Synthesis and spectroscopy of two-dimensional semiconductors and heterostructures

Jonas Göser

München 2024

Synthesis and spectroscopy of two-dimensional semiconductors and heterostructures

Jonas Göser

Dissertation
an der Fakultät für Physik
der Ludwig-Maximilians-Universität
München

vorgelegt von
Jonas Göser
aus Erlangen, Deutschland

München, den 29. Oktober 2024

Erstgutachter: Prof. Dr. Alexander Högele
Zweitgutachter: Prof. Dr. Kai Müller

Tag der mündlichen Prüfung: 06.12.2024

Zusammenfassung

Die vorliegende Dissertation beschreibt Ergebnisse zur kontrollierten Synthese von hochwertigen ein- und doppellagigen Übergangsmetall-Dichalcogeniden (transition-metal dichalcogenides, TMDs) mittels chemischer Gasphasenabscheidung (chemical vapor deposition, CVD). TMDs, wie $MoSe_2$ oder WS_2, bergen aufgrund ihrer einzigartigen elektronischen und optischen Eigenschaften Potenzial für zukünftige Halbleitertechnologien. Als Teilfamilie der zweidimensionalen Materialien weisen TMDs Eigenschaften auf, die sich aus ihrer direkten Bandlücke im monolagigen Grenzfall ergeben, wo die Beschränkung auf zwei Dimensionen zu starken exzitonischen Effekten führt. Ihre Spin-Valley-Polarisation, die durch optische, elektrische und magnetische Felder manipuliert werden kann, macht sie relevant für Anwendungen wie die Valleytronik und die Optoelektronik.

Ein Hauptziel dieser Arbeit war, ein reproduzierbares Wachstum von einkristallinen TMDs mit hoher Ausbeute zu erreichen und gleichzeitig Defekte zu minimieren, was bei CVD-Prozessen eine zentrale Herausforderung darstellt. Zu diesem Zweck, werden mehrere Innovationen bei den Wachstumstechniken vorgestellt, darunter Verbesserungen der Qualität und der Reproduzierbarkeit durch eine erweiterte Reihe von Parametern, sowie eine Verkürzung der Gesamtwachstumsdauer.

Desweiteren wurden die Verarbeitungsprozesse für CVD gewachsene Proben verbessert, was die Untersuchung von eingekapselten Mono- und Doppellagen, vertikalen und lateralen Heterostrukturen, sowie monolagigen Chalgonid-Legierungen und deren Heterostrukturen ermöglicht. Diese Ergebnisse stellen einen Beitrag zur Bandstruktur-Konstruktion in TMD Heterostrukturen dar und sind grundlegend für die Abstimmung der Valenzbandresonanz durch den Grad der Legierung. Das direkte Wachstum von Heterostrukturen ermöglicht außerdem die Untersuchung komplexerer Architekturen wie laterale Verbindungen von Homo-zu-Heterolagen oder Hetero-Homolagen.

Eine umfassende Charakterisierung, einschließlich optischer Spektroskopie bei Raum- und kryogener Temperatur und energiedispersiver Röntgenspektroskopie, wies auf die Qualität der Materialien hin und offenbarte Merkmale wie Exzitonenresonanzverschiebungen, Legierungsgradienten und ausgeprägtes exzitonisches Verhalten in Moiré-Übergittern. Die Ergebnisse unterstreichen nicht nur das Potenzial von TMDs in praktischen Anwendungen, sondern verdeutlichen auch die Bedeutung einer präzisen Kontrolle bei der Materialsynthese.

Abstract

The present PhD thesis describes the controlled synthesis of high-quality mono- and bilayer transition-metal dichalcogenides (TMDs) using chemical vapor deposition (CVD). TMDs, represented by materials such as $MoSe_2$ or WS_2, hold immense potential for next-generation semiconductor technologies due to their unique electronic and optical properties. As part of a broader class of two-dimensional materials, TMDs exhibit properties stemming from their direct bandgap in the monolayer limit, where the confinement to two dimensions leads to strong excitonic effects. Moreover, their spin-valley polarization, tunable by optical, electric, and magnetic fields, makes them relevant for applications such as valleytronics and optoelectronics.

A primary goal of this work was to achieve reproducible, high-yield growth of monocrystalline TMDs while minimizing defects, which poses a key challenge in CVD processes. To this end, the thesis introduces several innovations in growth techniques, including quality and reproducibility improvements through an extended set of parameters, as well as a decrease in overall growth duration for optimized feedback loops.

Furthermore, TMD fabrication processes for CVD grown samples were improved, enabling studies of encapsulated monolayers and bilayers, vertical and lateral heterostructures, as well as monolayer chalcogen alloys and heterostructures thereof. These results represent contributions to bandstructure engineering in TMD heterostructures and are foundational for valence band resonance tuning through the degree of alloy. The achievement of heterostructure growth further enables the study of more complex architectures, such as homo-to-heterobilayer or hetero-homobilayer junctions.

Extensive characterization, including optical spectroscopy at room- and cryogenic temperature and energy-dispersive X-ray spectroscopy, indicated the material's quality and revealed features like exciton resonance shifts, alloy gradients, and distinct excitonic behaviors in moiré superlattices. The results not only underscore the potential of TMDs in practical applications, but also highlight the importance of precise control in material synthesis for advancing semiconductor technologies.

There is plenty of space
in two dimensions.

List of Publications

[P1]. Park, A., **Göser, J.**, Kantipudi, R., Esin, I., Chen, Y., and Yeh, N.-C., "Manipulation of Excitonic Orbital Angular Momentum with the Topological Charge of Light", in writing

[P2]. Scherzer, J., Lackner, L., Han, B., Polovnikov, B., Husel, L., **Göser, J.**, Li, Z., Drawer, J. C., Esmann, M., Bennenhei, C., Eilenberger, F., Watanabe, K., Taniguchi, T., Baimuratov, A., Schneider, C., and Högele, A., "Correlated magnetism of moiré exiton-polaritons on a triangular electron-spin lattice", *arXiv:2405.12698* (2024), under review at *Nat. Phys.*

[P3]. Polovnikov, B., Scherzer, J., Misra, S., Schlömer, H., Trapp, J., Huang, X., Mohl, C., Li, Z., **Göser, J.**, Förste, J., Bilgin, I., Watanabe, K., Taniguchi, T., Bohrdt, A., Grusdt, F., Baimuratov, A., and Högele, A., "Implementation of the bilayer Hubbard model in a moiré heterostructure", *arXiv:2404.05494* (2024), under review at *Nat. Mat.*

[P4]. Park, A., Kantipudi, R., **Göser, J.**, Chen, Y., Hau, D., and Yeh, N.-C., "Strongly Enhanced Electronic Bandstructure Renormalization by Light in Nanoscale Strained Regions of Monolayer MoS_2/Au(111) Heterostructures", *ACS Nano* (2024)

[P5]. Polovnikov, B., Scherzer, J., Misra, S., Huang, X., Mohl, C., Li, Z., **Göser, J.**, Förste, J., Bilgin, I., Watanabe, K., Taniguchi, T., Högele, A., and Baimuratov, A., "Field-induced Hybridization of Moiré Excitons in $MoSe_2$/WS_2 Heterobilayers", *Phys. Rev. Lett.*, 132, 076902 (2024)

[P6]. Wietek, E., Florian, M., **Göser, J.**, Taniguchi, T., Watanabe, K., Högele, A., Glazov, M., Steinhoff, A., and Chernikov, A., "Nonlinear and Negative Effective Diffusivity of Interlayer Excitons in Moiré-Free Heterobilayers", *Phys. Rev. Lett.*, 132, 016202 (2024)

[P7]. Rupp, A., **Göser, J.**, Li, Z., Bilgin, I., Baimuratov, A., and Högele, A., "Imaging Lattice Reconstruction in Homobilayers and Heterobilayers of Transition Metal Dichalcogenides", *2D Mater.*, 10, 045028 (2023)

[P8]. Zhao, S., Li, Z., Huang, X., Rupp, A., **Göser, J.**, Vovk, I., Kruchinin, S., Watanabe, K., Taniguchi, T., Bilgin, I., Baimuratov, A., and Högele, A., "Excitons in Mesoscopically Reconstructed Moiré Heterostructures", *Nat. Nanotechnol.*, 18, 572-579 (2023)

[P9]. Rupp, A., **Göser, J.**, Li, Z., Altpeter, P., Bilgin, I., and Högele, A., "Energy-dispersive X-Ray Spectroscopy of Atomically Thin Semiconductors and Heterostructures", *Phys. Rev. Appl.*, 18, 064061 (2022)

[P10]. Polovnikov, B., Scherzer, J., Misra, S., Huang, X., Mohl, C., Li, Z., **Göser, J.**, Förste, J., Bilgin, I., Watanabe, K., Taniguchi, T., Baimuratov, and A. Högele, A., "Coulomb-correlated States of Moiré Excitons and Elementary Charges on a Semiconductor Moiré Lattice at Integer and Fractional Fillings", *arXiv: 2208.04056* (2022)

Contents

Chapter 1

Introduction

Human history has partly been divided into sections, named after materials of the time that shaped human lives through the technologies they enabled. There is the Stone Age with its monuments and tools carved out of stone, the Bronze Age, elevating technologies according to the new-found metal, and the Iron Age, giving rise to more durable and complex machinery [1]. Many more materials and corresponding technologies shaped human history, often simultaneously, making it difficult to assign single materials to a specific time period of modern history. However, if we were to continue this naming convention, there is one material family that could serve as a description for the modern period of humankind due to its overwhelming impact on our daily lives. The corresponding time period would be called: the Age of Semiconductors.

Semiconductors possess electrical properties that place them between conductors, such as metals, and insulators, such as most glasses and ceramics. While insulating in their natural ground state, they can be made conductive through a number of external stimuli, including electric or magnetic fields, temperature, mechanical pressure, or exposure to light. This change in electrical conductivity through external means has given rise to the transistor and complex integrated circuitry, enabling everything from smartphones to supercomputers, laying the groundwork for next generation quantum technologies, and driving the rapid progress in artificial intelligence.

To produce such highly complex systems, the semiconductor industry is based on one foundational process: material growth. This term encompasses epitaxy, which retains lattice-matching between the growing material and the substrate, and deposition. Deposition methods include physical vapor deposition, chemical vapor deposition (CVD), as well as its subset of atomic layer deposition. These techniques enable the formation of intricate multilayer architectures down to the nanometer scale by depositing single or multilayers of material onto a substrate. Any new material, such as

members of the novel two-dimensional transition-metal dichalcogenide (TMD), being considered for next-generation semiconductor devices must integrate with these established material growth methodologies to ultimately enhance device performance and continue the industry's ongoing push of reducing device dimensions - a trend famously framed by Moore's Law.

In addition to their two-dimensional nature - each layer extending just over half a nanometer in thickness - TMDs possess many unique properties that make them attractive for many technological applications. Correspondingly, strides have been made to enable desirable growth outcomes. For instance, polycrystalline monolayer films, which consist of randomly oriented, monocrystalline domains approximately one micrometer in size, can be grown on macroscopic length scales, covering entire wafer substrates [2]. However, polycrystalline TMDs lack the desirable attributes of monocrystals, such as the high charge-carrier mobility and uniform charging behavior. The challenge, therefor, is to grow high-quality monocrystalline TMD monolayers reliably, such that the method can be integrated into industrial processes. This includes either achieving wafer-scale growth or enabling spacially deterministic control over the growth origin for single-crystal array fabrication.

In this thesis, we tackle the challenge of achieving high-quality monocrystalline monolayer growth via CVD and evaluate such crystals using optical spectroscopy. The corresponding linewidth observed in optical photoluminescence and reflection spectroscopy indicates high sample quality and low defect density. Such samples are shown to host intricate excitonic states - states of bound electron-hole pairs - across two monolayers with particular trapping and charging behavior within specific superlattice potentials, known as moiré potentials, that form between two interacting TMD monolayers in specifically designed heterostructure.

Additionally, we demonstrate that the growth process used to produce high-quality monolayer TMDs can be modified to yield bilayers, lateral and vertical heterobilayers, more elaborate architectures such as homo-to-heterobilayer junctions and hetero-homobilayer junctions, as well as monolayer alloys for a wide tunability of the energetic properties. The specific materials, as introduced in Chapter 2, belong to the family of TMDs where the general formula is MX_2, with the transition-metal M consisting of molybdenum (Mo) or tungsten (W) and chalcogens X consisting of sulfide (S), selenide (Se), or telluride (Te). Different heterostructures and the more complex variations are based on MoS_2 and $MoSe_2$ with the alloyed material system of choice being $MoSe_{2(1-x)}S_{2x}$, where x denotes the degree of alloy.

The concrete structure of this thesis is as follows. After a concise introduction into two-dimensional TMD materials and their monolayer limit in Chapter 2, the most relevant methods which we either adopted or developed in the scope of this thesis are presented in Chapter 3. This includes methods for CVD, device fabrication, optical spectroscopy, and energy dispersive X-ray spectroscopy. Chapter 4 comprises the results on high-quality monolayer crystals presented in microscopic imaging as well as optical photoluminescence and reflection spectroscopy. After a theoretical treatment of two-dimensional crystal growth, optimizations and improvements to the experimental setup are discussed. Thereafter, growth results for molybdenum and tungsten based monolayers are presented. Chapter 5 comprises the advances in growth methodologies to include lateral and vertical heterostructures, respectively in the monolayer and in the bilayer plane. The results include more complex architectures and heterogeneous junctions. Special attention is given to the effect of alloying between chalcogenides in the molybdenum based systems. Subsequently, a growth method is implemented, which realizes specific alloy outcomes in the monolayer crystal. Chapter 6 summarizes the results and contributions of this thesis and gives an outlook into future projects and directions of the field.

Chapter 2

Semiconducting transition-metal dichalcogenides

2.1 The monolayer limit

The research on two-dimensional materials mostly started after the isolation of a single, mono-atomic sheet of graphene and its initial electrical studies in 2004 [3]. The idea of two-dimensional materials was not new, however, initial interest ebbed away due to the expectation that such single layers of material would not be thermodynamically stable [4]. It was only the fabrication method of mechanical exfoliation in which a Scotch tape is used to overcome the van der Waals forces within the bulk, that made it possible to isolate a single layer of graphene from its bulk crystal and to show that, indeed, the two-dimensional limit of the crystal is sustainable [5, 6]. As it turned out, graphene is only one material among others that, due to weak van der Waals forces between their layers, can exist in the two-dimensional form. Since its isolation, many materials have followed giving rise to a whole material family of so-called two-dimensional materials [5, 7, 8]. The zoo of materials within this family is comprised of insulators, such as hexagonal boron nitride [9], semiconductors, such as transition-metal dichalcogenides (see below), semi-metals such as graphene itself [10], and metals and superconductors, such as $NbSe_2$ or TaS_2 [11, 12] among others. It is the subset of two-dimensional semiconductors which is of particular interest for the work at hand.

Early studies of semiconducting transition-metal dichalcogenides (TMDs) go back over half a century [13–15]. However, it was the fabrication method of mechanical exfoliation that resulted in extensive study of the transition from few-layer bulk systems to the monolayer limit, which established group-VI TMDs as direct band gap semiconductors [16, 17]. Monolayer exfoliation is a work-intensive, low-yield method in which

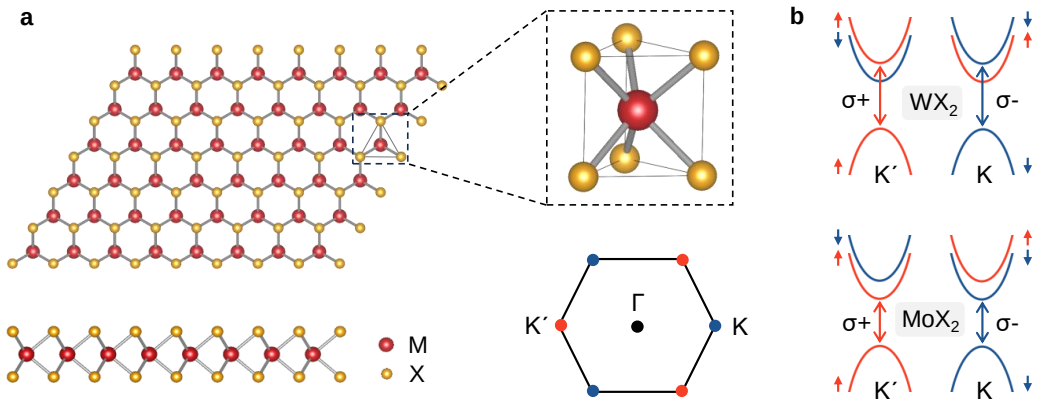

Figure 2.1: Physical representation of monolayer TMD. **a**,Top view (top left) and **a** side view (bottom left) with transition-metal atoms M (molybdenum or tungsten) in red and chalcogen atoms X (sulfur, selenide, or telluride) in gold. The right displays a 3D view of the crystal primitive cell (top) and the Brillouin zone with indicated high symmetry points Γ, K, and K' (bottom). Real-space representations were done using VESTA simulation software [18]. **b**, Valley-dependent optical selection rules for interband transitions in monolayer TMDs. $\sigma+$ polarized light couples to the K' valley (red), $\sigma-$ polarized light to the K valley (blue). Small arrows indicate spin in the corresponding band. In tungsten based materials (top) the momentum direct transition becomes spin indirect due to reversed ordering of spin states in the conduction band, in molybdenum based systems the transition remains direct (bottom).

material samples only display lateral sizes around 5 to 10 μm. In these aspects, a better alternative would be desirable not only for scientific progress, but, ultimately, for the industry-scale integration which will require a high-yield method, functional on the wafer scale, and compatibility with existing manufacturing technologies.

Group-VI TMDs are layered materials of the form MX_2 with transition-metal atom M (molybdenum or tungsten) and chalcogen atom X (sulfur, selenide, or telluride) as depicted in Fig. 2.1. Each layer consists of covalently bound X-M-X units forming a three atomic sheet of 6.15 Åin height [13] with the transition-metal in the center and chalcogen atoms at the top and bottom. These layers can come in three phases: 1T, 1T', and 2H [19, 20]. It is the stable, semiconducting 2H phase which is of interest here, however, the former two metallic phases can become relevant in material growth (see telluride-based growth in Chapter 4.3.1). Layers in out-of-plane direction are bound by van der Waals forces with an interlayer gap of 6.5 Å[21], making mechanical exfoliation from the bulk possible. In the bulk, the band gap is indirect between Γ and K points in the Brillouin zone, see Fig. 2.1a bottom right, with electronic state contributions at Γ from p_z and d_{z^2} orbitals from chalcogen and transition-metal atoms, respectively [22]. While these contributions are strongly effected by neighboring layers, orbital

contributions at the K and K' points remain unaffected, making the transition to a direct gap in the monolayer limit at these points possible. In addition, due to lower electric screening of the monolayer's surrounding, excitons, bound states of excited electrons and holes in the conduction and valence band, respectively, have binding energies of around 0.5 eV [22–28], making them stable at room temperatures. Furthermore, strong spin-orbit coupling leads to a large spin splitting of 200-400meV within the valence band [29–34] with spin degenerate K and K' valleys, see Fig. 2.1b. This leads to interesting optical selection rules where $\sigma+$ and $\sigma-$-circular polarized light couples only to the corresponding K and K' valley, allowing for direct optical access to the spin-valley polarization of excitons. Notably, the ordering of spin states in the conduction band of tungsten based monolayers is reversed, leading to spin-dark ground state transitions in optical spectroscopy [35, 36].

Monolayer technology

The above introduced physical properties of semiconducting TMD monolayers not only sparked high scientific, but also technologically driven interest. Since the topic of material growth has an enabling role in realizing such technologies at scale, a brief overview over some of the technological pathways shall be given.

From an electronic standpoint, atomically thin semiconductors are highly relevant for next generation transistor devices [37] or novel bendable electronics [38]. Over the past decades, the microchip industry has increased the number of transistors per unit area roughly by a factor of two every two years in order to increase computation capabilities while keeping the over-all size of the chip and its costs constant. This development is often referred to as 'Moore's law' [39, 40]. However, as the silicon- and lithography-based length scales inside transistors reach their physical limit of respectively 12 nm [37] and 13.5 nm [41] (with current state-of-the-art devices featuring channel lengths around 28 nm, gate lengths of 16 nm, and channel thicknesses of around 5 nm [42]), new materials are sought after. Here, two-dimensional TMDs can play a key role. By incorporating them as atomically thin channels inside field-effect transistors, channel lengths down to several nanometers where achieved [43–47]. Initially, also graphene had been considered as ultra-thin channel material due to its high charge carrier mobility in the order of $10^5 \mathrm{cm}^2/\mathrm{Vs}$ [3, 48], but the lack of a band gap limited further development [49]. Nevertheless, graphene can be incorporated into TMD-based transistor designs as gate material. Here, carbon nanotubes, rolled up

sheets of graphene, were used, scaling gate lengths down to 1nm [43].

A key parameter for channel material is the charge carrier mobility. Even though the charge carrier mobility of bare TMD monolayers is lower than their bulk systems (3cm^2/Vs [5] compared to 60-200cm^2/Vs [50–52]) it can be increased to meet transistor technology requirements by optimizing the dielectric environment around the monolayer with resulting charge carrier mobilities in the hundreds of cm^2/Vs [21, 53–56]. Furthermore, it was shown that TMD monolayers can be integrated into sophisticated state-of-the-art transistor architectures such as three dimensional complementary metal oxide semiconductor (CMOS) devices [57] or the novel fin field-effect transistor (FinFET) [58].

As mentioned above, monolayer TMDs exhibit degenerate valleys around their valence band maximum and conduction band minimum at K and K' points in the Brillouin zone as a direct consequence of strong spin-orbit coupling and the absence of an inversion center [30]. This fact established TMDs as prime material platform to study in the context of valleytronics, a research direction with the goal to utilize the valley degree of freedom of charge carriers for electronics applications in a similar way as the electric charge [59], exploiting the lack of energy dissipation through Joule heating within valley currents. First experiments used circular-resolved polarization spectroscopy to study valley polarization in TMDs, exploiting direct optical access of the valley degree of freedom [60–63]. Then, the observation of the so-called valley Hall effect effectively encodes the valley polarization into an electrical signal [64] whereas its inverse effect results in circularly polarized electroluminescence [65, 66]. Finally, an all-electrical device was fabricated to create and detect charge-neutral valley currents over distances of several μm [67, 68]. Notably, the device of Hung et al. [68], based on monolayer MoS_2, was fabricated using chemical vapor deposition, emphasizing the scalability of the technology.

From an optics perspective, a range of applications can be realized using TMDs monolayers, utilizing, for example, their strong light-matter interaction, excitonic properties, low dimensionality and weight, as well as mechanical flexibility. Among others, applications include electroluminescence devices, photovoltaic solar cells, and photodetectors [69–71]. An interesting application arises from the electro-optical tunability of TMDs, which is of particular interest for integrated photonics [72, 73]. When considering a wavelength range in the off-resonant near-infrared spectrum, TMDs have shown a high ratio of refractive to absorptive coefficients while displaying high electro-refractive

tunability in combination with a small electro-absorptive response. In particular, WS_2 and MoS_2 were studied with ratios reaching ~125 at 1571 nm wavelength, higher than silicon-based modulators [74].

2.2 Heterostructures

Combining multiple two-dimensional materials promises intriguing pathways for the creation of materials by design [75, 76], which can be fabricated using different methods [77] as discussed below in Chapter 3.2. Combining materials allows to build material systems with tailored properties to study as physical systems or to utilize in specific technologies. For example, layers of hexagonal boron nitride (hBN) exhibit a band gap in the UV range and are therefor used as atomically flat encapsulation dielectric for TMDs [78–86], increasing carrier mobilities [21, 53–56, 87], reducing inhomogeneous broadening effects in optical spectroscopy [88–90], and serving as spacer layers between TMD monolayer systems [91–95].

Vertically stacking of two TMD monolayers is one way to combine layers with intended properties into homobilayers (using the same material) or heterobilayers (using different materials) into so-called van der Waals heterostacks. The alternative to stacking is the direct growth method, which in vertical direction results in better alignment along the 0° and 60° rotational axis. There have been tremendous advances in growth techniques to enable direct TMD hereostructure growth in the vertical direction [96–113]. Direct-growth also enables new architectures, such as lateral heterojunctions in the monolayer plane, as well as combinations of lateral and vertical material combinations. Examples of such material systems are discussed in Chapter 5.

Placing two different TMD semiconducting monolayers in contact with each other creates a heterojunction with band offsets between the valence as well as the conduction band according to Anderson's rule [114, 115]. Density-functional theory and ab initio calculations have predicted type-II band alignment for most TMDs [114, 116], see Fig. 2.2a, which could be shown experimentally in angle-resolved photoemission spectroscopy [117]. For the material system of $MoSe_2/WS_2$, for which the conduction band edges where predicted to lie very close together, a type-I band alignment could be demonstrated in [P3], [P5] and [P10].

The different alignment of energy levels in TMD heterostructures can result in charge separation across the layers as well as charge hybridization between them [118–124],

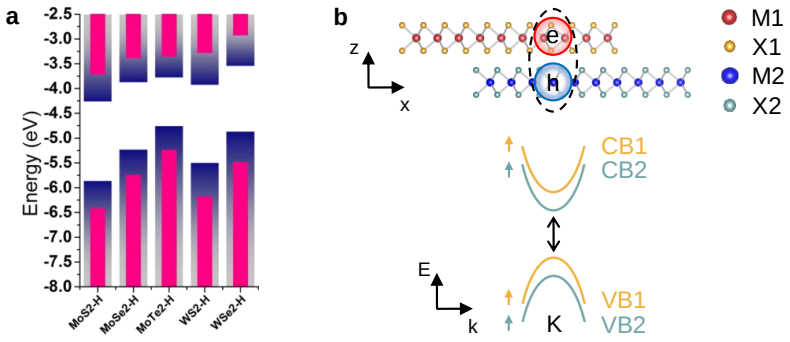

Figure 2.2: Interlayer band alignment in TMD heterostructures. **a**, Density functional theory calculations. **b**, interlayer excitons as a direct result from the alignment. Electrons (e) and holes (h) are separated across the two layers forming interlayer excitons (dashed line). The energetic transition is significantly lower than both intralayer exciton transitions. Subfigure **a** and **b** adopted from [116] and [127], respectively.

[P5]. In the case of charge separation, the exciton, initially created in one of the layers, will separate across the van der Waals gap between the layers and form so-called interlayer excitons (Fig. 2.2b, dashed line) with binding energies above 100 meV, altered lifetimes in the order of nanoseconds [125–129], diffusion lengths in the order of micrometers [130], and many other properties resulting from the reduced overlap of the wavefunctions due to spacial separation [127, 131, 132].

Overlapping two periodic lattices can create a superlattice interference pattern. This is formed, when the two sublattices possess a non-zero difference in lattice constants a_1 and a_2 and/or the lattices are twisted with respect to each other by an angle θ, see Fig. 2.3. This superlattice is called a moiré lattice, which sparked immense research interest [133–138]. For the hexagonal superlattice with TMD monolayers as sublattices, the resulting lattice vector length L_m of the superlattice, i.e. its periodicity, will be [139]:

$$L_m(\theta) = \frac{a_1}{\sqrt{1 + \left(\frac{a_1}{a_2}\right)^2 - \frac{2a_1}{a_2}\cos(\theta)}}. \tag{2.1}$$

This new length scale in real space introduces a new length and energy scale in reciprocal space which allows to realize moiré excitons and trions [121, 140–148], [P5], [P8] and [P10], novel quantum phenomena [149–155], [P3], and allows to engineer novel phases of matter [94, 134, 156–170].

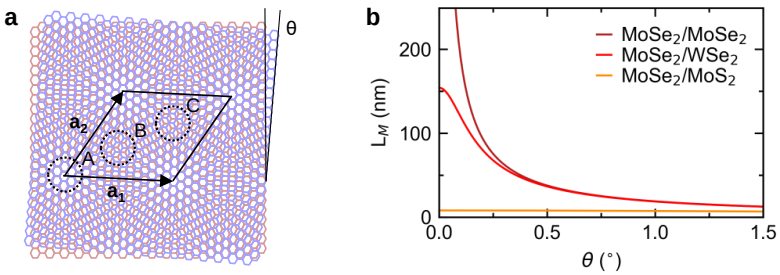

Figure 2.3: **a**, Moiré lattice between two sublattices with the same lattice constant and an interlayer twist-angle $\theta = 5°$. The moiré periodicity of the moiré lattice is given by the lattice vectors: $L_m = \|a_1\| = \|a_2\|$. All three symmetry bilayer stackings A, B, and C (dashed circles) are present within a moiré unit cell and depend on the stacking type. **b**, The moiré lattice periodicity for different sublattice combinations according to equation 2.1. A difference in transition-metal does not limit the moiré periodicities as strong as for a difference in chalcogenide. For example, at 0° twist-angle the $MoSe_2/WSe_2$ system (bright red) and $MoSe_2/MoS_2$ (yellow) are limited to ~154.2 nm and ~7.6 nm, respectively.

Within a moiré unit cell, all high symmetry stackings of a given orientation (R-type or H-type according to 0° or 60° twist-angle, respectively) are present. The difference in formation energies for each of the stackings leads to lattice reconstruction into an energetically favorable high symmetry stacking, locally within the moiré unit cell, as well as globally across mesoscopic length scales, particularly around large defects in the system or towards edges and corners [P7] and [P8].

From a growth perspective, tuning the twist-angle between two TMD layers grown on top of each other has posed a challenge: since the heterobilayer is build up atom-by-atom, the resulting stacking occurs most likely in the energetically most favorable stacking orders along 0° or 60° twist-angle [113]. However, notable growth techniques have realized twist-angle growth in graphene [171, 172] and recently also for TMD heterobilayers consisting of alloyed single-layers [173].

Growth of TMD heterostructures offers a unique way to realize not only vertical heterostructures, but also lateral heterojunctions, i.e. in-plane transitions from one material to another. There has been much progress in growth methodologies to realize such systems [174–185] which promise to host inter-material excitons across the junction, so-called charge transfer excitons [186]. A key challenge with this growth is to prevent alloying and cross-contamination effects when growing one material after the other [77], as is discussed in Section 5.1.2.

This growth of laterally interfacing two TMD monolayers can also be performed on the bilayer level. An example is the lateral junction of homobilayers realized in the

MoS_2-WS_2 and $MoSe_2$-WSe_2 systems [187]. As is discussed in Chapter 4, also more complex architectures are possible combining homo- and heterobilayers (see Section 5.1.2).

Heterostructure technology

The field of technological applications for TMD heterostructures is immense. Ranging from electrochemical, optical, and photonic applications to excitonic technologies and technologies that harvest emerging phenomena such as correlated many-body states and superconductivity [188–191]. For excitonic devices, harvesting the properties of the interlayer exciton is especially attractive due to its long lifetime and large exciton binding energy resulting in stability at room temperatures, in contrast to III-V and II-IV semiconductor quantum well heterostructures [93].

The work at hand addresses direct heterostructure growth in the vertical and lateral direction of the corresponding monolayers as well as combinations of the two. For industry adoption, wafer scale growth is essential for which early studies have shown promising results [192, 193].

Chapter 3

Experimental methods

3.1 Chemical vapor deposition

Chemical vapor deposition (CVD), or atmospheric pressure chemical vapor deposition (APCVD) in the work at hand, was performed using a three-chamber quartz-tube furnace (Carbolite Gero EZS-3G) with 2000W heating power, imaged in Fig. 3.1. The quartz glas tube connects all three chambers and is connected via flange adapters to the gas inlet and outlet. At the inlet side, two flow meters (Alicat Scientific MCE-500SCCM-D/5M and MCE-200SCCM-D/5M) separately control the inflow of argon, serving as inert carrier gas, and hydrogen, serving as oxygen reduction agent, with maximum output of 625 sccm and 250 sccm, respectively, while on the outlet side the gas is led through either a pump (Edwards E25M High Vacuum Pump) for initial pre-growth pumping of the system, or simply bypassing the pump to the exhaust during the growth process. The temperatures within the chambers is controlled for each chamber separately via controllers (model Eurotherm 3216CC) which allow for manual control of temperatures up to 1200°C, individual ramp-up rates, and ramp-up powers, which were generally set to 90%. Manipulation of said parameters was performed initially and during the growth process. Cooling down of the system was achieved through ambient air simply by opening the furnace or, in some cases, with more effective cooling through a fan. A photo of the setup is depicted in Fig. 3.1.

Initially, the precursor material is placed in high-alumina combustion boats (Coors^{TM}) with a 5 ml capacity, see Fig. 3.2. The boat with the molybdenum dioxide powder additionally contains the 1x1 cm pre-cut Si/SiO_2 substrates with a 285 nm SiO_2 layer (CrysTec GmbH, polished, etched, 100K wafers, type-N pre-doped with Phosphorus, and specific resistance of 1-20 Ohm). The substrates are placed directly on top of the precursor material, the SiO_2 pointing downwards, leaning against the side wall of the

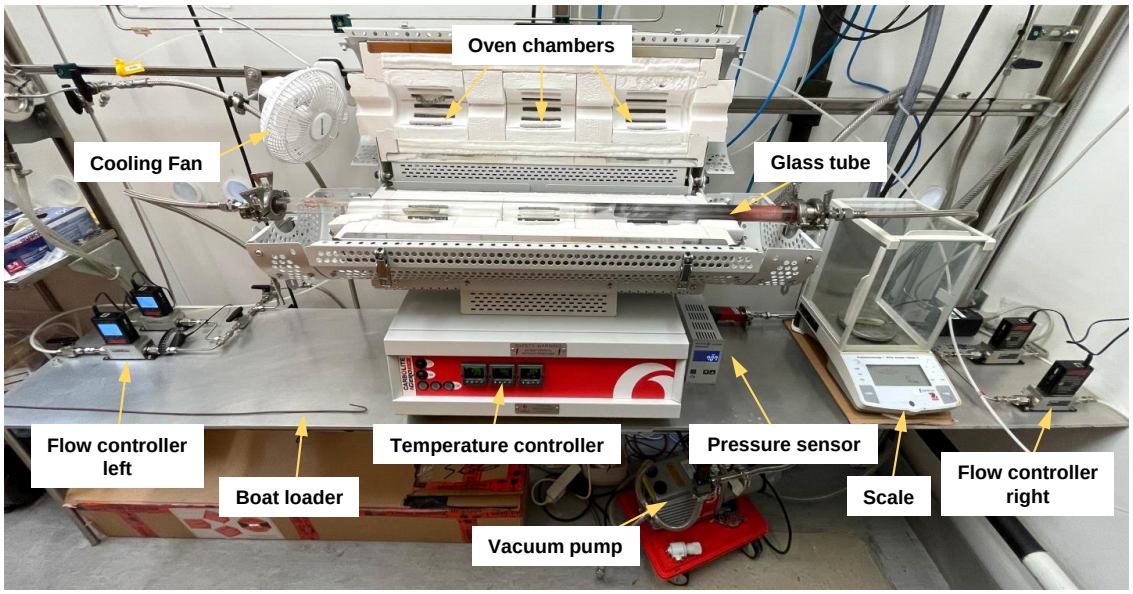

Figure 3.1: Image of the CVD setup with the three-chamber furnace. Carrier gas flow amount and composition can be controlled from either side of the tube using the flow meters. The scale is used to weigh the powders before placing the aluminum boats inside the tube using the boat loader. The cooling fan is attached to the back wall and is used to cool the chambers down to room temperature after growth.

boat to ensure high molybdenum precursor concentration as well as flow of chalcogen precursor onto the substrate, see Fig. 3.2. The boats are subsequently loaded into their respective chamber inside the quartz tube using a metal hook slider and the quartz tube is closed using flange connectors. While starting the initial heat-up of the system (specifically the main growth chamber with initial ramp-up to 400-650°C in 30-50°C/min) the tube is pumped down to 1.5-2x10^{-1} Torr and flushed with argon gas three times consecutively to eliminate atmospheric gas residues. All relevant parameters are listed in Fig. 3.3.

3.2 Device fabrication

Following material growth on Si/SiO_2 substrates, monolayer transition-metal dichalcogenides (TMDs) are often incorporated into van der Waals heterostructures, see Chapter 2.2. These may or may not include multiple TMDs ([P2], [P3] and [P5] to [P10]), electrically contacted by few-layer graphene ([P2], [P3], [P5] and [P10]), encapsulated by hexagonal boron nitride (hBN) ([P2], [P3], [P5], [P6], [P8] and [P10]), and sandwitched

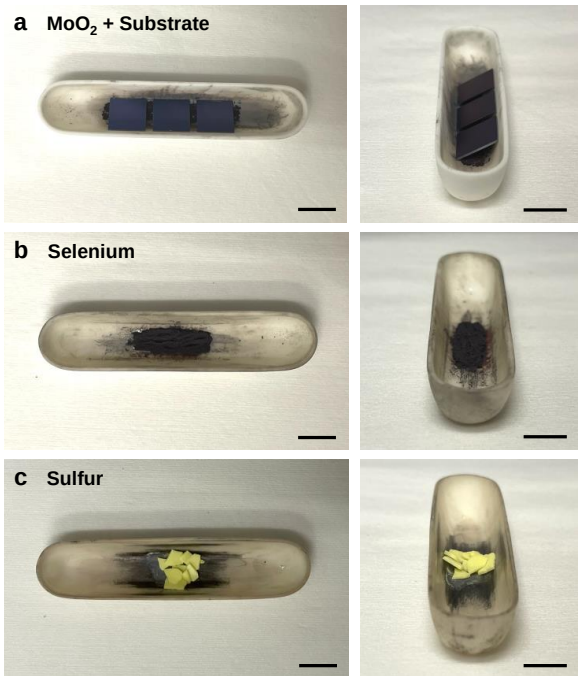

Figure 3.2: Precursor and substrate placement inside the high alumina combustion boats as side-view (left) and top-view (right) of the precursors MoO_2 (**a**), selenium (**b**), and sulfur (**c**). Precursors as indicated with the substrates placed sideways directly on top of the molybdenum precursor powder. The scalebar is 1cm.

by few-layer graphene as top and bottom gates ([P2], [P3], [P5] and [P10]). Commercial graphene (*HQ graphene*) and hBN (National Institute for Materials Science (NIMS) of Japan [194]) where hereby exfoliated from the bulk. During mechanical exfoliation, thin-film material is peeled off from the bulk using Nitto Tape BT-150P-LC [195], which proved to be more stable at higher temperatures than conventional Scotch^{TM} tape [5]. The material on the tape is then transferred onto Si/SiO_2 substrates at elevated temperatures (around 140°C), and peeled off while cooling down. This leaves material flakes on the substrate at various thicknesses. Material flakes are chosen to be clean under the optical microscope, which is achieved using contrast and gamma filters in the microscope software to isolate material flakes that are only *surrounded by* a tape residue contact region. This indicates, that the exfoliation tape was only touching the surrounding of the flake, not contacting the actual flake but rather its originating bulk which remained attached to the exfoliation tape. Thickness analysis was performed using an atomic force microscope (Bruker ICON) in tapping mode.

In artificially fabricated homo- and heterobilayers, the twist-angle between the two

Parameter		Dimension	Responsibility
Final Temperatures	T_g T_X	°C	Chemical driving force and transition-metal concentration Chalcogen concentration
Temperature Ramp-up Rates	ΔT_g, ΔT_X	°C/min	Coordination of concentrations with growth process
Powder amounts	n_{MO_2},n_{WO_2}, n_X	mg	Molybdenum, tungsten and chalcogen concentration
Growth time	t_g	min	Duration of constant temperature after ramp-up
Total flow	Q	sccm	Particles mean velocity
Gas concentration	q_{Ar}, q_{H_2} t_{H_2}	sccm s	Transition-metal concentration Time of H_2 injection and increase in transition-metal concentration
Flow direction	left, right		Coordination of precursor or gas flow with growth process
Pressure	$p = p_{atm}$	Torr	
Substrate surface and placement	SiO_2, 1x1cm		Constant dimension of 1x1cm, 285nm SiO_2 on boron-doped silicon

Figure 3.3: Table of relevant parameters for CVD. The pressure as well as the substrates where hereby constant. For growth configurations with bidirectional flow, the corresponding parameters such as total flow (Q), gas concentrations (q_{Ar}, q_{H_2}, and t_{H_2}), and growth time would be adjusted for the right and the left side or the material, respectively.

TMD layers can play a crucial role (Chapter 2.2). Angle-control during fabrication is realized by rotation of the sample stage with respect to the stamp, i.e. the first layer with respect to the second, see Chapter 3.2.1 below. TMD monolayers are aligned with each other with respect to their crystallographic edges. Since these are unambiguous for grown samples due to the characteristic triangular shape, a precise angle-control with accuracy around 1° is achieved through the resolution of the sample stage and optical alignment capabilities. This gives a unique advantage of CVD-grown samples over exfoliated ones during fabrication, since crystallographic edges in exfoliated material leave the distinction between the 0°- and 60°-edge ambiguous. Therefor, in CVD-grown samples, R- and H-type samples can be fabricated deterministically.

3.2.1 Pick-up and stacking

Pick-up and stacking refers to the process of detaching layers of van der Waals material from their initial exfoliation or growth substrate and transferring them to a desired substrate. The method is also expanded to the pick-up of several layers consecutively, stacking them on top of each other, until the created van der Waals stack is dropped onto the final substrate. The process is also referred to as viscoelastic dry transfer or hot pick-up technique [196, 197], with considerable effort undertaken for its improvement

concerning clean interfaces between single layers within the van der Waals stack (e.g. here [198]). The process involves a polydimethyl-siloxane (PDMS) droplet as base polymer on a glass slide above which a contact polymer is attached (see Fig. 3.4 and Master theses [199] and [200] for details), which will be in direct contact with the first material of the stack. Due to its mechanical, adhesive, and chemical properties as well as its specific glass transition temperature, polycarbonate (PC) is used as contact polymer for hBN material. The corresponding process is illustrated in Fig. 3.6. It can be noted that also polycaprolactone (PCL) can be used as contact polymer [201]. The glass transition temperature is significantly lower than for PC, above which the polymer essentially becomes a liquid. The liquidity can be used to increase the binding to the underlying material. However, an improvement is only achieved for hBN pick-up, usually when the hBN flake has a height of several hundred μm, since TMDs need temperatures above 120°C to detach from SiO_2. These temperatures are not allowed for pick-up using PCL, however, due to its low glass transition.

The pick-up method uses the glass-polymer stamp to pick up one material after the other at various temperatures until the finished stack is deposited onto the final substrate by melting the contact polymer. Therefor, the polymers used have to withstand multiple cycles of heating and cooling while mechanical stress is exerted on them. Additionally, they need to be transparent to enable precise localization of the sample and placement of the stamp. For the stamp fabrication, see Fig. 3.4, a drop of PDMS mixed with curing agent 10:1 (Sylgard™184) is placed on top of a glass slide and placed face-down on top of a copper block on a heating plate at 140°C for 20 min such that the drop is hanging free. After additional drying for 12 h, a thin layer of contact polymer (PC or PCL) is placed on top of the PDMS using adhesive tape. The polymer film is prepared by placing a polymer/chloroform solution (6 mass-%) on top of a glass slide and, after pressing it with another glass slide, the glass slides are slid apart leaving a thin film of polymer. The adhesive tape is cut such that visibility through the glass slide and the polymer layers in ensured.

For the fabrication of van der Waals stacks, the polymer stamp is placed on top of a heating block and fixed by low-pressure vacuum, as depicted in Fig. 3.5. The block is movable in x/y/z-direction through piezo positioners. The sample stage is movable in x/y/ϕ-direction and consists of a heater and the sample holder through low vacuum. Both piezo positioners are used to align the stamp and the sample with the optical microscope.

TMD monolayers grown by CVD are very difficult to pick up. Most likely, this results from the fact that in comparison to exfoliated samples, grown monolayers build up

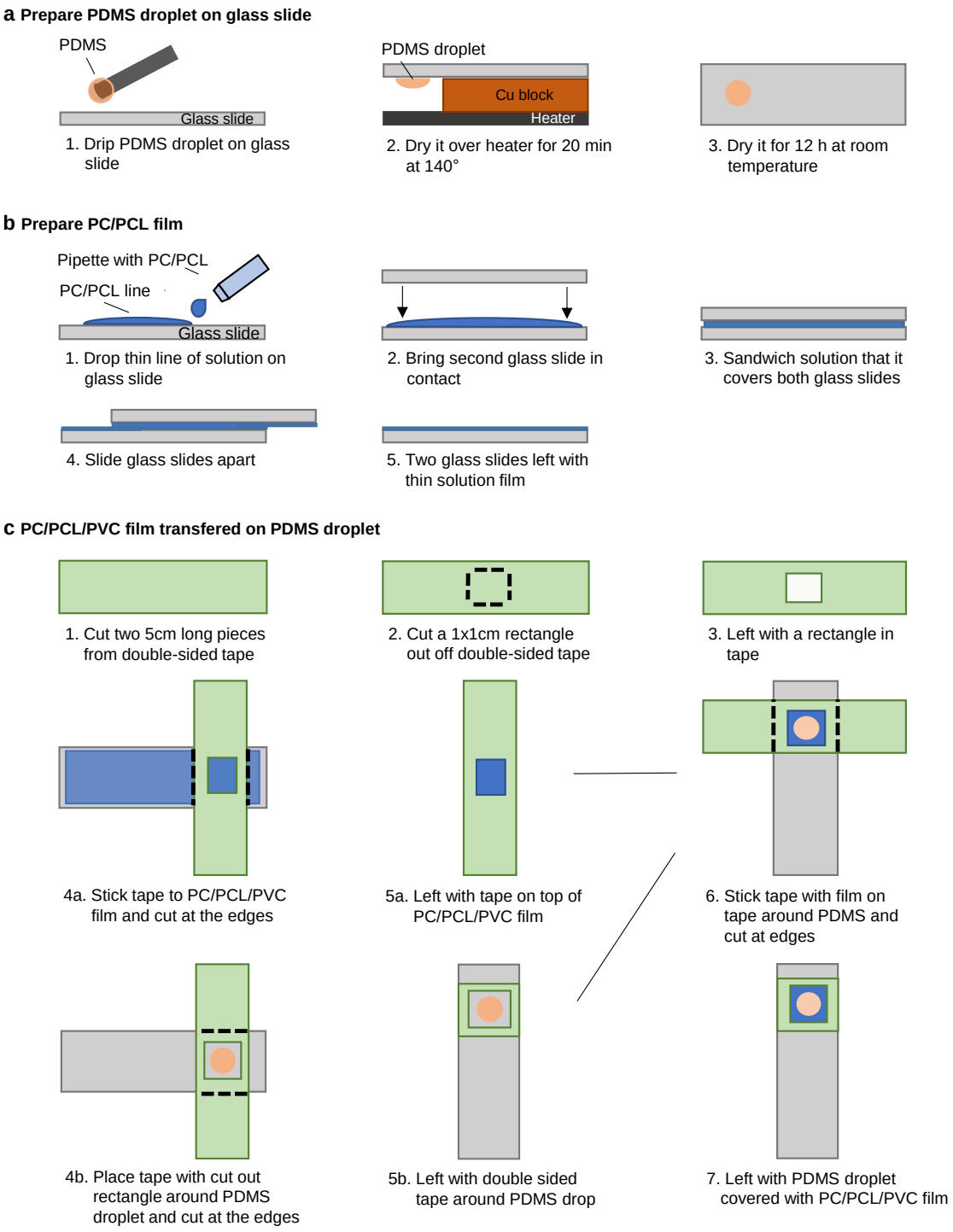

Figure 3.4: Fabrication method for the stamp used for pick-up and stacking. The details are described in the main text. Figure taken from [200].

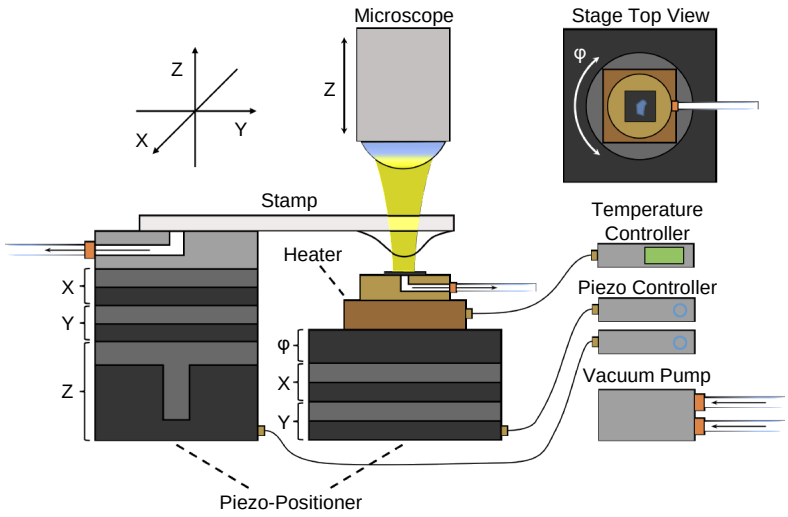

Figure 3.5: The fabrication setup for stamp-based pick-up and stambing. The stamp is aligned between a microscope and the sample through piezo positioners of the stamp and the sample. Both are fixed by low vacuum in the respective holders. Figure adopted from [202].

atom by atom, which increases bonding to the underlying SiO_2 surface. The bonding to the boron nitride layer (or the polymer, depending on whether boron nitride is used as encapsulation material) is then not strong enough to overcome the bonding to the surface. Therefor, a new pick-up sequence was developed which includes an additional annealing step in the process, is illustrated in Fig. 3.6. First, the polymer stamp is put in contact with the substrate roughly 200 μm away from the target material. This is achieved by only touching the substrate with the tip of the droplet-shaped polymer. For hBN, the substrate is at 40°C initially. The position of touch-down can then be altered to accommodate for the specific angle at which the pick-up is supposed to happen (e.g. due to an edge or a corner of the target material), or to ensure that a clean and homogeneous area of the polymer will land on the target material. Upon moving down of the stamp and polymer by the piezo positioners, the contact region to the substrate is increased. Shortly before touching the target material, the stage is heated to 90°C which will melt the PC over the material. Pick-up is achieved in reverse by cooling the stage back to 40°C. For TMD materials, the initial substrate temperature is set to 110°C, as illustrated in Fig. 3.6. After step 3, however, instead of picking up the TMD flake, the contact polymer is melted off the stamp (step 4) and after cool-down and washing in chloroform(TCM), acetone (ACE), and isopropyl alcohol (IPA) for 5, 4, and 3 min, respectively, to remove any polymer residues (step 5), annealed in a low vacuum chamber ($< 10^{-8}$ mbar) for at least 2 h (step 6). Afterwards, pick-up can continue with a

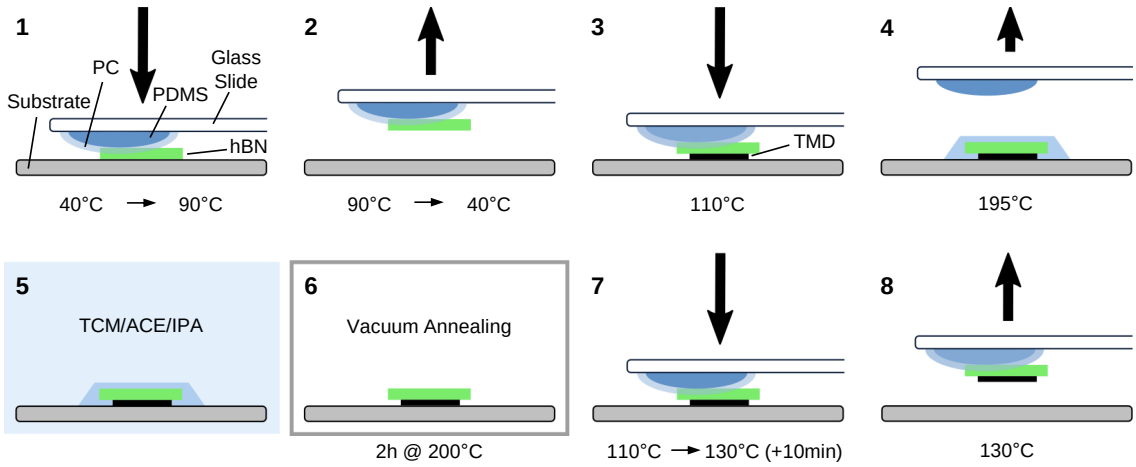

Figure 3.6: Novel pick-up sequence for grown TMD monolayers. A glass slide with a droplet-shaped polydimethyl-siloxane (PDMS) base polymer is covered with a film of either polycarbonate (PC) or polycaprolactone (PCL) as contact polymers and located upside-down roughly 200μm to the side of a material flake to pick up. After contacting the surface at an initial temperature, the temperature is increased which causes the contact polymer to expand and cover the entire material flake. Afterwards, contact area is increased to roughly 200 μm after the material flake. To pick up CVD grown samples, additional steps were included which deposit the hBN on top of the desired monolayer TMD (step 4), wash away the polymer residues in chloroform (TCM), acetone (ACE), and isopropyl alcohol (IPA) for respectively 5, 4, and 3 minutes, and let the van der Waals stack anneal in low vacuum ($< 10^{-8}$ mbar) at 200°C for 2 h (step 6). Pick-up and stacking continues afterwards with a new stamp (step 7). hBN is picked up at low temperature of 40°C while TMD crystals are picked-up at 130°C after 10 min of polymer contact. The final stack is deposited onto the final substrate in accordance to steps 4 to 6 with a 12 h annealing time.

new stamp (step 7). This is done in a similar fashion as before with an elevated contact temperature of 130° at which the stamp is kept in contact with the substrate for 10 min. For all materials the radius of contact to the substrate reaches about 200 μm away from the material flake. The distance can, however, be adjusted slightly ($\pm$50 μm) to adjust the pressure according to different droplet shapes. This technique of adding an additional vacuum annealing step during pick-up has proven effective for CVD grown samples and crystals that were particularly difficult to pick up. After picking up all layers, i.e. all graphene gates, hBN layers, and TMDs, the final stack is melted off the stamp, as before, onto the final substrate at close to 200°C. At the end, low vacuum annealing ($< 10^{-8}$ mbar) at 200-300°C for 12 h is performed to increase the binding between the layers and reduce residue distribution between the layers of the stack [203].

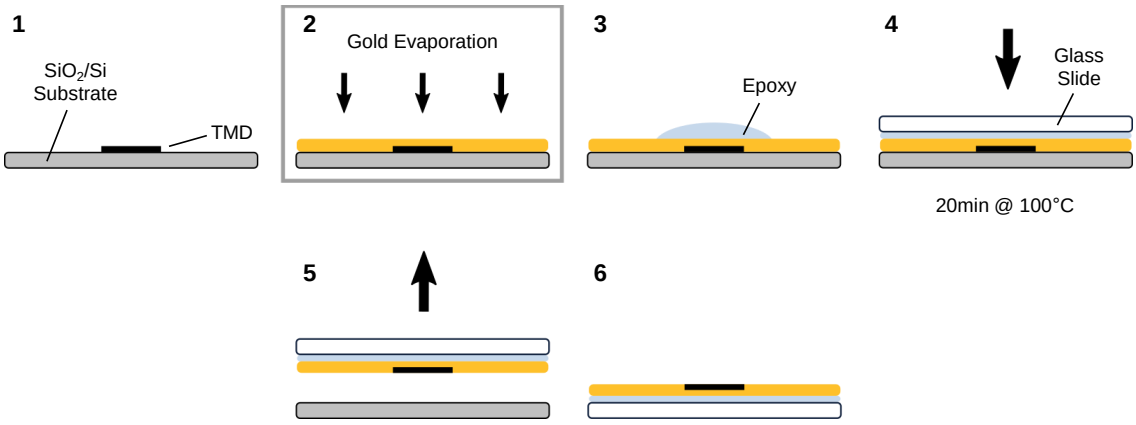

Figure 3.7: Pick-up sequence for transfer to gold (Au) substrate. The sequence starts with a TMD sample on a SiO_2/Si substrate (step 1). After gold evaporation in a high-vacuum chamber (step 2), epoxy is placed on top of the gold (step 3) which is pressed down using a conventional glass slide (step 4). To cure the epoxy, the stack is subjected to 100°C for 20 min on a hotplate. The pick-up of the glass slide detaches the gold and the TMD from the initial substrate (step 5), leaving the TMD transferred on the gold (step 6).

3.2.2 Gold substrate transfer

The method described here represents a transfer method from the initial substrate (SiO_2/Si) onto a gold (Au) substrate without subjecting the TMD sample to any polymer or chemical. This method was chosen for the study of MoS_2 on gold in scanning tunneling microscopy (STM) [P4] for which the sample needed to be atomically clean, as well as contacted to a metal to prevent charge accumulation.

The process is illustrated in Fig. 3.7. After the growth of the TMD on a 285 nm SiO_2/Si substrate, 90 nm of gold was evaporated onto the surface in a conventional high-vacuum evaporation chamber. Afterwards, epoxy (Epo-Tek®H74 30Z) was placed on top of the gold and a conventional glass slide was pressed by hand onto the epoxy to glue the gold onto the glass slide. After curing on a hotplate at 100°C for 20 min, the entire stack could be separated at the Au/SiO_2 interface. This step may need the help of a scalpel or other object to forcefully separate the gold. The TMD, however, would stay attached to the gold and stay as clean as possible, without any contact to wet chemicals or encapsulation material.

3.2.3 Crystal carving

Not only are CVD-grown TMD monolayers more difficult to pick up from their growth substrates than exfoliated samples. There are instances, especially in multilayer growth, where the crystal edge is not a clean crystallographic edge but where excess precursors have accumulated such that small bulky structures occur on the edges of otherwise smooth layers. Since the entire crystal is picked up from the edge, these bulky structures hinder the binding to hBN and either prevent the monolayer from being picked up or lead to damage to the crystal through a partial pick-up. For these reasons, the technique presented here has been developed. The technique employs the tip of an atomic force microscope (AFM) in contact mode with the surface to move along the surface and carve away single lines of monolayer material, as illustrated in Fig. 3.8 a. Initially, the tip is scanned over the crystal in tapping mode to acquire a topographic map of the crystal and align the scanning direction as close as possible with the crystallographic orientation. Afterwards, the mode is changed into contact mode to a deflection voltage of around 8 V, measured at the piezo of the AFM. Clean results have been achieved with a carving resolution above 6 lines per μm. The result of the process is depicted in Subfigure 3.8 b. After scanning, the crystal is surrounded by residue material. This should be removed using a polycaprolactone (PCL) stamp, as described above, to later allow any hBN used for pick-up to bind thoroughly to the material layer. PCL is highly adhesive above its glass transition temperature of 60°C [201] and due to its liquidity at this temperature very effective in cleaning the TMD residues. After carving, the substrate around the material layer is exposed to the PCL polymer film, as indicated by white dashed lines in Subfigure b. The substrate is heated to 60°C and cooled again. Subsequently, the polymer as well as the carved-off material is removed. The result is displayed in Subfigure c, upper left. In comparison with an uncarved crystal, the multilayer is picked up more easily and, as seen in Subfigure c bottom, more cleanly.

The technique had independently been developed to fabricate μm-scale wire-type structures in TMD to prevent the need for lithography steps based on chemical treatments [204, 205]. It also has been employed in graphene samples [206, 207], in particular it has been used for the fabrication of twisted homobilayers of graphene with a high-resolution control of the twist-angle [208]. Hereby, a monolayer is carved in two parts which results in two atomically aligned layers. Consecutive pick-up and stacking of the two layers gives control of the interlayer twist-angle with the resolution of the sample stage's rotation mechanism.

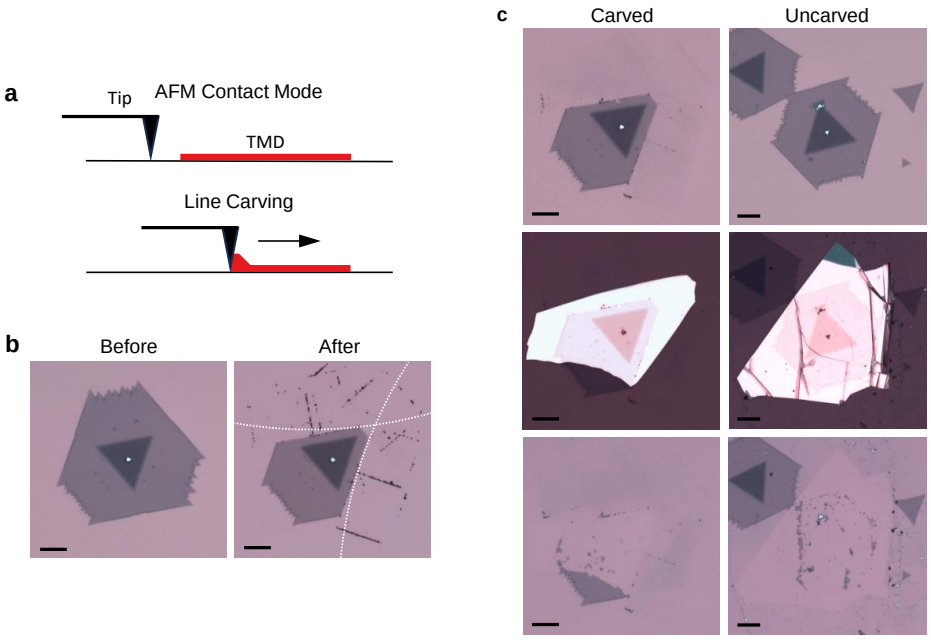

Figure 3.8: The crystal carving technique. **a**, An illustration of the technique using the tip of an atomic force microscope to carve away single lines of TMD material. **b**, Result of the technique. Carving leaves material residue which can be removed using a polymer stamp (see Section 3.2.1) based on polycaprolactone (PCL). The polymer contacts the substrate around the sample as indicated by white dashed lines around the TMD crystal. Consecutive heating above the glass transition temperature of 60°C [201], cooling, and removing of the polymer collects the residues. **c**, Pick-up with the carving result after cleaning (upper left), the consecutive coverage of the crystal with hBN layers (center) and the leftover on the substrate after pick-up (bottom). Apart from the lower corner, the pick-up of the carved crystal leaves less residues on the substrate.

3.2.4 Edge contact through etching

The method described here can be used under various circumstances and is based on an etch process of hBN as developed here [209]. The method was used as an alternative for a heterobilayer sample (*Sample 3*, Fig. 5.12) for which the contact through a multilayer-graphene was lost during fabrication. Laser lithography is used for various samples in this thesis to contact top and bottom gates as well as the contact multilayer-graphene and was usually done at a LPKF ProtoLaser system (1-μm resolution at 375 nm wavelength) with 170 mJ/cm^2 exposure power. AZ®MIR 701 was used as positive photoresist, spin-coated at 4000 rpm for 30 s, and softbaked for 2 min at 90ř◦C. Post-bake, i.e. after irradiation, was done at 110ř◦C for 90 s and development was done in a bath of AZ®MIF 726 developer for 90 s.

The etching method in hBN used a Heidelberg Instruments μMLA (sub-μm resolu-

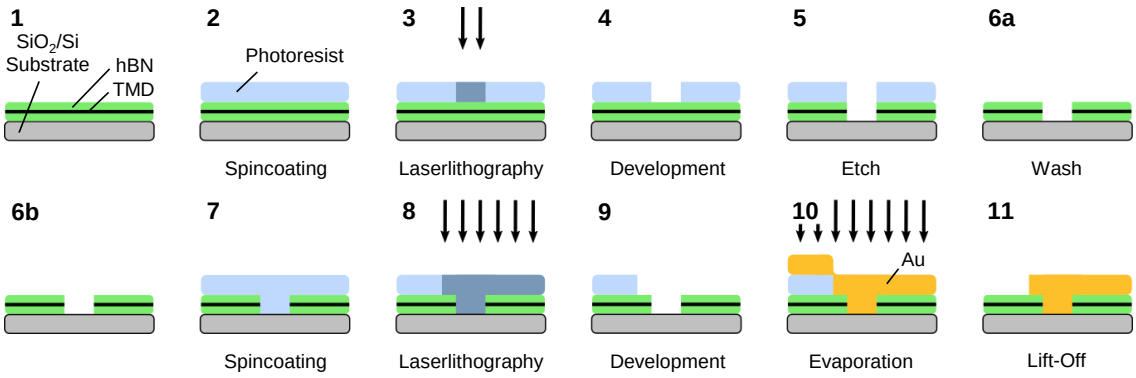

Figure 3.9: Edge-contact fabrication using laser lithography and reactive ion etching (ICP). The process follows a series of steps in laser lithography to create a small hole inside the photoresist (of μm scale) through which ICP etching is done to etch away hBN as well as part of the TMD. In a second step (steps 6b - 11) a contact geometry is written again using laser lithography and filled by evaporation of 3 nm of titanium and 90 nm of gold. The titanium increases bonding to the gold. After lift-off (step 11), the desired gold contact remains, contacting the TMD from an edge and leaves part of the sample exposed for optical access.

tion at wavelength 365 nm) with an exposure of 200 mJ/cm^2 for the laser lithography step. The positive photoresist AZ®5214E was used which is spincoated at 6000 rpm for 45 s. Softbake followed at 105°C for 60 s and development using AZ®826 MIF for 45 s. The method is illustrated in Fig. 3.9. The directional reactive ion etching (RIE) (step 5) uses a Oxford PlasmaLab 100 ICP-RIE system with the inductively coupled plasma (ICP) method at 300 W ICP and 300 W RF power at a frequency of 13.56 MHz. The DC bias of the sample is set to 30 V which resulted in an etch rate of roughly 0.76 nm/s. Since the system was not able to keep up the etch rate constantly, multiple etch cycles needed to be executed with assurance of the etch rate via AFM measurements. The washing step (6a) is done by gently dipping the sample in acetone (ACE) and isopropyl alcohol (IPA) in that order, for roughly 4 min each. The evaporation inside a BesTec UHV evaporator deposits 3 nm of titanium first, to increase bonding to the gold, before evaporating 90 nm of gold (Au). Lift-off is done similar to washing in ACE and IPA, however 10 min of ACE bath is done initially with a sequence of ACE and IPA done multiple times until the lift-off is complete. A pipette can be used inside the ACE bath to gently increase the mechanical stress on the gold through the creation of currents and swirls inside the ACE.

3.3 Optical spectroscopy

To study excitonic physics in TMD based van der Waals heterostructures optically, a low-temperature confocal microscope setup in reflection configuration, see Fig. 3.10, is employed for most studies in this thesis unless otherwise described. Hereby, the sample is placed either in a liquid helium bath (inside of a microscope shielding tube filled with helium exchange gas) or in a closed-cycle dry-cryostat with a base temperature of 3.2 Kelvin (attocube systems attoDRY1000 or attoDRY800) to minimize thermal effects in the system. Light is guided to and from the sample through optical fibers and after collimation (through attocube systems RT-APO/NIR-IR/0.13 collimators), filtering, and polarization manipulation (depending on the measurement), is focused into the sample plane using low-temperature apochromatic objectives (attocube systems LT-APO/VISIR) with numerical aperture in the range from 0.70 to 0.82. As light sources, either lasers are used (diode lasers with 635 nm or 532 nm), or white light sources (NKT Photonics Super K Varia and Super K Extreme) or a tungsten halogen lamp (Ocean Optics HL-2000-HP). Through beam samplers along the path, the excitation intensity is measured via a photodiode and the sample is located on the substrate using the CCD camera with the sample located in the optical image plane. Depending on the measurement, the signal light is guided to a detection modality, e.g. a spectrometer (Roper Scientific Acton SP2500 with a 300/1200 grooves/mm grating).

Photoluminescence (PL) spectroscopy was performed under coherent laser light excitation with a long-pass/short-pass filter combination in the detection/excitation arms in accordance with the chosen excitation and detection wavelength. Excitonic resonances in PL spectra where fitted using a pseudo Voigt function of energy E [210], according to

$$V(E) = fL(E) + (1-f)G(E), \tag{3.1}$$

which consists of contributions from a Lorentzian $L(E)$ and a Gaussian $G(E)$ in a ratio specified by the parameter f. For the Lorentzian, the formula

$$L(E) = \frac{2A/\pi\gamma}{1+4\left(\frac{E-E_{res}}{\gamma}\right)^2} \tag{3.2}$$

holds and for the Gaussian

$$G(E) = \frac{A}{\gamma}\sqrt{\frac{4\ln(2)}{\pi}}\exp\left[-4\ln(2)\left(\frac{E-E_{res}}{\gamma}\right)^2\right]. \tag{3.3}$$

Where E_{res} denotes the resonance position, γ the full width at half maximum (FWHM), and the area under the curve is given by A. Through the Lorentzian and Gaussian functions the Voigt profile reflects homogeneous and inhomogeneous broadening mechanisms, respectively. Homogeneous broadening mechanisms consist of dephasing between the crystal ground and exciton states, for example through exciton-exciton interactions or exciton-phonon scattering, or the corresponding population relaxation rate. Inhomogeneous broadening mechanisms can be caused through local potential differences through defects and impurities [211]. Differential reflection measurements are performed without filters under white light irradiation. The acquired signal I_{DR} then follows the convention

$$I_{DR} = \frac{I_{BG} - I_R}{I_{BG}}, \tag{3.4}$$

where I_{BG} denotes the back reflected intensity from a suitable background, e.g. top and bottom hBN on SiO_2, and I_R the reflected intensity of the region of interest. Line shapes, including peak positions and line widths, are fitted using a Fano line shape [212, 213]. This effectively fits the line shape as a result from the interference of the exciton signal with its back-reflection from the underlying substrate. As a function of energy E, the Fano line shape is according to

$$F(E) = \frac{\left(\frac{q\gamma}{2} + E - E_{res}\right)^2}{\left(\frac{\gamma}{2}\right)^2 + (E - E_{res})^2} \tag{3.5}$$

with resonance position E_{res}, full width at half maximum γ, and Fano parameter q. For the actual fit, an amplitude as well as background offset were included.

3.4 Energy-dispersive X-ray spectroscopy

Energy-dispersive X-ray (EDX) spectroscopy is a powerful tool to study materials and their composition [214, 215]. Through inelastic scattering of primary electrons within a scanning electron microscope (SEM), see Fig. 3.11a and b, X-ray radiation is created within the sample, characteristic of its constituent atoms. These X-rays are generated when an electron close to the atom's nucleus, i.e. the inner shell, is kicked out, leaving behind an electron vacancy, Fig. 3.11c. This vacancy is filled from an outer shell electron under the emission of electromagnetic radiation in the X-ray regime, characteristic to the underlying electron transition and thereby the corresponding element. If the resulting energy does not lead to Auger electrons, the characteristic X-rays can be

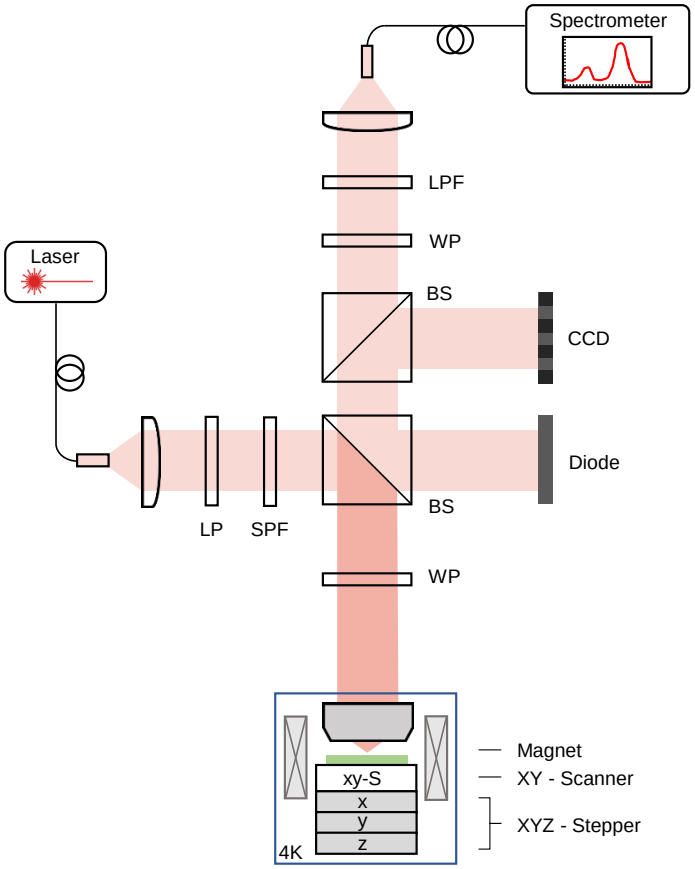

Figure 3.10: Optical experimental setup for various spectroscopic measurements. The sample (green) is mounted on piezoelectric nanopositioner steppers (attocube systems ANPx,z101) and scanners (ANSxy100lr/LT) inside a liquid helium dry-cryostat (typical attocube systems attoDRY1000 or attoDRY800) equipped with or without vector magnets. A low-temperature objective (attocube systems LT-APO/VISIR) is placed directly on top of the sample. The optical head on top of the cryostat uses a fiber to guide light into the excitation arm where it is collimated through a lens, linearly polarized (LP), and filtered (SPF, short-pass filter in photoluminescence (PL) configuration). The light is reflected towards the sample through a beam sampler (BS, 90/10 beam sampler) where 90% of light is transmitted to measure the beam intensity via a photo diode. The polarization of the reflected light can be altered by a wave plate (WP), e.g. a $\lambda/4$-WP for the measurement of the degree of circular polarization. After interaction with the sample, the back-scattered light is collected in the upward direction where again a wave plate can be included, e.g. a $\lambda/2$-WP for degree of polarization measurements or a $\lambda/4$-WP for polarization selective PL or differential reflection (DR) measurements. In PL, a long-pass filter (LPF) separates signal from excitation light which is collected through a collimation lens an guided via an optical fiber to a detection modality, e.g. a spectrometer.

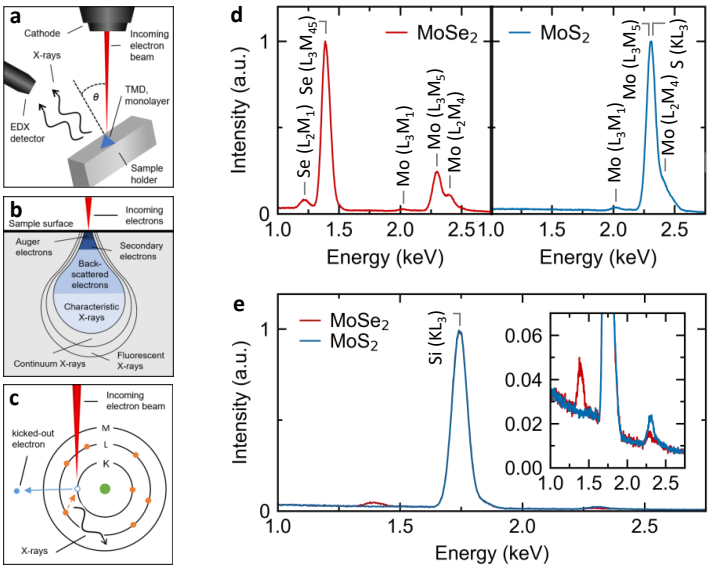

Figure 3.11: Energy-dispersive X-ray spectroscopy for atomic concentration determination in $MoSe_2$ and MoS_2. **a**, Setup illustration of an X-ray detector mounted inside the scanning electron microscopy (SEM) chamber. **b**, Physical scattering processes at different penetration depths inside the sample. **c**, Generation of characteristic X-ray radiation inside an atom. **d**, Spectra of bulk material with strong signal peaks stemming from the noted transitions according to [217]. **e**, The signal stemming from monolayer $MoSe_2$ and MoS_2. In contrast to bulk, the underlying substrate is strongly visible in the spectrum in the form of the KL_3 line of silicon at 1.739 keV, which is used to normalize each spectrum. The inset shows the low-intensity peaks of the spectrum with a strong background stemming from Bremsstrahlung. Figures a, b, and c are taken from [200]. Data for bulk spectra in d are taken from [P9].

detected and analyzed [216].

Figure 3.11d displays the spectra of such X-ray signals stemming from bulk $MoSe_2$ and MoS_2. The naming convention describes the inner atomic shell to which an atom relaxes to (e.g. K, L, M, etc.) with the sub-shell as subscript (e.g. 1, 2, 3, etc.), followed by the letter and subscript corresponding to the originating electron shell. Attribution of the peaks has been done using data from [217]. Notably, in MoS_2 the transition-metal and chalcogen signals superimpose in the spectrum whereas in $MoSe_2$, chalcogen signal can clearly be resolved from the transition-metal. For the determination of chalcogen concentration in TMD alloys (Section 5.2), the $Se(L_3M_{45})$ peak is used to assign selenium concentrations in the samples.

3.4.1 Atomic layer resolution

To achieve high-resolution inspection of atomically thin TMDs and their composition down to the monolayer limit, we used a SEM (Zeiss LEO DSM982) at 5 keV electron beam energy equipped with an EDX detector (Oxford Instruments, X-Max^N 50Standard) mounted 35° between the detector axis and the plane of the sample in 7.5 mm distance from the sample with an aperture of 30 μm and a sample tilt-angle of 75° between the electron beam and the sample plane's normal. Due to the minimal interaction volume inherent to monolayer materials with thicknesses below 1 nm, operational parameters were optimized through a combination of numerical simulations and empirical calibrations. Key optimization steps included adjusting the sample tilt-angle with respect to the primary electron beam to increase the interaction volume, as well as fine-tuning the electron beam energy to balance between penetration depth and ionization efficiency. These methodological enhancements enabled layer-resolving sensitivity for few-layer TMDs and provided elemental composition profiling in both vertical and lateral heterostructures of TMDs.

Spectra from 5 down to the single layer limit for $MoSe_2$ and MoS_2 for exfoliated samples are shown in [P9] with the signal from the exfoliated monolayer matching that of the monolayer result from CVD. The signal from grown monolayers of both $MoSe_2$ and MoS_2 are displayed in Fig. 3.11 e, taken with the settings listed above and an integration time of 50 min. The layer number had been confirmed through optical imaging contrast as well as photoluminescence and Raman spectroscopy. Prominently, the substrate is visible in the form of the KL_3 line of silicon at 1.739 keV, which was used to normalize for all cases. In the incut, the low-intensity spectrum is shown with a prominent background resulting from continuous Bremsstrahlung of the incident electrons propagating through the sample and the substrate. While the spectra of both materials display superimposing peaks between 2.2 and 2.5 keV, the L_3M_{45} at 1.379 keV of selenium is distinct and clearly visible. This peak is used to assign alloy degree values between the chalcogens, i.e. the sulfur content in $MoSe_{2(1-x)}S_{2x}$.

Chapter 4

Monolayer growth via chemical vapor deposition

Intense progress of two-dimensional material research is marked by the early studies on graphene by Novoselov and Geim as introduced in Chapter 2. Apart from the isolation of graphene, they also introduced a new method to isolate single two-dimensional layers from van der Waals bulk allotropes: mechanical exfoliation, a process which uses sticky tape to peel off layers from the bulk and deposit them in a thermal process onto a substrate [3, 5]. Even though the low-yield method worked for scientific experiments it hampered technological advancements at scale [218]. And while mechanical exfoliation has improved over time to increase yield and quality [219, 220], different methods are needed to fabricate high-quality two-dimensional materials for industry adoption.

Chemical vapor deposition (CVD) is a widely-used vapor-phase deposition technique promising to overcome the hurdles posed by industry adoption for TMDs. If implemented successfully, the technology would mark a significant step towards atomic scale bottom-up manufacturing. Synthesis of thin film transition-metal dichalcogenides (TMDs), even down to single layers, goes back to the 1980's in the form of molecular beam epitaxy, more specifically van der Waals epitaxy [221, 222]. Here, the lack of dangling bonds on the surface of two-dimensional materials is used to grow heterostructured atomically clean interfaces between materials of different lattice constants. Single layers of NbS_2 [223, 224] and $MoSe_2$ [225, 226] were grown in vacuum under electron beam evaporation of the transition-metals. More recently, growth methods on MoS_2 were optimized to reach crystal lengths from several atoms [227], to several μm [228–231], and finally several 100μm [232, 233]. Similar methods have been reported for $MoSe_2$ [234, 235], WSe_2 [236–238], and WS_2 [230, 239–242]. Notably, these studies specifically are concerned with single-crystal growth. This excludes methods

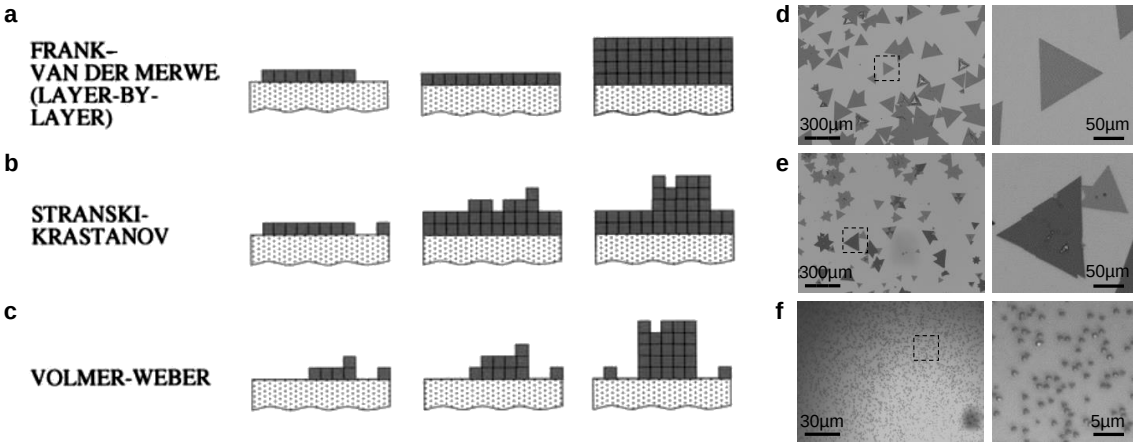

Figure 4.1: Classical growth modes. **a, b, c**, Growth modes as defined by E. Bauer [253, 254], illustrations taken from [255]. **d, e, f**, The respective grow results under different growth conditions. Difference in optical contrast due to different microscope and lighting conditions. The zoomed-in image on the right corresponds to the indicated cutout on the left.

to grow monolayer thick polycrystalline sheets, which already reach wafer scale dimensions [2, 243–252]. The following section will deal with the general CVD growth mechanism of TMDs and its dependencies in detail.

4.1 Theoretical considerations

The goal of this section is to establish a theoretical framework for the formation of atomic monolayer single-crystals in a CVD process and to establish a link from theoretical considerations to specific growth parameters. This chapter mainly relies on the textbooks by Hans J. Scheel and Tsuguo Fukuda [256] and Yukio Saito [257] for crystal growth theory, as well as argumentation from V. Voronenkov et al. [258]. These references, as well as others, are cited correspondingly.

An intuitive understanding of growth results can be drawn from considering the phase change from a non-condensed phase into a crystalline phase, as established by E. Bauer [253], by considering a liquid droplet wetting the surface of a substrate surrounded by some vapor. This differs from vapor phase deposition, however the underlying growth modes share similarities since in both cases material growth heavily depends on the bonding between the source material and the substrate. In the case of the droplet, the initial shape is determined by the wetting angle θ which is used to formulate the equilibrium condition between the three phases of the liquid film, the

solid substrate, and the vapor. The condition is the Young equation [259]:

$$\gamma_{SV} = \gamma_{FS} + \gamma_{FV} * \cos\theta \tag{4.1}$$

where γ_{SV}, γ_{FS}, and γ_{FV} respectively denote the free interfacial energies between the substrate-vapor, film-substrate, and film-vapor phases. For $\theta \rightarrow 0$, i.e. significant wetting, we would expect layer-by-layer growth of TMD crystals where

$$\gamma_{SV} = \gamma_{FS} + \gamma_{FV}. \tag{4.2}$$

This is referred to as the Frank-Van der Merwe growth mode [260], as depicted in Fig. 4.1a and d. In the case of small wetting, i.e. high wetting angle,

$$\gamma_{SV} < \gamma_{FS} + \gamma_{FV} \tag{4.3}$$

where the deposition will occur on discrete nuclei with three-dimensional crystal growth occurring preferably. This is referred to as the Volmer-Weber mode [261], as depicted in Fig. 4.1c and f. The intermediate case in which the film-substrate interaction is stronger than the binding within the film is called Stranski-Krastanow mode [262], where

$$\gamma_{SV} > \gamma_{FS} + \gamma_{FV}. \tag{4.4}$$

In this case, after the initial monolayer due to high wetting, bilayer, multilayer, and bulk material will grow, as illustrated and depicted in Fig. 4.1b and e, respectively.

In the crystal growth process directly from vapor, the outcome is determined not only by the nucleation process itself, but also by the nucleation density, which is influenced by the lateral transport of precursor particles. Figure 4.1f depicts an example of relatively high nucleation density growth in which crystal seed distances are on the order of μm. These crystals, assuming monolayer growth is ensured, can grow larger over time until they merge into a connected polycrystalline film [246, 263]. Considering surface diffusion as the only lateral transport mechanism, low surface diffusion will lead to short diffusion length and to high nucleation site density. Surface diffusion at a temperature T is described by the Einstein equation of the mean displacement x_S of adsorbed particles:

$$x_S = \sqrt{D_s \tau_S}, \tag{4.5}$$

where τ_S is the mean life of an adsorbed particle before desorption into the vapor takes place. The diffusion coefficient is expressed as

$$D_s = a^2 \nu \exp(-\frac{U_S}{k_B T}), \tag{4.6}$$

where a is the distance between two neighboring equilibrium positions on the surface, U_S the activation energy between these two sites, and k_B the Boltzmann constant [264]. ν is a frequency factor corresponding to the vibration frequency of the adsorbed molecule.

In the case of TMD precursors on SiO_2, it is believed that surface diffusion is limited to $\sim 1-2\mu$m distances within the temperature and carrier gas flow ranges that maintain the specific out-of-equilibrium conditions of the crystal growth. This effect is similar to GaAs grown on SiO_2 [258, 265, 266]. For TMDs, this has been indicative in numerous large-area growth studies [2, 243–245]. Other examples include MoO_3 precursors in MoS_2 growth on SiO_2 [267] or for $W(CO)_6$ precursors in WSe_2 growth on sapphire [268]. Therefor, the increase of crystal seed distances to several 100 μm through a low nucleation density, as depicted in 4.1a and d, might not be possible through surface diffusion only - a different lateral transport mechanism must occur. This mechanism was identified as gas-phase diffusion [258], a type of lateral surface transport proceeding precursor adsorption to, and/or following precursor desorption from, the substrate surface. If the precursor desorption rate is increased while keeping precursor adsorption and surface diffusion constant, gas-phase diffusion transport is increased and thereby nucleation site distances - the precursors are not able to bind to the surface within their diffusion lifetime. This process allows to increase lateral precursor transport while keeping the deposition process in the desired range close to equilibrium.

For precursor atoms in the ideal gas phase at temperature T and pressure p the velocity distribution of a monoatomic ideal gas will follow the Maxwell distribution:

$$P(\boldsymbol{v})d\boldsymbol{v} = (\frac{m}{2\pi k_B T})^{3/2} \exp(-\frac{m\boldsymbol{v}^2}{2k_B T})d\boldsymbol{v}, \tag{4.7}$$

where $\boldsymbol{v} = (v_x, v_y, v_z)$ is the velocity of a precursor particle and m is its mass, see Fig. 4.2a. In the case of TMDs it is sufficient to consider only the metal precursors with $m = m_{Me}$ at partial pressure $p = p_{Me}$ to be limiting to the deposition process since the chalcogen precursor concentration is assumed to be much larger than metal precursor concentrations [258]. Considering the ideal metal precursor gas now on top of a crystal surface with the surface normal pointing in z-direction, as depicted in Fig. 4.2a, the number of precursors impinging upon the surface per unit time can be calculated by

$$f = \int_{-\infty}^{\infty} dv_x \int_{-\infty}^{\infty} dv_y \int_{-\infty}^{0} dv_z n_{Me}|v_z|P(\boldsymbol{v}) = \frac{p_{Me}}{\sqrt{2\pi m_{Me} k_B T}} \tag{4.8}$$

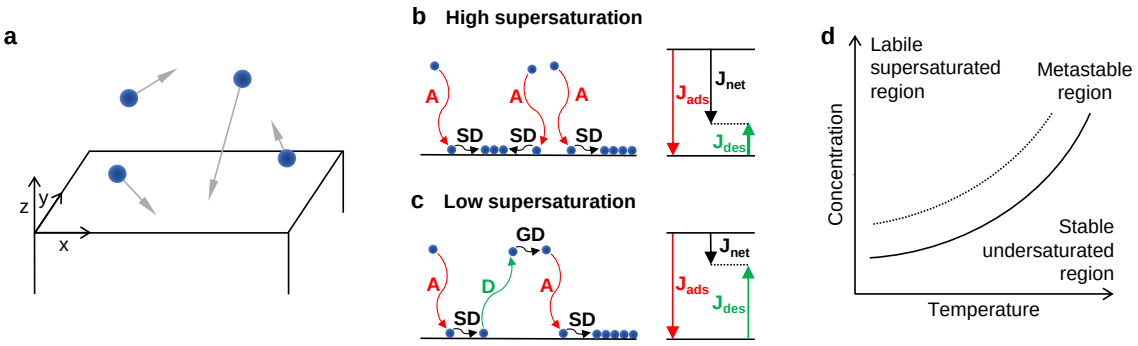

Figure 4.2: Illustration of crystal growth from the vapor phase. **a**, Vapor atoms impinging upon a flat surface. **b**, High supersaturation causes atoms to adsorb to the surface and, following surface diffusion (SD), to nucleate either directly onto the surface forming new nucleation sites or at already existing nucleation sites. The desorption rate J_{des} is low while the net deposition rate, J_{net}, is high. **c**, High supersaturation and resulting increased gas-phase diffusion (GD) suppresses direct nucleation resulting in a high desorption flux and low net deposition flux. If supersaturation is within the Ostwald-Miers metastable region, the deposition will only occur on existing nucleation sites or growth seeds. **d**, Illustration of the metastable region of nucleation. Figures **a**, **b/c**, and **d**, adopted from [257], [258], and [256], respectively.

where $n_{Me} = p_{Me}/k_b T$ denotes the average number density of precursor atoms. If p_{Me}^{eq} denotes the equilibrium pressure of the crystal at which the desorption rate equals the deposition rate, the growth rate can be written as the deviation from the equilibrium pressure:

$$J_{net} = J_{ads} - J_{des} = \frac{p_{Me} - p_{Me}^{eq}}{\sqrt{2\pi m_{Me} k_B T}}. \tag{4.9}$$

with the adsorption and desorption rates J_{ads} and J_{des}, respectively. This is the Hertz-Knudsen equation [269, 270], named after the scientists among the first to study evaporation dynamics [271]. In the limiting case of a surface-reaction-limited deposition with $J_{net} \approx 0$, the partial pressure at the surface will equal the partial pressure of the gas. Hence,

$$J_{des} \approx J_{ads} = \frac{p_{Me}}{\sqrt{2\pi m_{Me} k_B T}}. \tag{4.10}$$

In the opposing case of an infinitely fast surface reaction, the gas mixture close to the surface will be heavily depleted of metal precursor molecules and the partial pressure at the surface will equal the equilibrium pressure. Consequently, adsorption to the surface occurs via diffusion through the depleted boundary layer and is described by Fick's law of diffusion [272]:

$$J_{net} \approx D_{Me} \frac{p_{Me} - p_{Me}^{eq}}{\delta}, \tag{4.11}$$

where D_{Me} is the metal precursor gas-phase diffusion coefficient and δ denotes the boundary layer thickness. The desorption rate will be

$$J_{des} = \frac{p_{Me}^{eq}}{\sqrt{2\pi m_{Me} k_B T}}. \tag{4.12}$$

In order to increase the desorption rate, there are now two approaches as discussed by [258]. The first approach is to take the reaction out of equilibrium by lowering the growth temperature where the desorption rate will follow equation 4.10. Reducing deposition by taking the growth reaction out of equilibrium is, however, associated with low crystalline quality and defect density. The second approach is to stay in a regime of fast surface reaction, but to reduce supersaturation, see Fig. 4.2b and c. In the case where supersaturation lies within the Ostwald-Miers metastable region, see Fig. 4.2d, nucleation will be prohibited in the absence of nucleation seeds. The desorption rate would follow 4.12 which, next to lowering temperature, can be increased by increasing p_{Me}^{eq}. This is achieved not only through temperature, but through the composition of the gas, which, in the case of the experiment, means to adjust powder amounts, powder evaporation temperatures, and hydrogen gas concentration (see Fig. 3.3). The very last approach forms the basis for growth optimization in the following chapter.

As discussed in Chapter 3, precursor mobility can be increased by the overall flow rate $Q = q_{Ar} + q_{H_2}$. It can be noted, however, that the flow rate acts as an essential parameter to all other fundamental parameters, in the sense that changing it will not only change precursor mobility but also precursor concentration or even change precursor temperature (due to the finite exposure time of chalcogen precursor to the high-temperature growth chamber). Therefor, the flow rate is kept constant at a high level (300 sccm of argon) within ±10 sccm, to keep all other parameters undisturbed and to stay at the upper limit of surface diffusion achievable through precursor mobility while staying within a regime of laminar flow. However, through changing the composition of the gas, i.e. q_{Ar} and q_{H_2}, the metal precursor concentration can be tuned.

Finally, tuning the precursor density and composition, particularly p_{Me}^{eq}, can be monitored by the growth result on the substrate. To fine-tune the density and composition close to equilibrium, the overall crystal shape can give sufficient indications [273, 274], as shall be discussed below in Section 4.2.3. For growth conditions far out of equilibrium, either no growth at all will take place, or chaotic multilayers will form, often with

edges ranging from multiple spikes of various angles to fully round, due to an overwhelming amount of defects in the crystalline structure. For very high temperature, different material phases are predicted to form [275].

4.2 Growth optimization

4.2.1 Substrate dimension

Initially, substrates were cut from a wafer using a diamond cutter. The resulting growth substrates displayed various forms and sizes which ultimately effected the growth result. Figure 4.3 shows the difference in growth for two substrates of different dimension. Both substrates stem from the same growth with their bottom edge touching the molybdenum precursor. Due to different flow dynamics, the growth varies along the flow (x)-direction. The wider substrate (Subfigure b) displays a desirable close-to-equilibrium growth towards the center, with crystals growing well-separated. On the narrower substrate (Subfigure a) crystals almost form a continuous polycrystalline film. In addition to the displayed difference in substrate width, the difference in height results in a difference in angle of the substrate inside the boat, further influencing the growth result. Since multiple substrates are placed next to each other inside the boat, differences in growth interfere across all substrates in the form of precursor concentration differences. Therefor, pre-cut 1x1 cm substrates were employed to circumvent dimensional differences and ensure consistent results.

4.2.2 Set-up improvement

Growth operation for monolayers was done in the setup configuration displayed in Fig. 4.4c which followed initial optimization steps that followed from Fig. 4.4a. Initially, chalcogen precursors were placed in their aluminum boats at certain positions upstream of the growth chamber. Due to variability in placing the boats, as well as a high temperature difference between the positions separated only by 1 cm from each other, this positioning was neglected for a setup that allowed for separate control of growth/transition-metal temperatures from chalcogen temperatures, expanding the parameter space significantly (see Fig. 3.3).

Additionally, temperatures were initially risen at a rate of 3-5°C/min below T_g = 450°C and 30°C/min above. This accumulated to a ramp-up duration of about 115 minutes. Over time, this ramp up duration could be reduced to 33 minutes, limiting

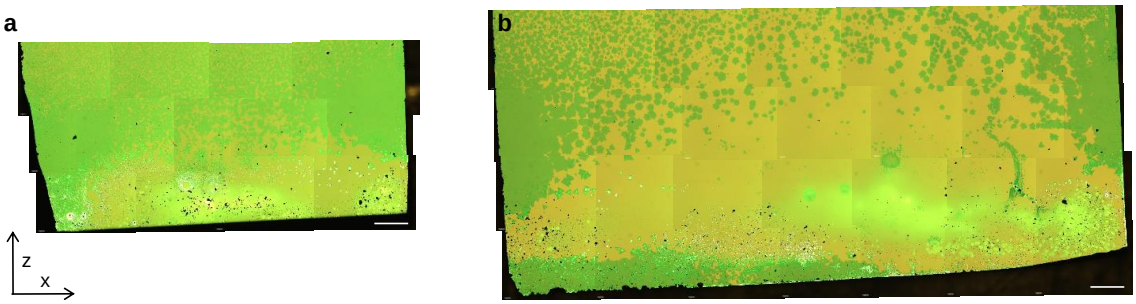

Figure 4.3: Substrate size comparison. Two substrates of different dimensions were used in the same growth, stemming from the same Si/SiO_2 wafer with a 285 nm oxide surface. The scale bar is 1 mm and applies to both substrates. **a**, Growth result on the narrow substrate displays the polycrystalline result. **b**, Growth result on the wide substrate displays a polycrystalline film towards the outside of the substrate in x-direction following the carrier gas and precursor flow direction. Towards the center, the growth of single crystals is well isolated from other crystals and therefor preferable to use in fabrication. It is this variation in growth result that led us to use pre-cut wafers of 1x1 cm substrates only. The bottom edge in both **a** and **b** is located close to the MoO_2 precursor, as displayed in Fig. 3.2 a. The variation of the growth result along the z-direction is therefor attributed with a varying molybdenum precursor concentration. The scale bar is 500 μm.

the total growth duration to about 50 minutes and thus greatly improving on the speed at which multiple runs could be undertaken.

4.2.3 Monitoring and quality feedback

As mentioned in Section 4.1, the overall crystal shape can be used to fine-tune the precursor densities and composition around the growth equilibrium, see Fig. 4.5 and 4.6, as has been observed by others as well [273, 274, 276]. The corresponding precursor concentration in the growth environment is hereby mainly tuned through the amount of precursor material, its temperature, and, for the molybdenum precursor, the flow of hydrogen (see Fig. 3.3) which acts as an agent for the oxygen reduction process. Next to these strong parameters, additional soft parameters, such as the overall pressure, the substrate, as well as its placement play a role. Overlapping effects are visible for $MoSe_2$ in Fig. 4.6 where bi- and multilayer growth is initiated (Subfigures b and c), likely due to the increased growth time of $t_g^{Se} = 20$ min in this particular growth (compare Section 4.3.1 below), and more complex growth (Subfigure d) resulting from a strong imbalance in precursor concentrations in combination with particular high growth temperature of $T_g = 770°C$ (see Section 4.3.1 below).

For monolayers which display the characteristic monolayer contrast from the sub-

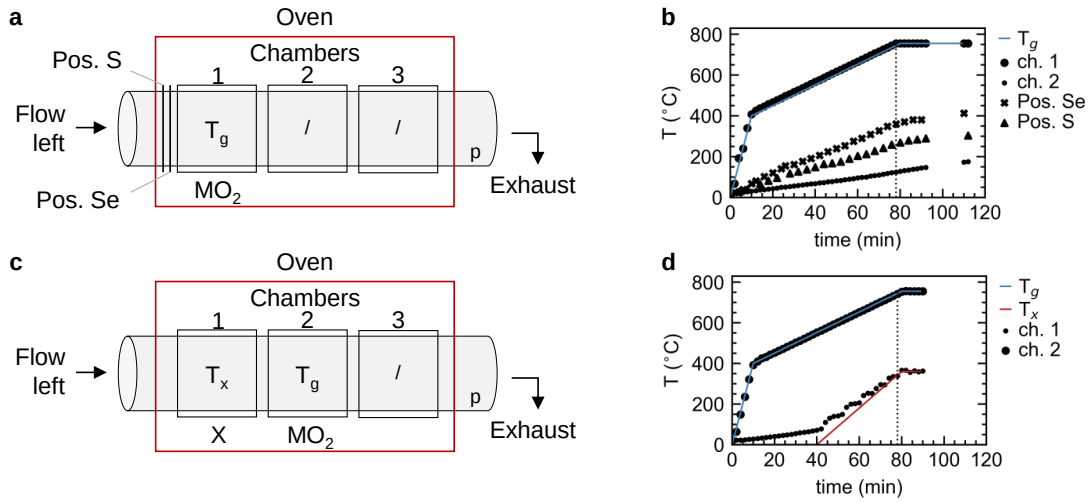

Figure 4.4: Growth setup improvement. **a**, Schematic of initial setup from [231] with indicated key parameters. Only chamber 1 of the furnace is heated at temperature T_g, which contains the growth substrates as well as transition-metal precursor powder, i.e. MO_2 with M being molybdenum or tungsten. Selenium or Sulfur are placed at their respective positions upstream. **b**, Respective temperature measurements at key locations in the setup **a**. Set temperature T_g in chamber 1 (blue) exerts heat onto the positions of Selenium and Sulfur which display a significant temperature difference despite being 1 cm apart. **c**, Schematic of the improved setup, placing the chalcogenides, i.e. X=Se, S, Te, in chamber 1, separate from the growth chamber chamber 2, separating parameters ΔT_x and T_x from ΔT_g and T_g. **d**, Corresponding temperature measurement of setup in Subfigure **c**.

strate, a close investigation under the microscope is performed using bright-field microscopy. The imaging settings are set to high-contrast with the application of a gamma filter on all color channels (r, g, and b) with a set-in value of 155. Tuning the brightness will then move all color channels in and out of the range which is effected by the gamma filter. This further enhances the contrast and reveals inhomogeneities across the crystal. The effect is made visible in Fig. 4.7 for an as-defined homogeneous crystal (Subfigures a to e) and a inhomogeneous crystal (Subfigures f to j). The slight inhomogeneities become visible in Subfigures g and h.

4.2.4 Substrate differences

Studies on the growth behavior on different substrates have not been undertaken systematically in the scope of this thesis, even though different surfaces as well as different roughnesses most certainly effect the growth. However, growths have been performed on different oxide thicknesses, which might have an impact on growth

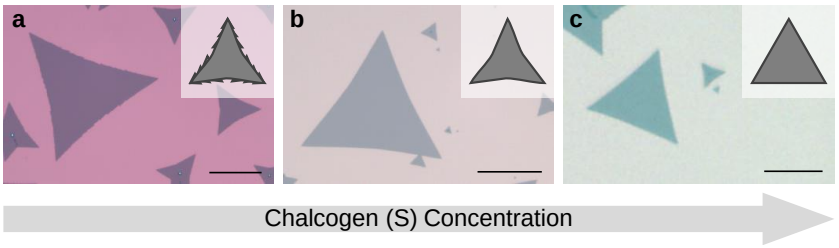

Figure 4.5: Chalcogen concentration monitoring close to growth equilibrium through the crystal shape. The material is MoS_2. The scale bar is 50 μm.

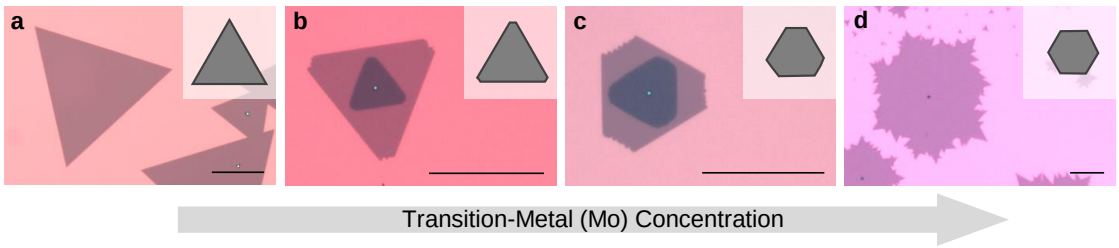

Figure 4.6: Molybdenum concentration monitoring close to growth equilibrium through the crystal shape. The material is $MoSe_2$. Other parameters also contribute to the result, such as a longer growth time which increases bilayer growth in **b** and **c**. **d**, Strong imbalance in precursor concentrations and increased temperatures lead to more defects and chaotic growth. The scale bar is 50 μm.

dynamics as well due to the underlying doped silicon in the low-thickness limit of the bare silicon wafer, or due to differences in surface roughness.

Figure 4.8 displays growth results for three cases: 85 nm SiO_2 on silicon, bare p-doped silicon, and bare SiO_2 which is represented by a common commercially available flat glass slide (VWR®microscope slides 631-1552). The bare silicon substrate usually hosts a thin oxide layer due to oxidation with the environment. If the oxide layer was minimal after processing in the factory, the resulting oxide thickness should be in the order of around 5 Å after the exposure to air for about 20 min after cleaning and proceeding growth [277]. Furthermore, the growths in Subfigure a and b can directly be compared, since the substrates stem from the same growth. So while on the SiO_2/Si substrate only very limited growth takes place, often displaying bilayer contrast, the growth on the bare silicon seems to work well. The layer thickness still needs to be confirmed, however, the growth of large, well-separated triangular crystals is evident. Lastly, the growth on the commercial glass slide also seems to work well. The substrates were cut into 10x10 mm squares to match the placement specifications of the other substrates. After growth, the substrates were bent, almost touching the MoO_2 powder. However,

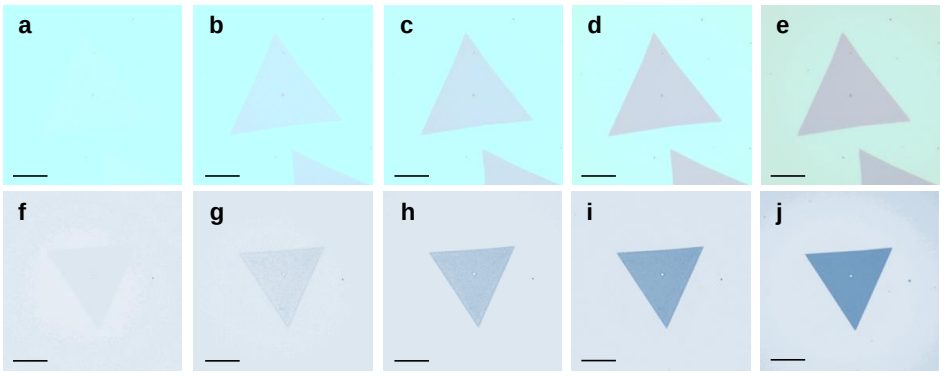

Figure 4.7: Quality control through optical bright-field imaging of $MoSe_2$ samples directly after growth. The contrast is maximized in combination with maximal gamma effect on all color channels with a set-in value of 155. **a** to **e**, The as defect-free defined crystal becomes visible homogeneously with decreased light intensity. **f** to **g**, A crystal that looks homogeneous at low light condition (**g**) displays a substructure under high light condition (especially **g** and **h**). Both crystals display a bi- or multilayer in their center, manifesting itself as dark or bright spot, respectively. Scale bar is 20 μm.

this does not seem to dampen the growth process.

4.3 Monolayer growth

4.3.1 Molybdenum-based growth

For molybdenum-based materials, i.e. MoS_2, $MoSe_2$, and $MoTe_2$, the setup is configured as displayed in Fig. 4.4 c. The precursors are: molybdenum(IV)-oxide (MoO_2) powder (≥ 99%, 234761, Sigma-Aldrich), sulfur powder (≥ 99.998%, 213292, Sigma-Aldrich), selenium powder (200 mesh, ≥ 99.999%, 36208, Alfa Aesar), and tellurium (≥ 99.999%, 204544, Sigma-Aldrich). The growth temperature is set to $T_g = 750°C$ with a temperature gradient set to $\Delta T_g = 50°C/\text{min}$ below and 5 °C/min above $T_g = 650°C$. The chalcogen temperatures and temperature gradients are

$$\begin{aligned} T_S &= 135°C, \quad \Delta T_S = 5°C/\text{min} \quad @T_g > 650°C \\ T_{Se} &= 390°C, \quad \Delta T_{Se} = 18°C/\text{min} \quad @T_g > 650°C \\ T_{Te} &= 750°C, \quad \Delta T_{Te} = \Delta T_g \end{aligned}$$

Notably, except for tellurium, all other chalcogen temperatures would only be increased after the growth chamber would hit 650°C. The amount of powders used were

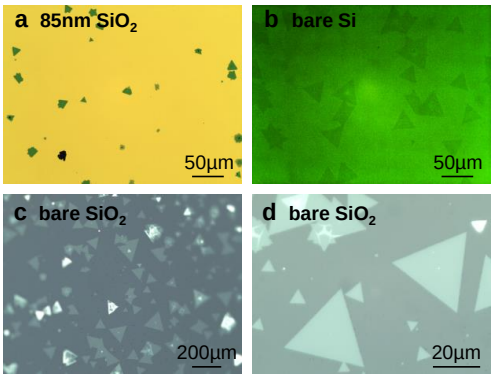

Figure 4.8: Growth results for different substrates. **a**,**b**, Result from the same growth run on 85 nm SiO_2 on silicon and bare silicon, respectively. The growth on the bare silicon seems to work particularly well in this case, which might be due to the underlying p-doped silicon underneath the thin oxide layer on the top of the substrate. **c**,**d**, Growth on unsupported SiO_2 from commercially available glass slides.

$$
\begin{aligned}
n_{MoO_2}/n_S &= 20/100\text{mg} \quad \text{for } MoS_2,\\
n_{MoO_2}/n_{Se} &= 40/100\text{mg} \quad \text{for } MoSe_2,\\
n_{MoO_2}/n_{Te} &= 40/400\text{mg} \quad \text{for } MoTe_2.
\end{aligned}
$$

However, powder amounts could be changed, for example whether three or four substrates were placed in the boat. For four substrates, additional 10 mg of MoO_2 were distributed inside the growth boat.

Other essential growth parameters are the growth times: $t_g^S = 15\text{min}$, $t_g^{Se} = 10\text{min}$, and $t_g^{Te} = 10\text{min}$, as well as the flow: $Q = q_{Ar} + q_{H_2}$. Usually, a high inert carrier gas flow of $q_{Ar} = 300\text{sccm}$ was used to increase carrier mobility on the substrate (Section 4.1). Hydrogen flow allowed for a precise but sensitive control of molybdenum concentration through controlled reduction of the oxide precursor. A low flow rate of $q_{H_2} = 0.75\text{sccm}$ was used with t_{H_2} chosen to match the $T_g > 650°\text{C}$ criterion. The cool-down was initialized after t_g by terminating hydrogen flow and opening the furnace with the help of the air fan at $T_g < 600°\text{C}$.

Figure 4.9 displays typical growth results for molybdenum based TMDs. Symetrical triangles are grown for $MoSe_2$. The MoS_2 usually displayed *pointy* triangles, most likely due to elevated chalcogen concentration in the system which leads to increased growth along the triangle directions [273], see Section 4.2.3. The close-up image displays that the edge is indeed not round but rather step-like, such that the crystal orientation is preserved. The $MoTe_2$ crystals display an overall different shape in accordance with other results [278–280], which points to the fact that $MoTe_2$ has been grown in the

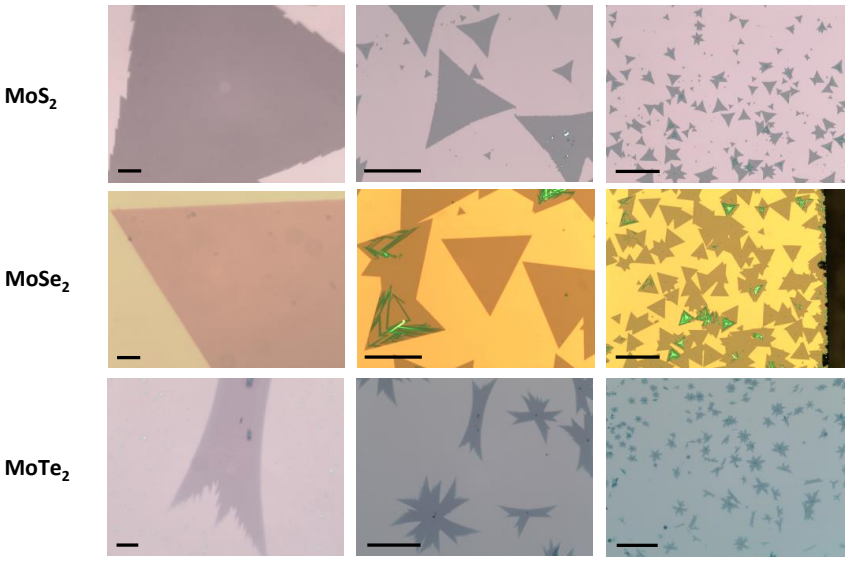

Figure 4.9: Molybdenum based monolayer growth results. Scale bars are (left to right): 10, 100, and 300 μm.

1T'-phase. Further experimentation would have to be conducted to grow the semiconducting 2H-phase. Earlier studies have pointed out that the 1T- and 1T'-phase could be transitioned into the 2H-phase by increased temperature during cool-down [279], during growth [281, 282], or by external manipulation such as electrostatic doping [283] or strain [284, 285].

Through the setup alterations and expansion of the parameter space (Section 4.2.2), reproducibility and sample quality could be improved. Reproducibility was especially helpful for publication [P7] in the process of which around 40 samples of stacked heterobilayers were fabricated, with many failed attempts that did not make the count. As a measure of quality we use the excitonic linewidth as the full width at half maximum (FWHM) of the PL peak or the differential reflection (DR) peak at low temperature [35, 286–289] and encapsulated in hBN [290]. In most samples, cavity effects of the encapsulating hBN layers had been considered to tune the exciton transition lifetime away from any minimas inside the weakly coupled cavity of hBN layers [291].

Figure 4.10 displays the optical result for all samples available in photoluminesence of hBN-encapsulated $MoSe_2$ monolayer at low temperatures of 4K under laser light excitation of 635 nm. The FWHM is determined from the fit (see Subfigure a, inset) of the pseudo Voigt function 3.3. In Subfigure a, the best result is plotted with the exciton resonance (X) at 1635.1336 ± 0.0016 meV with a FWHM of 1.062±0.007 meV, much

a

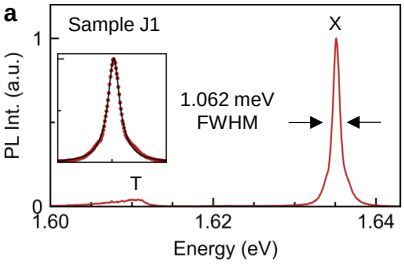

b

Sample	t/b-hBN (nm)	Spots (μm²)	Mean (meV)	Std (meV)	Min (meV)	Voigt Ratio
J1	70/280	1	-	0.007	1.062	1.000 ± 0.011
D1	55/56	47	1.6	0.5	1.3	0.55 ± 0.13
JS1	90/90	143	2.0	0.4	1.4	0.87 ± 0.18
JS2	95/85	1	-	0.06	1.50	0.81 ± 0.15
Other Samples from the Group						
S1M3	100/100*	309	2.9	0.6	2.5	0.82 ± 0.09
S2t53	100/100*	33	1.9	0.5	1.5	0.66 ± 0.15
S3M	100/100*	611	4.0	0.7	3.0	0.94 ± 0.15
S3M1	100/100*	7	5.7	0.4	5.2	0.3 ± 0.3

Figure 4.10: Optical linewidths in photoluminescence spectroscopy of encapsulated $MoSe_2$ at T=4K. **a**, Best result from sample J1 with FWHM of $1.062 pm 0.007$ meV at 1635.1336 ± 0.0016 meV, according to the Voigt fit, see incut and Section 3.3. A slight doping is evident from the charged trion T at 1.611 meV [292, 293]. **b**, Table of all samples grown with the method presented in this thesis (top) and other samples grown by colleagues in the group (bottom). Top (t) and bottom (b) hBN thicknesses are indicated in the second column taken from AFM measurements, marked values (*) were estimated from the optical contrast under the optical microscope. The *Spots* column indicates the number of diffraction-limited optical spots of the 635 nm excitation laser over which the data was averaged. The FWHM mean with the standard deviation across all spots are indicated in columns *Mean* and *STD*, respectively. The standard deviation for the single-spot samples is according to the fit result of the single spectrum. The minimum FWHM value across the set of data is listed in *Min*. Comparing the minimum and mean values indicates that the improved method of sample growth presented in this thesis yields higher quality than conventional samples grown in the group. Linewidths of the improved method approach the homogeneous linewidth limit [291] and display lower linewidths of grown (2.4 meV [286]) and exfoliated (1.1 meV [291]) samples than previously reported. The column *Voigt Ratio* lists the ratio between homogeneous and inhomogeneous broadening (function 3.3) of the spectrum with minimal FWHM with the uncertainty taken from the set of data over all spots. A spectrum with a value of 1 represents complete homogeneous broadening.

smaller than previously reported values of 2.4 meV [286] for grown samples and even smaller than previously reported values for exfoliated samples with FWHM down to 1.1 meV [291]. Slight doping of the sample is evident through the signal of the charged trion (T) at 1.611 meV [292, 293]. Subfigure b tables those samples produced from CVD grown $MoSe_2$ for which statistics was recorded, where the top four samples were grown with the improved method described in this thesis and the bottom four were grown by colleagues using an alternative method. The second column keeps track of all the top (t) and bottom (b) hBN thicknesses of the encapsulation. If possible, a mean (*Mean*) in FWHM was calculated averaging over an extended area including all *Spots* of the sample with a diffraction limited excitation spot size ω_0. The total area scanned is then the number of spots times ω_0^2. The column *Std* lists the standard deviation from the set of data and corresponds to the standard deviation value taken from the fit. For a single spectrum this corresponds to the uncertainty of the fit. The column *Voigt Ratio* lists the fit parameter f from function 3.3 and represents the ratio between Lorentzian and Gaussian function corresponding to homogeneous and inhomogeneous broadening, respectively. A value of one corresponds to a complete homogeneously broadened spectrum proportional to the population relaxation decay rate of the excitonic state and the dephasing rate between the coherent superposition of the ground and excited states [211]. A value closer to zero takes inhomogeneous broadening effects into account such as lattice defects and impurities. The uncertainty of this value also stems from the standard deviation across the entire set of data or from the single spectrum fit where only one spectrum was recorded.

Importantly, within the monolayer area, not all optical spots are included. The number of spots was determined by considering only those where the PL peak intensity was reduced $\leq 30\%$ of the maximum peak. The reason being that spots with further decreased PL intensity often belong to spots of diminished quality by external factors such as defects and residues from the fabrication process forming *bubbles* below the hBN. On spots with deteriorated quality through residues, the fit of a single linewidth is often prevented.

Comparing the average values as well as the minimum value of FWHM in PL over all samples indicates that the improved method of sample growth and quality monitoring presented in this thesis yields higher quality samples than conventional samples grown in the group. Furthermore, linewidths of the improved method display smaller values of FWHM of grown and exfoliated samples than previously reported [286, 291].

For completion, the data from differential reflection (DR) is presented in Fig. 4.11. Data from an additional sample (JS3, hBN thickness of 90 nm for top and bottom)

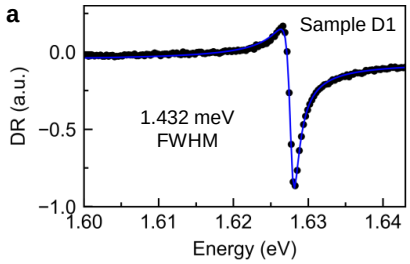

b

Sample	Spots (µm²)	Mean (meV)	Std (meV)	Min (meV)
D1	847	2.1	0.4	1.4
JS1	1394	4.6	1.0	3.1
JS2	6333	2.8	0.8	1.8
JS3	25	3.6	0.9	2.6

Figure 4.11: Optical linewidths in differential reflection spectroscopy of encapsulated $MoSe_2$ at T=4K. **a**, Best result from sample D1 with a FWHM of $1.432 pm 0.016$ meV according to the fit of a Fano line shape. **b**, Tabled data from samples grown with the method presented in this thesis. Sample *JS3* is added while for sample *J1* DR data was unavailable.

was included while from the J1 sample, DR data do not exist. Due to a lack of data, a comparison to other samples within the group was not possible. All samples tabled where grown by the improved method presented in this thesis. The signal is extracted in accordance with equation Eq. (3.4) and fitted using the Fano line shape (equation 3.5). Similar to PL, a criterion was implemented to eliminate spots stemming from fabrication induced distortions. Included *Spots* where those with a DR signal difference ≤ 70% of the minimum peak.

4.3.2 Tungsten-based growth

For tungsten based growth, precursor tungsten(IV)oxide powder (WO_2, ≥ 99.9%, 100 mesh, Sigma-Aldrich) was used together with the above named precursors of chalcogenides. Only WSe_2 has been grown here. WS_2, which is used in some of the fabricated heterobilayer samples later discussed, was grown by colleagues with similar precursors using the growth method displayed in Fig. 4.4a. For the growth here, an additional quartz tube, about 20 cm long with a 10 mm diameter, was inserted into the large tube of the furnace with the tungsten precursor powder placed directly inside this second tube. This is to keep the tungsten concentration high between the evaporation and the growth chamber (chamber 3). The substrates were placed inside a boat (empty of precursors) directly at the exit of this smaller tube. The setup and temperature profile are displayed in Fig. 4.12 a and b. For the growth, n_{WO_2} = 80mg and n_{Se} = 150mg were used with T_g = 960°C as well as ΔT_g = 50°C/min below and ΔT_g = 5°C/min above 860°C of the growth chamber. For tungsten, a T_W = 1100°C had been introduced with ΔT_W = 50°C/min whereas selenium was kept at the parameters from molybdenum growths: T_{Se} = 390°C with ΔT_{Se} = 16.7°C/min starting at T_g > 860°C, at which point the

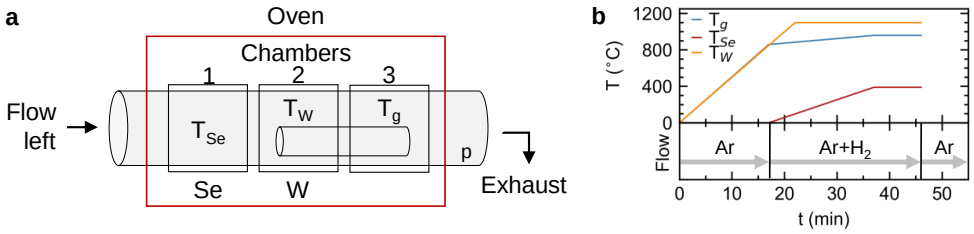

Figure 4.12: Tungsten based monolayer growth operation for WSe_2. **a**, The setup includes an additional quartz tube of 20 cm in length and 10 mm in diameter between chambers 2 and 3 to increase tungsten concentration in the growth region. **b**, Temperature and flow profile.

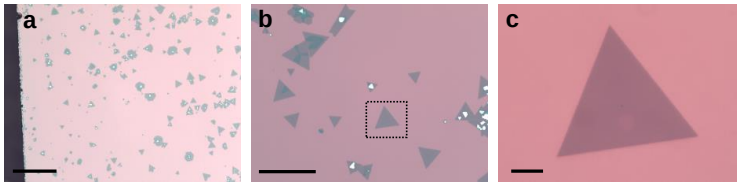

Figure 4.13: Growth result of WSe_2. **a**, Distribution of different shapes and sizes, well-separated. **b**, Well-separated triangular crystals of high quality. **c**, Dotted square in **b**. Scale bars are (left to right): 300, 100, and 10 μm.

selenium chamber had been heating up to 56°C due to cross-heating of the chambers. Other parameters were $t_g = 10$min and for the flow $q_{Ar} = 300$sccm and $q_{H_2} = 0.75$sccm at $T_g > 860$°C had been chosen. The result of large, homogeneous, and well-separated monolayers is displayed in Fig. 4.13.

4.3.3 Deterministic growth

The results of this section, though preliminary, highlight a significant challenge in achieving deterministic growth of TMD crystals at designated sites on a SiO_2/Si wafer. This capability might be critical for integrating TMD monolayers into current semiconductor manufacturing processes. Achieving monocrystalline TMD growth across an entire wafer presents a formidable challenge due to the need for a precise and uniform initiation of the growth process. First, an effective seeding mechanism must be engineered to nucleate the monolayer. The subsequent growth would need to strictly follow a Frank–Van der Merwe mode to maintain layer-by-layer deposition, minimizing defects to preserve monocrystallinity. While growing monocrystalline TMDs across the entire wafer is difficult, deterministic growth offers a simplified approach. By developing precise seeding at predetermined locations, TMD monolayers can be selectively grown where needed, followed by the removal of excess material through etching or

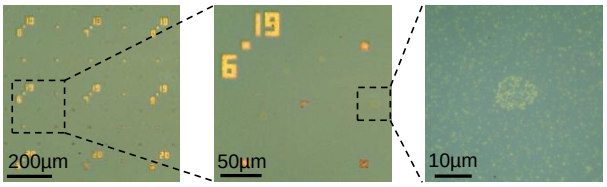

Figure 4.14: Deterministic TMD growth on a patterned SiO_2/Si substrate. Equilateral triangles had been written during e-beam lithography and etched using a wet-etch process. The 5 nm deep pits had edge lengths of 15 to 150 nm in the lithography design. On sites with such pits, more deposition or growth is induced during MoS_2 growth. Due to the poor growth quality overall, it is difficult to say how the growth was induced and if the orientation of the triangles had an impact on the crystal's orientation.

alternative methods. This approach reduces the complexity of the task to solving the seeding challenge.

In the approach presented here, triangular-shaped holes were patterned into the substrate to locally alter the precursor partial pressures and potentially induce swirls of the flow. Equilateral triangles of various sizes were etched into the SiO_2/Si substrate using e-beam lithography and a wet-etching process, producing holes of 5 nm in depth. The substrates where then loaded into boats, following the growth methodology of Section 4.3.1 for MoS_2 growth. The triangle side lengths, ranging from 15 to 150 nm, did not appear to significantly affect the outcome. However, due to the growth being far from equilibrium, only small, deposition-like islands were formed. Although the seeds influenced the local growth environment, leading to enhanced deposition in their vicinity, the poor crystal quality makes it unclear whether the triangular shape directly affected the crystal orientation.

This method has the potential to engineer specific surface features that modify the flow profile over the substrate, inducing favorable changes in precursor concentration. Previous work, independent of this study, has demonstrated that etched holes can indeed act as growth seeds for micrometer-scale monolayers [294]. Other approaches used deposition techniques to deposit molybdenum precursor as seeds with which the chalcogen precursor reacts during the growth step [295]. Additionally, patterning gold particles on SiO_2 substrates has shown promise in promoting TMD growth as well [296].

Chapter 5

Mono- and Bilayer growth variations

5.1 Bilayer and heterobilayer growth

As discussed in Section 4.1, the growth of homobilayers can be induced by altering the chemical potential to enter into the Stranski-Krastanov growth mode, see Fig. 4.1. The result in Fig. 5.1 was achieved by starting from the monolayer growth as specified above (Section 4.3.1) and consecutively increasing selenium concentration (n_{Se}) from 100 to 150 mg while decreasing molybdenum concentration (n_{MoO_2}) from 50 to 40 mg, as indicated in the figure. The results are well separated bilayer crystals which can clearly be identified from the optical contrast under the microscope. The overall size of the crystals is smaller since monolayer growth diminishes to give rise to bilayer growth. It is worth noting the uniformity of bilayer growth as compared to mixtures of mono-, bi-, tri-, and multilayer growths [297, 298].

5.1.1 Vertical heterobilayers

Due to the lattice mismatch of ~4% in the molybdenum-based $MoSe_2/MoS_2$ system, simply changing the chemical potential to induce second layer growth does not suffice [299], at least not without introduction of additional chemicals [106]. Instead, higher temperatures were employed to induce nucleation of the second layer on top of the first. A similar reasoning had been found for homobilayers to grow in different stacking configurations [300].

TMD monolayers are quite sensitive when it comes to sequential heat treatment. Re-heating a crystal after cool-down to high temperatures can cause various sorts of destructions, see Fig. 5.2. Initial attempts to raise the temperature of the growth of the second layer resulted in severe damage to the crystal (Fig. 5.2 a), sometimes destructing

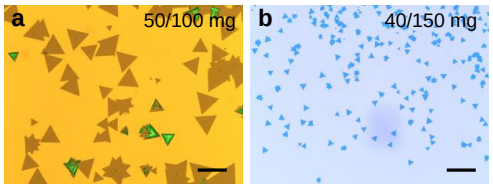

Figure 5.1: The bilayer growth result. **a**, Growth of monolayer $MoSe_2$ as specified in Section 4.3.1. **b**, Decreasing the molybdenum concentration (the powder amount n_{MoO_2}) from 50 to 40 mg and increasing the selenium concentration (the selenium amount n_{Se}) from 100 to 150 mg, as indicated, will change the growth mode and yield smaller but well separated bilayer crystals. The scale bar is 200μm.

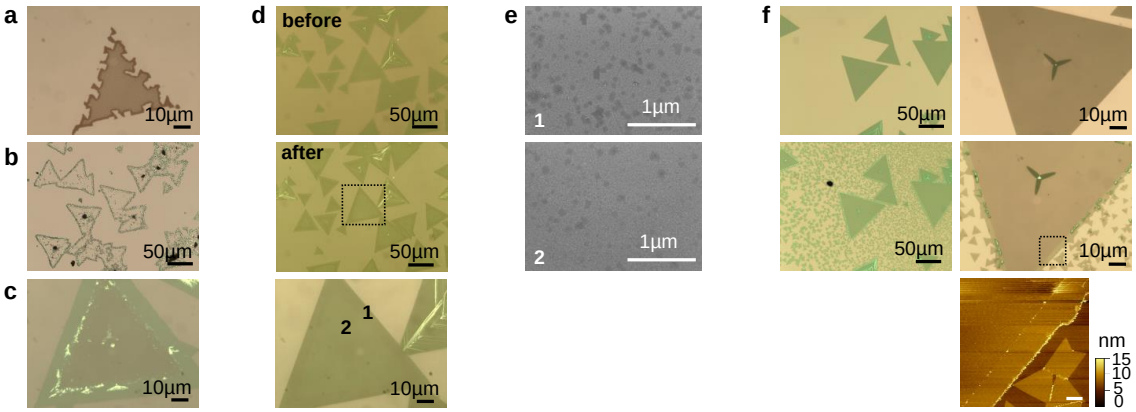

Figure 5.2: Outcome and damage during separated heterobilayer growth in optical imaging, SEM (**e**), and AFM (**f**, bottom). Re-heating of the first layer can cause severe damage (**a**) or entire destruction (**b**). Failed vertical growth can be seen through separated multilayer growth (**c**) or formation of undesired nucleation sites (**d**, **e**). Only lateral growth could be induced (**f**) with residue particles on the hetero edge as well as on the outside edge (see AFM, bottom image).

the crystal entirely (Fig. 5.2 b) or cause uncontrolled and undesired nucleation site on the first layer (Fig. 5.2 c and d). Scanning electron microscopy could reveal the nucleation sites of about 100 nm in lateral dimension at 42.000x magnification, 10 kV beam energy, and 3 mm aperture. Second layer growth, without destroying the first layer, could only be achieved laterally, as is displayed in Fig. 5.2f and discussed in Section 5.1.2 below.

To enable vertical heterobilayer growth, a new growth method was established to grow the second layer immediately after the first, not needing to cool down to room temperatures, and exploiting the out-of-equilibrium conditions of the first layer growth. Through precise control of the intermediate ramp-up in temperature, the flow, and the precursor concentrations, vertical heterobilayer growth was achieved.

Figure 5.3 displays the growth setup with according temperature and flow profiles

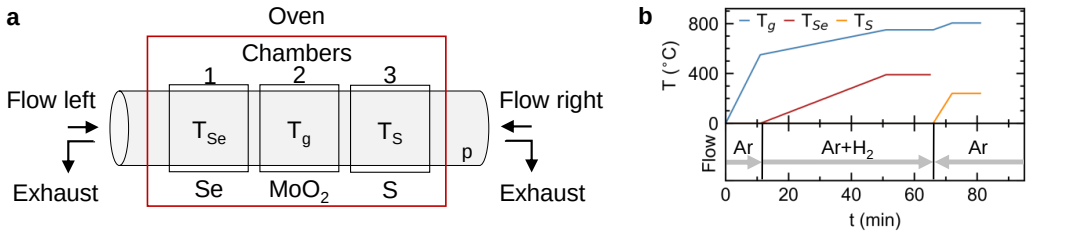

Figure 5.3: **a**, Adjusted setup allows for bidirectional flow and change in chalcogen precursor through corresponding precursor placement. **b**, Temperature and flow profile of the process.

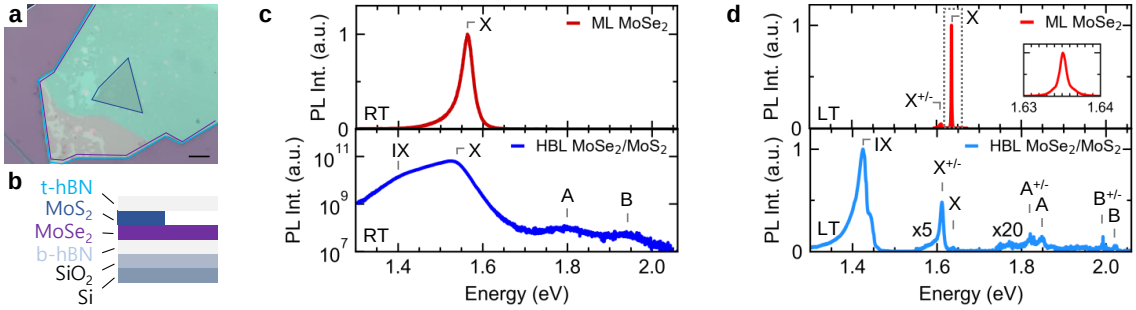

Figure 5.4: Grown $MoSe_2/MoS_2$ heterobilayer encapsulated in hexagonal boron nitride (hBN). **a**, Optical image of the encapsulated sample. **b**, Side view illustration. **c**, Photoluminescence spectroscopy of the monolayer (top) and heterobilayer (bottom) regions at room temperature. **d**, Photoluminescence spectroscopy of the monolayer (top) and heterobilayer (bottom) regions at cryogenic temperatures (*LT*). The scale bar in **a** is 10 μm.

which allows for immediate growth of one hetero-layer after the initial layer by changing the carrier gas flow direction and with it the chalcogen precursor within the growth regime. Selenium (n_{Se} = 100 mg) is hereby placed to the left of the growth chamber as in previous growths with n_{MoO_2} = 20 mg and a similar temperature and flow profile as before. After the selenium growth time, the flow is changed to the right side with $Q = q_{Ar}$ = 200 sccm and sulfur precursor (n_S = 80 mg) is heated from 150°C (due to cross heating of the chamber) to its final temperature T_S = 240°C, now located upstream from the growth chamber, within t^{gap} = 5 min. Growth times of t_g^{Se} = 15 min and t_g^S = 10 min were determined with corresponding growth temperatures T_g^{Se} = 750°C and T_g^S = 850°C.

One of the few well-grown heterobilayers was picked-up and encapsulated by hBN with top and bottom hBN thicknesses of 70 nm and 280 nm, respectively. The sample is displayed in Fig. 5.4a and b. Room-temperature (*RT*) photoluminescence spectroscopy with excitation wavelength of 532 nm, at 170 μW excitation power with 10 s integration, reveals clear signal from the $MoSe_2$ monolayer site at 1561.69 ± 0.05 meV with a FWHM

of 34.3 ± 0.2 meV, see Fig. 5.4 c top. A monolayer MoS_2 signal is not available, since this layer has grown strictly on top of the $MoSe_2$. Deviation in the peak position of MoS_2 A- and B-excitons (*A* and *B*, respectively) from exfoliated samples both at room [62, 301, 302] and cryogenic temperatures [303] can be explained by potential chalcogen alloying in the MoS_2 sample which would shift the energy downwards, see Section 5.2.

On the heterostructure at room temperature, the underlying states can be identified by plotting on a log scale ([302]). The spectrum, taken at 400 μW excitation power with 240 s integration, reveals a spectroscopic pump around 1.40 eV ascribed to the interlayer exciton states (*IX*) [302], as well as the two pumps at 1.79 eV and 1.95 eV indicating the A- and B- exciton states of MoS_2 with a splitting of roughly 160 meV [62, 301, 302], see Fig. 5.4 c bottom. The A exciton of $MoSe_2$ (*X*) appears shifted from its pure monolayer position by roughly 30 meV. This might not be a shift, but simply a stronger contribution from the charged exciton at lower energy (see discussion below) indicating a higher natural doping in the heterobilayer region, potentially through additional defects in the neighboring MoS_2 layer.

At low, i.e. cryogenic, temperature (*LT*, Fig. 5.4 d), the peaks become narrow and well-defined [210]. The narrow monolayer PL signal (taken at 100 μW power with 5 s integration) at 1635.1336 ± 0.0016 meV with a FWHM of 1.062±0.007 meV, was plotted before as sample *J1* in Section 4.3.1. The heterobilayer sample displays multiple peaks with state population cascading down to highest intensity peak at 1424 meV, denoted as the interlayer exciton peak [302]. To resolve all peaks, the measurement was done at 100 μW excitation power with an integration time of 200 min. The A- and B-exciton of MoS_2 at around 1847 meV and 2022 meV, respectively display an equally strong trion signature ($A^{+/-}$ and $B^{+/-}$) at roughly 30 meV below the uncharged signature, in accordance with previous studies [301]. The same holds for the neutral (*X*) and charged ($X^{+/-}$) excitons of $MoSe_2$ [292] where the $X^{+/-}$ signal is much stronger than the signal from the neutral exciton. The latter, together with the fact that the direct exciton peak is exactly at the same position in mono- and heterobilayer, is again indicative of the intrinsic doping in the heterobilayer region as speculated above for the room-temperature measurement.

It can be noted, that the charged trion is probably a negative creature due to results found in charge-controlled devices, where the neutral samples display a slight negative doping ([P3], [P5], [P6] and [P10]), as well as from the large splitting which has been attributed to the negative trion in WSe_2 [304]. On another note, no splitting of the *X* and $X^{+/-}$ peak are observed, in contrast to a previous study on an exfoliated and stacked $MoSe_2/MoS_2$ sample, where the splitting had been assigned to the influence of any

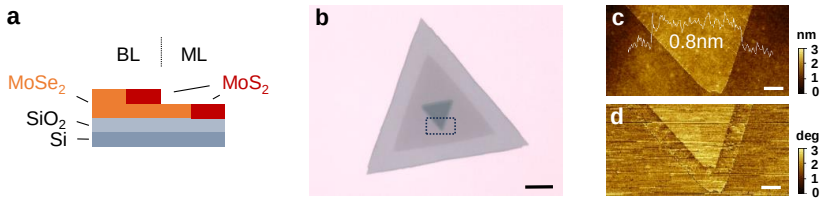

Figure 5.5: Bilayer to heterobilayer transition in the laterally stacked $MoSe_2/MoS_2$ system. **a**, Sketch of the sample. **b**, Optical image displaying four distinct regions. **c**, AFM height measurement of the dotted region in Subfigure b, displaying two distinct regions: the monolayer and the bilayer/heterobilayer region. **d**, AFM phase resolving the two bilayer regions with $MoSe_2$ and MoS_2 on the inside and outside, respectively. The scalebars are 20 μm and 2 μm for Subfigures b and c/d, respectively.

moiré lattice present in the system [140].

Due to low yield and immense difficulties to keep the growth conditions stable for vertically stacked heterobilayers, another method to achieve such systems was found. This method uses a grown homobilayer as the seed for the heterobilayer, see Fig. 5.5 a. In the end, the hetero-layer attaches to to the homo-layer on top of an initial layer, in this case $MoSe_2$.

Figure 5.5 displays such a sample with the bilayer and monolayer regions scetched in Subfigure a. Subfigure b displays a typical growth result which displays four distinct regions of optical contrast which can be assigned to the corresponding layers in Subfigure a. The dotted region is the scan region for the AFM measurement in Subfigure c and d. The height profile (c) displays the step from the monolayer to the bilayer, with 0.8 nm slightly higher than the 0.6 nm that one would expect. However, the height is constant within the fluctuations across the entire corner, whereas the phase of the AFM tip (Subfigure d) changes clearly for the hetero-bilayer region. Unfortunately, this sample was destroyed during the pick-up with hexagonal boron nitride preventing further studies in optical microscopy.

5.1.2 Lateral heterobilayers

Heterobilayers not only occur in vertical stacking arrangement. If two hetero-layers attach in-plane, they form a lateral heterobilayer which, due to the strong covalent binding from atom to atom, can ideally be manufactured in edge-epitaxy [181].

Figure 5.6 displays a typical sample. The optical image after growth shows a clear contrast difference between inner ($MoSe_2$) and outer (MoS_2) crystal on top of the 285 nm SiO_2/Si substrate. The sample stems from a bidirectional growth process, see Fig.

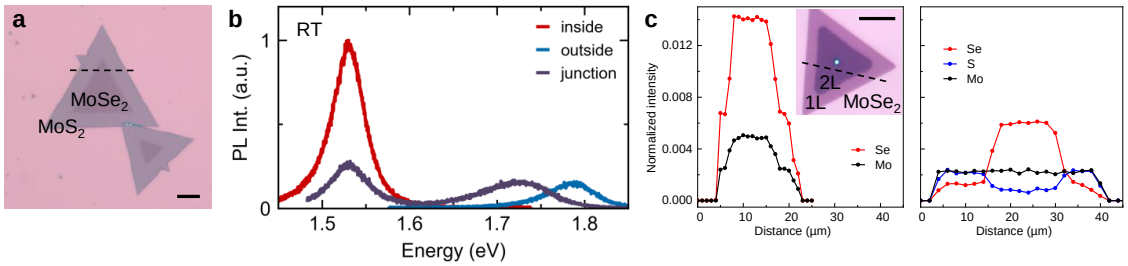

Figure 5.6: Lateral heterobilayer. **a**, Optical image of the as-grown $MoSe_2/MoS_2$ system, displaying clear optical contrast between inside ($MoSe_2$)and outside (MoS_2) regions. **b**, Room-temperature photoluminescence measurement of the inside, outside, and junction region. Peak shifts in the junction region most likely are caused by cross-contamination. **c**, Energy-dispersive X-ray spectroscopy measurement on mono- and bilayer $MoSe_2$ (left), as well as the lateral heterobilayer from Subfigure a (right). The spectrum displays clear signs of cross-contamination and sompositional gradients. The scale bars are 20 μm and 10 μm for Subfigures a and c, respectively.

5.3, with an increased sulfide growth temperature of $T_g^S = 785°C$ (in comparison to $T_g^{Se} = 750°C$) to allow for the sulfur growth on the lattice-mismatched selenium edge of the crystal but decreased temperature from vertical heterobilayer growth ($T_g^S = 850°C$) to prevent vertical formations.

The overall thickness of one monolayer was determined from the optical contrast and from the photoluminescence spectroscopy at room-temperature under 532 nm excitation at 170 μW and 10 s integration, Fig. 5.3b. The inside region displays the $MoSe_2$ photoluminescence of the neutral exciton at 1529.49 ± 0.05 meV with FWHM of 44.61 ± 0.17 meV. The outside region displays the A-exciton peak of MoS_2 at 1783.77 ± 0.12 meV with FWHM of 64.6 ± 0.4 meV. The signal at the junction displays both peaks slightly shifted to the energetic inside. The lower peak is located at 1530.32 ± 0.09 meV and the upper peak at 1721.26 ± 0.20 meV. Both peaks are visible, since both layers are situated inside the optical spot. The energy of both peaks could be shifted due to cross contamination and/or chalcogen alloying during growth. This would shift the exciton peaks of $MoSe_2$ and MoS_2 energetically up and down, respectively, see Section 5.2 below.

Figure 5.6c shows results from energy-dispersive X-ray (EDX) spectroscopy, see Section 3.4. The data was taken at 45° sample twist, 5 kV beam energy, with 2 μm step size, and 35 min integration time by A. Rupp. The figures were adopted from [P9]. Data from a CVD grown mono- and bilayer of $MoSe_2$ (left) are compared with the result from the lateral heterojunction of Subfigure a. It is evident from the spectral intensity that cross-contamination and compositional gradients play a role. The inside region shows less selenium content than the monolayer in the left plot, indicating that se-

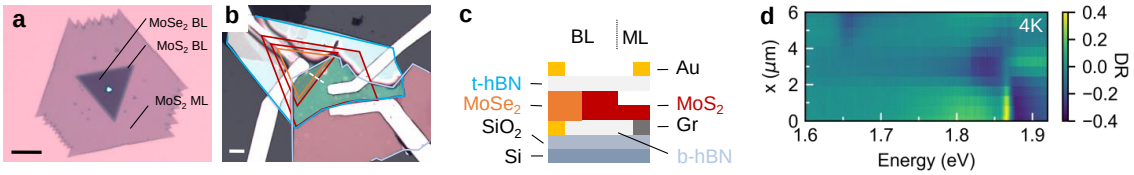

Figure 5.7: Lateral hetero-homobilayer junction. **a**, Optical image as-grown on SiO_2/Si substrate. **b**, Image after device fabrication. **c**, Illustration of the device. The junction is encapsulated in hexagonal boron nitride and contacted with gold (Au) from one side and graphite (Gr) from the other. Top gates made from gold are added on top, while the silicon substrate acts as global bottom gate. **d**, Differential reflection scan along the dashed line indicated in Subfigure **b**. The signal at x= 0 displays a strong resonance at 1875.5 ± 0.4 meV, corresponding to MoS_2 monolayer with an energetic shift due to alloying and cross-contamination. The resonance becomes broad on the small strip of MoS_2 homobilayer and vanishes on the $MoSe_2$ homobilayer where the excitonic resonance is visible at 1654.4 ± 0.5 meV. The scale bars in Subfigures **a** and **b** are 10 μm.

lenium from this region cross-contaminated the outside region during MoS_2 growth, as displayed by the selenium intensity in the outside region. Notably, sulfur seems to have contaminated the inner monolayer region as well, potentially substituting selenium. This indicates that the formation of an alloy is energetically favored over a clean heterostructure junction.

With the lateral heterobilayer growth established, another, more complex architecture can be realized which features a lateral transition of different homobilayers, therefor forming a lateral hetero-homobilayer junction. The sample is displayed in Fig. 5.7, as-grown (Subfigure a) and as electrical device (Subfigure b) with top gates made of gold, contacts from gold and graphite, and the silicon substrate acting as global bottom gate. Each gold deposition involved a 3 nm thick titanium layer for increased binding of the gold layers with 250 nm gold at the bottom (to match the bottom hBN thickness) and 50 nm gold as top gates. Due to a shortcut, the device was never operated to study transport across the hetero-homobilayer junction. Hexagonal boron nitride is used as encapsulation with top- (t-hBN) and bottom- (b-hBN) hBN thicknesses of 80 nm and 253 nm, respectively.

The spectroscopic line scan across the junction in differential reflection spectroscppy (Subfigure d) shows the excitonic signatures of the corresponding regions. On the MoS_2 side ($x = 0$), the spectrum displays a strong feature at 1875.5 ± 0.4 meV, determined through a Fano resonance fit, indicative of the monolayer resonance. The signal on the bilayer ($1 < x < 2$) becomes weak and broad [305], the position is fitted to 1849.5 ± 0.4 meV. The transition to the $MoSe_2$ bilayer ($x > 2$) is marked by the disappearance of this peak and the appearance of the weak $MoSe_2$ transition at 1654.4 ± 0.5 meV.

It can be noted that further away from the junction, the peak from x= 0 shifts energetically upwards to roughly 1900 meV, closer to what would be expected from monolayer MoS_2. This shift is well explainable with alloying and compositional gradients resulting from cross-contamination between selenium and sulfur during the growth, similar to what was observed in optical data and EDX data in the monolayer junction (Fig. 5.6). This effect is further discussed in Section 5.2 below.

5.2 Alloyed transition-metal dichalcogenides: $MoSe_{2(1-x)}S_{2x}$

Following initial signatures of alloyed TMDs in optical spectroscopy and energy-dispersive X-ray spectroscopy (see Section 5.1.2, [P9]), a new growth configuration was developed to give control to the alloy degree. The material system of choice was based on molybdenum as transition-metal and selenide and sulfide as chalcogenides, i.e. $MoSe_{2(1-x)}S_{2x}$, where $x \in [0,1]$ denotes the sulfur content, i.e. the alloy degree. This material combination had been studied in the bulk [306–310] as well as in grown monolayers [311–314]. The specific method introduced here allows for manipulating the alloy degree through a single parameter with monolayer edge sizes up to a magnitude larger than in previous studies.

5.2.1 Growth

Figure 5.8 displays the altered growth setup where now selenium and sulfur are both placed inside their respective chambers. The setup of the boats and substrates stays the same as in previous growths (see Fig. 3.2). Subfigure b plots the temperature profiles of each chamber as put forth by the controllers. It should be noted that the actual temperatures differed from these profiles due to cross-heating between the chambers. Especially the sulfur chamber, due to its overall low temperature, continued to heat up during the constant growth temperature period of up to 25% of its anticipated temperature.

A typical result of growth is shown in Fig. 5.9 with well-separated monolayers grown on the 285 nm SiO_2 substrate that display high homogeneity in high optical contrast imaging, see Section 4.2.3. Lateral sizes of the triangle edges are around 80-100 μm, about a factor of at least 5-10 larger as previous monolayer alloy growths [311–314]. Initial growth parameters where: T_g = 750°C with ΔT_g of 40 °C/min below and 5 °C/min above 650°C of T_g; T_{Se} and T_S set to 390 °C and 135 °C with ΔT_{Se} set to around 17.9

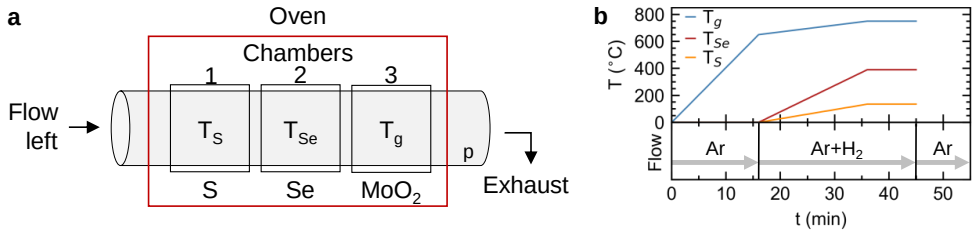

Figure 5.8: CVD growth setup for the growth of $MoSe_{2(1-x)}S_{2x}$ alloys. **a**, Illustration of the growth furnace, all chambers equipped with their respective materials with precursor placement of 40 mg MoO_2, 150 mg selenide, and 100 mg sulfide and 4 substrates placed, all according to Fig. 3.2. **b**, Temperature and flow profile. T_g is set to 750 °C with a δT_g of 40 °C/min below and 5 °C/min above T_g = 650°C. T_{Se} and T_S were initially set to 390 °C and 135 °C with δT_{Se} set to around 17.9 °C/min and δT_{Se} around 5 °C/min according to their respective starting temperatures such that the final temperature would be met coinciding with T_g. Other essential parameters were t_g = 10min and q_{Ar} = 300sccm and q_{H_2} = 0.75sccm with a t_{H_2} = 16min such that hydrogen flow would start at T_g > 650°C and end during cool-down. Notably, due to its overall low temperature the sulfur chamber would heat up in the constant temperature growth regime up to 25% of its set value due to cross heating between the chambers.

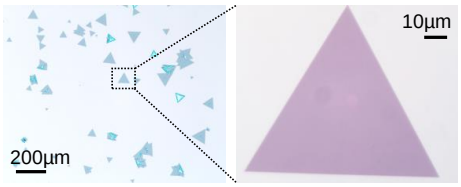

Figure 5.9: Optical images of a typical result of a $MoSe_{2(1-x)}S_{2x}$ alloy. High homogeneity of monolayers displayed in high contrast optical imaging. The dotted square indicates the frame for the image on the right in which a light and a dark circular inhomogeneity stem from the microscopes optics. Typical monolayers display edge lengths of 80-100 μm, a factor of at least 5-10 larger than in previous studies [311–314].

°C/min and ΔT_{Se} around 5 °C/min according to their respective starting temperatures such that the final temperature would be met coinciding with T_g; t_g = 10 min, q_{Ar} = 300 sccm, and q_{H_2} = 0.75 sccm with a t_{H_2} = 16 min such that hydrogen flow would start at T_g > 650°C. The growth of different degrees in alloy was achieved by simply decreasing selenide concentration through T_{Se}, see legend in Fig. 5.10 b.

5.2.2 Optical spectroscopy

The full alloy series, achieved through change of T_{Se}, was measured in photoluminescence (PL) and Raman spectroscopy at room temperature, see Fig. 5.10. The order in which spectra are plotted is changed to reflect the sulfur content as measured below in

EDX spectroscopy, which results in a shuffled order with respect to selenide temperature, as seen in the legend on the right. As expected, selenide concentration decreases with decreasing T_{Se} while T_S stays on the level of monolayer MoS_2 growth. The fact that temperature and sulfur content only roughly coincide is due to several reasons. Firstly, samples were taken from the first to the last substrate in flow direction without accounting for its position. The resulting alloy is then a product of the change in precursor concentration alongside the flow direction. Secondly, it is possible that the large temperature difference between the growth temperature and room temperature causes stress inside the monolayer upon cool-down. Since optical spectroscopy was performed on the growth substrate, this stress might be responsible for any positional signal change. And thirdly, there is the possibility of positional changes in the sulfur content (as is discussed in Section 5.2.5 below). This is due to the fact that the precursor mixture, as anticipated by the temperatures T_{Se} and T_S, is not constant due to a finite temperature slope during growth temperatures. The signal in Fig. 5.10 was taken in the same fashion on all samples, slightly to the side from the center of the crystal (since the center region usually hosts some kind of a growth seed). However, depending on the alloy gradient, the uncertainty in position might be enough to diminish the link between the alloy degree as determined through optical spectroscopy and growth temperature. Furthermore, optical signal from photoluminescence and Raman spectroscopy are taken from the same optical spot. The growths of $x = 0.00$ ($MoSe_2$) and $x = 1.00$ (MoS_2) were performed isolated from each other in their respective tubes using the growth configuration as displayed in Fig. 4.4c. Parameters were hereby the same as listed above, except $t_g = 15$ min was used during MoS_2 growth.

Photoluminescence (PL) spectroscopy at room temperature reveals that the optical band gap can be tuned through the entire range from $MoSe_2$ at 1.523 eV to MoS_2 at 1.824 eV, see Fig. 5.10a. At 1.965 eV the B-exciton is located in the MoS_2 spectrum, 139 meV above the A-exciton at 1.826 eV in accordance with previous reports [315, 316]. PL spectroscopy was performed under 532 nm laser irradiation in a confocal microscope at 160-200 μW with 1-3 s integration. Each spectrum is normalized to the resonance peak. The tunability of the band gap is remarkable from a growth perspective since no other parameters than the selenide concentration were changed, indicating the robustness of the metastable region of supersaturation within the range of given chalcogen concentrations. In contrast to results from physical vapor deposition [312, 313], no general change to the precursor concentrations or the growth setup had to be undertaken.

The result of the Raman spectroscopy in Fig. 5.10b was performed under 532 nm laser

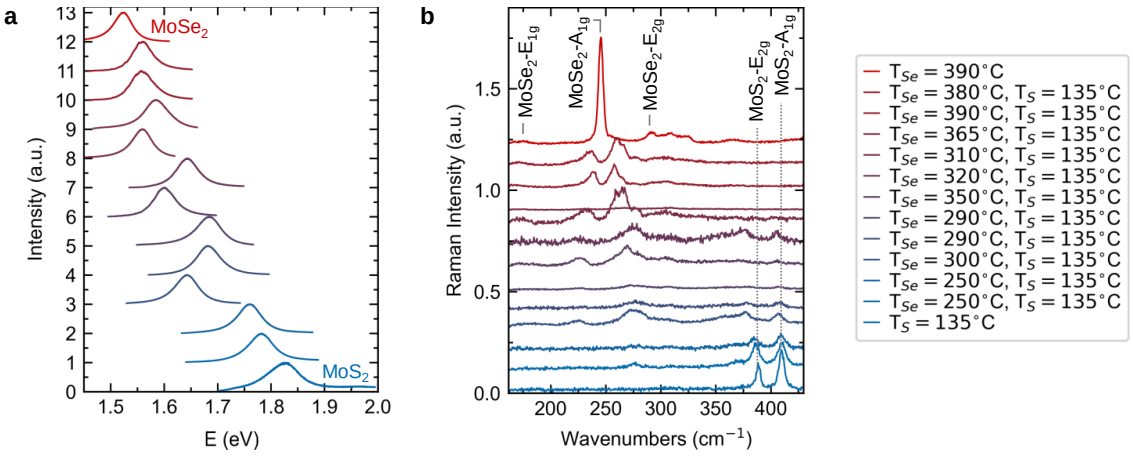

Figure 5.10: Optical spectroscopy at room temperature of as-grown $MoSe_{2(1-x)}S_{2x}$ species. Selenide precursor temperature is used as tuning parameter for the alloy degree, as indicated by the legend on the right. **a**, Photoluminescence spectroscopy revealing full tunability of the band gap from $MoSe_2$ at 1.523 eV to MoS_2 at 1.824 eV. The shoulder at around 1.965 eV corresponds to the B-exciton of MoS_2, 139 meV above the A-exciton at 1.826 eV [315, 316]. **b**, Corresponding Raman spectra. Fundamental optical mode assignment is done in accordance to previous studies [310, 317–321]. MoS_2-A_{1g} and MoS_2-E_{2g} peaks are located at 409.7 cm^{-1} and 388.8 cm^{-1}; $MoSe_2$-E_{1g}, $MoSe_2$-A_{1g}, and $MoSe_2$-E_{2g} at 175.1 cm^{-1}, 245.6 cm^{-1}, and 292.6 cm^{-1}, respectively. The order in which spectra are plotted corresponds to their sulfur content as measured thereafter. Changes in temperature are due to concentration changes alongside the flow direction and corresponding substrate placement, possible local strain in the as-grown monolayer, and positionally graded alloy degree as discussed in Section 5.2.5.

light irradiation in a confocal microscope at room temperature with 160-200 μW at 10 min integration time. Fundamental optical modes are assigned in accordance with historical studies [310, 317–321]. MoS_2 displays two prominent peaks at 409.7 cm^{-1} and 388.8 cm^{-1} which are identified as A_{1g} and E_{2g}, respectively. $MoSe_2$ displays several peaks which are assigned as E_{1g} at 175.1 cm^{-1}, A_{1g} at 245.6 cm^{-1}, and E_{2g} at 292.6 cm^{-1}. Exchanging selenide for sulfide and vice versa will inevitably lead to energetic shifts and mode mixing. It can be shown that any energy shift, as well as the prominent splitting of the $MoSe_2$-A_{1g} peak, with the alloy degree originates from the two different masses of chalcogen atoms as well as the difference in binding to the molybdenum atom [310]. The data shown here agree well with previous results for bulk [310] and for monolayers [311–313].

5.2.3 Determination of the alloy degree through energy-dispersive X-ray spectroscopy

The transition function of the band gap in the $MoSe_{2(1-x)}S_{2x}$ alloy system with regard to the sulfur content x, i.e. the alloy degree, had been indicated to be a linear relation through density functional theory calculations by Komsa and Krasheninnkov [322] and measured using X-ray photoelectron spectroscopy by Feng et al. [313]. In this study, we used energy-dispersive X-ray spectroscopy (EDX) to determine the composition at $1000x$ magnification, 5 keV electron energy, 7.5 mm detector to sample distance, 30μm aperture, 75° sample tilt-angle, and 30 min integration time (see Chapter 3.4). For each sample, optical spectroscopy was performed prior to EDX measurements due to electron induced defects and carbon deposition during electron irradiation. As evident from Fig. 3.11, the atomic resonance of L_3M_{45} in selenide at 1.379 keV is an ideal candidate to sample the composition due to its isolation from other resonances. Figure 5.11a illustrates the measurement and consecutive comparison. With the signals from monolayer $MoSe_2$ and MoS_2 as reference, the degree in alloy is determined through

$$x = 1 - \frac{\sum_E [I_{MoSeS}(E) - I_{MoS}(E)]}{\sum_E [I_{MoSe}(E) - I_{MoS}(E)]}, \tag{5.1}$$

where $I_{MoSeS}(E)$, $I_{MoSe}(E)$, and $I_{MoS}(E)$ denote the intensity values of the alloy, of molybdenum diselenide, and of molybdenum disulfide at energy value E, respectively. The position of the resonance in photoluminescence was determined through a pseudo Voigt fit (see Chapter 3.3). The resulting data, as well as a linear fit through the data points, is plotted in Fig. 5.11b. It can be noted that the slope of the acquired fit of 282 ± 30 meV is just about equal within error bars of the result of 312 meV acquired by Komsa and Krasheninnkov (read off from the figure in [322]) and slightly below of 326 meV acquired by Feng et al. [313]. The y-intercept of the fit yields 1493 ± 19 meV.

5.2.4 Heterobilayer of $WS_2/MoSe_{2(1-x)}S_{2x}$

With the possibility of tuning the direct energy band gap at the K valley in a TMD monolayer through the alloy degree, the possibility to tune the energy band across two or more materials into resonance becomes feasible. In the heterostructure of $WS_2/MoSe_{2(1-x)}S_{2x}$, band alignment calculations point to the fact that the valence band could be tuned into resonance under a linear energy shift between $MoSe_2$ and MoS_2 [116]. Similar results concerning the band alignment in this system were experimentally measured in microARPES experiments where the electronic structure

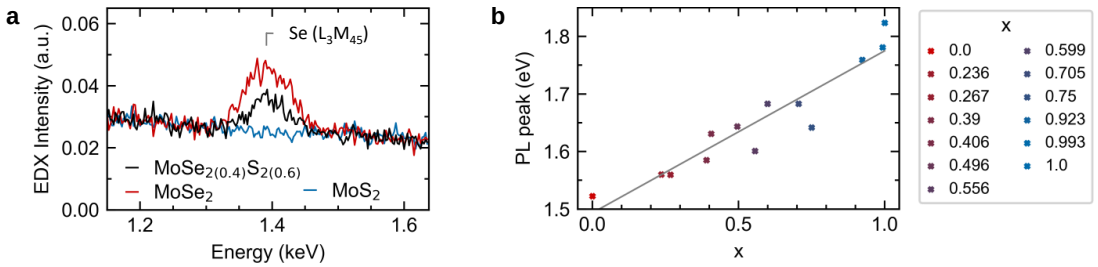

Figure 5.11: Alloy determination through EDX spectroscopy. **a**, Determination through referencing the selenide L_3M_{45} line of monolayer $MoSe_2$ and MoS_2 to the alloy. **b**, Result for all alloy samples with the PL peak position taken from the spectra plotted in Fig. 5.10. Grey line indicates the linear fit through all data points with a slope of 282 ± 30 meV and y-intercept of 1493 ± 19 meV.

in k-space is sampled through high spacial and angular resolution of photoemitted electrons from the sample under X-ray irradiation. By calibrating the Fermi level to that of graphene, the alignment between different TMDs was determined making an energy values comparison of the valence band edges in $MoSe_2$, MoS_2, and WS_2 possible [117]. Applying a linear model to the energetic transition yields band-alignment at an alloy degree of roughly 44%.

Fabrication

To this end, three samples with different alloy degrees were grown and fabricated into functional devices, see Fig. 5.12. The alloy degree was determined through photoluminescence spectroscopy at room temperature under 532 nm laser light irradiation in confocal microscopy with 110-150 μW power and 30 s integration time, prior to encapsulation in hexagonal boron nitride (hBN). The hBN thicknesses for top (t-) and bottom (b-) hBN were 48 and 74 nm for Sample 1, 58 and 73 nm for Sample 2, and 69 and 39 nm for Sample 3. Each sample was contacted through a thin film of graphite initially, however, during fabrication the graphite film in sample 3 was lost through folding of the material flake. Contact to sample 3 was later established through a gold contact by etching through the top hBN and evaporating titanium (3 nm) and gold (160 nm) into the created pit, see Fig. 5.12e and Section 3.2.4. Due to non-constant etching rates of the system through hBN, in total four etching runs needed to be performed with an AFM measurement in between runs to measure the current etch rate. The total etch depth was 110 nm.

Contacting of the graphite flakes sticking out on the side of the hBN/TMD/hBN stack was achieved via titanium (3 nm) and gold (80 nm) evaporation using the lithography

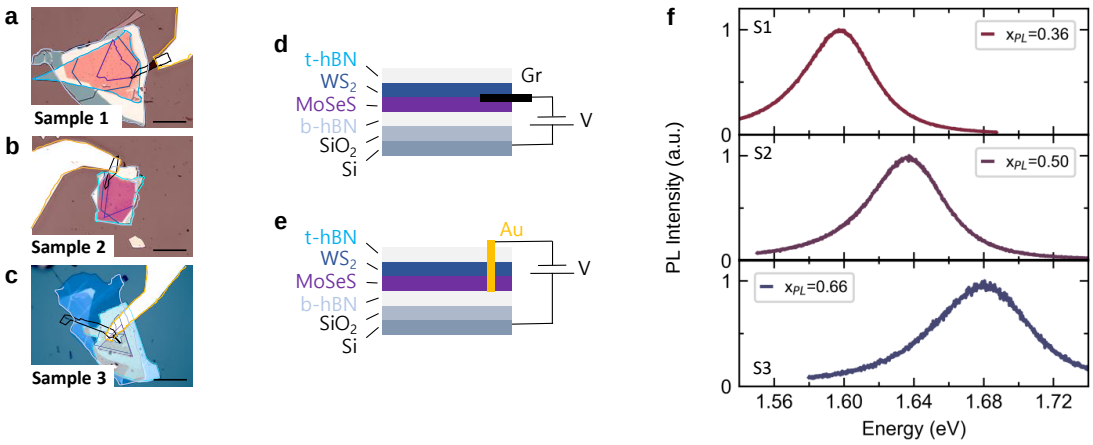

Figure 5.12: Heterobilayer samples utilizing three different alloys. **a, b, c**, Optical images of *Sample 1*, *Sample 2*, and *Sample 3*, respectively, after encapsulation in hBN and contacting by either graphite (black, samples 1 and 2) or by gold (yellow, sample 3). The scale bar is 50 μm. Multiple laser lithography steps were undertaken to create the gold contact in sample 3 via etching into the top hBN layer after encapsulation, see Section 3.2.4. All fabrication was undertaken on a single 5x5 mm Si/SiO_2 with 50 nm oxide thickness. **d, e**, Device schematics of contacted and back-gated samples. **f**, Photoluminescence spectra at room temperature prior to encapsulation alloy for the assignment of the alloy degree, x_{PL}, according to the linear function acquired through EDX correlation, in Fig. 5.11.

steps described above. The fabrication of all three samples was performed on a single 5x5 mm Si/SiO_2 substrate with a 50 nm oxide thickness.

Back-gating the samples was achieved through contacting the silicon underneath the silicon dioxide, see Fig. 5.12d and e. To avoid Schottky barriers between the metal cables and the semiconducting silicon, gold was inserted into the silicon by electrical discharge through two silicon corners of the substrate under high voltage of 20-30 V application between two gold wires which are brought into close proximity to each other on either side of a silicon corner [323]. The corners are then contacted in the same way as the gold bonding pads on top of the substrate via thin metal wires and silver paste.

The degree in alloy was determined solely through photolumenescence at room temperature prior to encapsulation instead of EDX spectroscopy to avoid any damage and contamination of the samples by the electron beam or carbon deposition inside the SEM chamber. The corresponding alloy degree x_{PL} (see Fig. 5.12f) was determined in accordance with the linear fit acquired from previous data (Fig. 5.11).

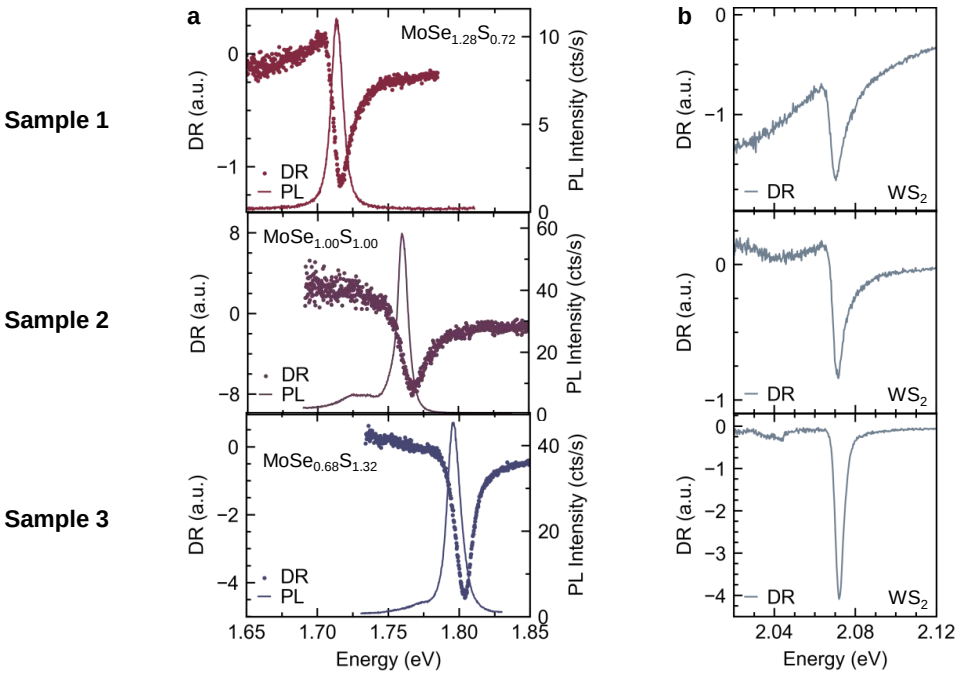

Figure 5.13: Encapsulated monolayer DR and PL at cryogenic temperatures (4K) of the alloy, **a**, and DR signal within the same device of monolayer WS_2, **b**. PL and DR signals in the alloy monolayers lie directly on top of each other on the sample optical spot, a hallmark of the exciton resonance. With respect to the respective WS_2 DR peak, the alloy signals shift according to their alloy degree with a slope of 275 ± 11 meV, in accordance to room temperature measurements. The PL peak positions are 1713.798 ± 0.007 meV, 1760.04 ± 0.04 meV, and 1796.153 ± 0.015 meV with FWHMs of 9.923 ± 0.024 meV, 8.75 ± 0.14 meV, and 11.10 ± 0.06 meV for samples 1 (top), 2 (middle), and 3 (bottom), respectively.

Optical spectroscopy

Initial optical results at low temperatures of T= 4K and with shorted contacts revolved around the monolayers of the heterostructure. With respect to the WS_2 monolayer signal in DR (see Fig. 5.13b) at roughly 2.072 meV, each alloy monolayer has a shifted PL and DR signal, as expected. Similar to room temperature, the excitonic resonance shifts with a slope of 275 ± 11 meV fitted through the three data points available. Some PL spectra display a broader shoulder, in particular samples 2 and 3, on the low-energy side which is not visible in the DR spectrum. These shoulders can correspond to defects in the alloy lattice system. The PL peak positions are 1713.798 ± 0.007 meV, 1760.04 ± 0.04 meV, and 1796.153 ± 0.015 meV with FWHMs of 9.923 ± 0.024 meV, 8.75 ± 0.14 meV, and 11.10 ± 0.06 meV for samples 1, 2, and 3, respectively. All data is acquired through a Fano fit (see Section 3.3).

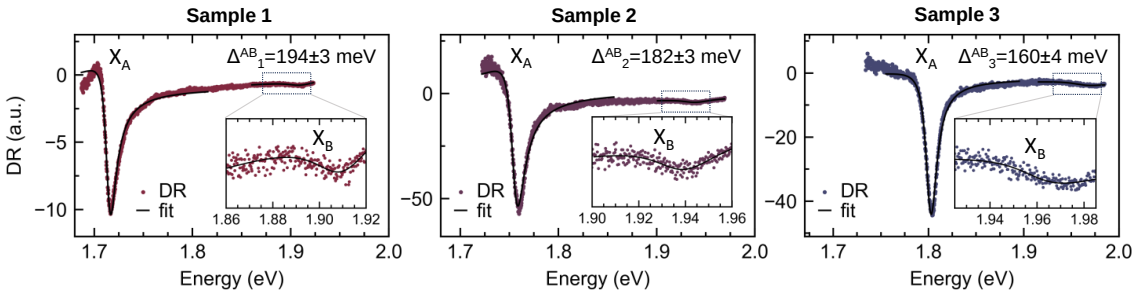

Figure 5.14: Tracking of the B-exciton shift with the alloy degree. The energy difference Δ^{AB} between the A (X_A) and the B (X_B) resonances decrease for increasing alloy degree, as indicated. The resonances are fitted separately in the corresponding energy range using a Voigt fit (see Section 3.3). Positions of the B-exciton are 1909.00 ± 0.07 meV, 1937.84 ± 0.09 meV, and 1961.89 ± 0.05 meV for samples 1, 2, and 3, respectively.

The DR signal also allows for tracking the shift of the B-exciton peak at higher energies, as depicted in Fig. 5.14. Sometimes barely within the reange of the spectrometer, the data allows for a Voigt fit (see Section 3.3) seperately for the A-exciton (X_A) and B-exciton transition (X_B). The resulting peak distance between X_A and X_B for samples 1, 2, and 3 are $\Delta_1^{AB} = 193 \pm 3$meV, $\Delta_2^{AB} = 182 \pm 3$meV, and $\Delta_3^{AB} = 160 \pm 4$, with B-exciton positions of 1909.00 ± 0.07 meV, 1937.84 ± 0.09 meV, and 1961.89 ± 0.05 meV. The resulting linear shift in B-exciton transition amounts to 174 ± 12 meV, different from the 242 meV acquired by Komsa and Krasheninnkov [322] as well as 323 meV acquired by Feng et al. [313]. The difference can be due to different dielectric environments of the excitonis system in all studies as well as different intrinsic and extrinsic electrostatic doping between the experimental studies.

5.2.5 Alloy gradients

After establishing a controlled method to grow alloy TMDs from $MoSe_2$ and MoS_2, the effect of laterally graded alloy crystals shall be discussed again, as it is evident from the optical results in Section 5.1 in combination with their EDX results, that such a distribution is formed during the growth process.

The results here are very limited and concentrate on the optical results in Fig. 5.15. A shift in the exciton line peak in the photoluminescence spectrum can be caused by strain in the crystal stemming from the cool-down procedure from the growth temperature to room temperature. High strain in the inside of the crystal would then shift the excitonic resonance to lower energies [324–329]. To neutralize this effect, the grown alloy picked up and encapsulated via hexagonal boron nitride (hBN). Interestingly, after

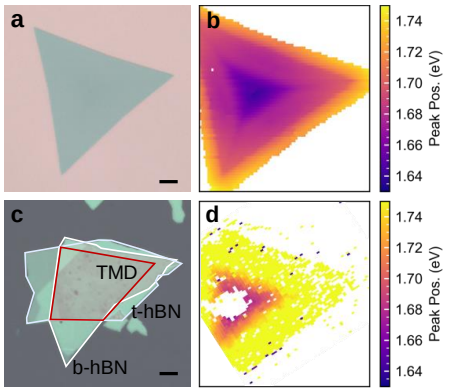

Figure 5.15: Optical spectroscopy of a positionally graded alloy of $MoSe_{2(1-x)}S_{2x}$. **a**, Optical microscopy image of the as grown crystal. **b**, Two-dimensional convocal microscopy scan with the atomic resonance fitted to the photoluminescence spectrum. **c**, The same crystal encapsulated in hexagonal boron nitride. **d**, Equivalent measurement as in **b**. The scale bar is 10 μm.

encapsulation the entire signal is shifted to higher energies, Fig. 5.15d. Both measurements in Subfigures b and d where taken under 532 nm illumination at 150 μW with a 2 s integration per pixel. Notably, the exciton peak is still shifted to lower energies towards the inside of the crystal, supporting the idea of the presents of alloy gradients in the system.

Energy-dispersive X-ray (EDX) spectroscopy measurements were taken on similar crystals, however, they where not able to resolve the change in chalcogen concentration. Only single point measurements were taken that indicated a gradient from the inside to the outside of the crystal. A clear link between the shift in PL energy and concentration, therefor, remains missing.

Chapter 6

Summary and outlook

This thesis presents a framework for growing high optical quality monolayer transition-metal dichalcogenides (TMDs). Monolayers of MoS_2, $MoSe_2$, $MoTe_2$, and WSe_2 were successfully grown. Most experiments and statistics focused on $MoSe_2$ where full-width at half maxima (FWHM) down to 1.06 meV could be demonstrated, much smaller than previously reported values of 2.4 meV [286]. Samples of WS_2, used in fabricated heterostructures, were grown by colleagues using the same growth setup with methodological variations. Additionally, the direct growth of vertical and lateral $MoS_2/MoSe_2$ heterostructures was established and it is demonstrated that the growth for monolayer TMDs can be extended to bilayer crystals as well as bilayer architectures of the $MoS_2/MoSe_2$ system, such as homo-to-heterobilayer and hetero-homobilayer junctions.

These heterostructure systems were grown one layer directly after the other during a single growth run. This was achieved by loading the respective materials in the setup simultaneously and changing the chalcogen precursor in the growth environment by changing the carrier gas flow direction inside the furnace. This method maintains the specific out-of-equilibrium condition of the first growth to initiate the second growth without having to ramp down to room temperature and thus terminating the growth. However, this approach may promote cross-contamination between heterostructural layers and may lead to the formation of alloy systems. This alloy effect was observed for lateral heterostructures through energy-dispersive X-ray spectroscopy and in optical spectroscopy, where shifts of the exciton resonance were detected. Additionally, the shift of the resonance continuously spans across several tens of micrometers, indicating a gradual change in precursor concentration during the growth time and resulting in alloy gradients within the crystal. This alloy effect in the $MoS_2/MoSe_2$ system was further exploited and a growth configuration was introduced that allowed to control-

lably grow $MoSe_{2(x-1)}S_{2x}$ monolayer alloys continuously within the full range of sulfur content ($0 < x < 1$), in contrast to previous studies [312, 313].

Based on the initial growth methodology described in Section 4.2.2, the optimizations and improvements implemented to increase control over the growth process, increase yield, and allow for reproducible results involved a redistribution of precursors across multiple chambers to directly access the individual precursor temperature profiles during the growth, while pre-growth weighing of the precursors allowed for tracking and variation of material quantities. These changes, together with the incorporation of multiple precursors during heterostructure growth, significantly expanded the parameter space and allowed for more control. Furthermore, the total growth time was reduced by half, from 100 minutes to 50 minutes, which increased the sampling rate of the parameter space. These improvements were crucial for direct heterostructure growth and high-throughput projects, such as publication [P7], where 40 functional samples were fabricated, along with numerous others that did not make the final count.

To monitor changes between growth processes, as parameters were adjusted, optical imaging was employed to ensure the out-of-equilibrium condition of the growth and a high desorption rate of precursors off the substrate during the nucleation process (as discussed in Section 4.1). This was reflected in the formation of well-separated, triangular crystals of significant size, typically ranging from 50 to 200 µm. Large deviations from optimal growth conditions resulted in disordered multilayer growth, irregularly shaped crystals with multicornered edges, or very small, closely-spaced deposition spots of less than 2 µm. Smaller deviations where monitored through slight changes in shape of the crystal edge. Ultimately, well-shaped crystals were selected for sample fabrication, with contrast homogeneity confirmed using high-contrast imaging techniques.

The fabrication process involved a series of methods to electrically contact TMD samples with multilayer graphene or gold, encapsulate them in hexagonal boron nitride (hBN), and gate them using multilayer graphene. Lithography and evaporation techniques were used to electrically contact the sample and all gates on the desired substrate, as detailed in Section 3.2. While most techniques were standard for two-dimensional material fabrication, new methods were developed in the scope of this work. This included the incorporation of an annealing step during the pick-up procedure to increase bonding between the hBN and the TMD as well as the introduction of a novel carving technique. These innovations were necessary as CVD-grown TMD layers, which are closely adhered to their growth substrates, are more difficult to pick up using viscoelastic stamping compared to exfoliated samples, where the conventional method suffices.

In terms of characterization, EDX spectroscopy in a scanning electron microscope (SEM) was optimized to increase its resolution and achieve layer-resolving sensitivity down to the two-dimensional limit [P9]. Numerical simulations and experimental data guided the optimization of operational parameters, particularly by adjusting the geometrical tilt angle to enhance the interaction volume and selecting appropriate electron beam energies for increased ionization efficiency. These optimizations allowed for precise EDX measurements in both exfoliated and CVD-grown samples, enabling the distinction of cross-contamination and alloying in CVD-grown heterostructures with a spatial resolution of 300 nm. These advancements expanded the experimental toolbox for quantitative characterization of two-dimensional materials and their heterostructures.

The layer-resolution of EDX spectroscopy was further applied to secondary electron imaging, which allowed for the resolution of intensity variations based on the penetration angle of primary electrons and with it the differentiation between stacking orders in homo- and heterobilayers [P7]. By optimizing imaging conditions, such as tilt and rotation angles, domains with distinct atomic registries in both homobilayers and heterobilayers were spatially resolved. These results, combined with optical spectroscopy and theoretical simulations, were used to study mesoscopic reconstruction of the moiré superlattices in the heterobilayer $MoSe_2/WSe_2$ [P8]. The results revealed the existence of registry-contrasting domains in closely lattice-matched heterobilayer systems showing complete reconstruction into distinct stacking configurations across micron-sized two-dimensional domains, one-dimensional wires, or zero-dimensional quantum dot arrays, with distinct optical excitonic signatures. Moreover, exciton diffusion was studied in an extended region of a reconstructed H^h_h-stacking domain in the same material system of $MoSe_2/WSe_2$ [P6]. The mesoscopically reconstructed domain allowed for the observation of the propagation properties of interlayer excitons independent from trapping at moiré- or disorder-induced local potentials.

Furthermore, the high optical quality monolayers of $MoSe_2$ grown by CVD were incorporated into numerous samples of twisted heterobilayers of $MoSe_2/WS_2$ to study excitons in the moiré superlattice formed between the lattice-mismatched layers ([P2], [P3], [P5] and [P10]). These studies collectively examined various moiré exciton states under electric and magnetic fields, as well as varying charge-doping levels, down to the milli-Kelvin regime, revealing novel correlated effects.

Finally, monolayer MoS_2 on gold was studied using a scanning tunneling microscope (STM). Strained regions of the monolayer, caused by atomic steps in the gold surface, were compared to unstrained regions, allowing for the investigation of exciton-induced

band renormalization. The study revealed enhanced excitonic interactions and band-structure modifications in the strained regions, emphasizing the impact of local strain on exciton behavior [P4].

Two-dimensional TMDs provide a novel platform for exploring strongly interacting many-body physics through engineered moiré superlattices in heterobilayers and multilayers. However, beyond fundamental research, TMDs hold great promise for practical applications due to their low dimensionality, high electron mobility, strong light-matter interactions, and valley-conserving physics. This makes them ideal candidates for a range of applications such as next-generation transistor technology and on-chip photonics. To scale such technologies, it is crucial to overcome the restrictions of exfoliation-based sample fabrication and develop methods of growth that can be incorporated into existing semiconductor manufacturing processes. The key challenges lie in achieving wafer-scale growth, whether through continuous monocrystalline films or site-selective, deterministic growth, while maintaining low defect densities to preserve desirable optical and electrical properties. Promising approaches involve engineering the substrate interaction through precursor partial pressure engineering (Section 4.3.3) or other methods to control growth locations [192, 193, 330]. Additionally, the high temperatures required for CVD growth pose compatibility issues with other materials in semiconductor processing [331]. Here, plasma-enhanced CVD (PECVD) has shown potential in reducing reaction temperatures [332–334], offering a path to overcome this limitation. At the same time, such growths potentially need to include angle control of the layer with its substrate. Significant progress has been made in this direction of epitaxial growth by growing on step edges of the underlying substrate [247, 335, 336].

For the current setup, further optimization can be achieved by separating the growth chamber from the molybdenum precursor. Since the substrates are placed directly above the precursor, to allow for high concentrations, there is no discrimination between the precursor evaporation temperature and the growth temperature. By separation of these two processes, a higher control may be achieved. Furthermore, it is noted that the pressure of the growth in the current setup is set equal to the pressure of the outside environment, which may have an influence on the growth within pressure fluctuations of $\sim \pm 10$ millibar. To further increase control over the growth, a precise pressure control is needed. This ties in with a higher degree of precursor concentration control which can be achieved by more precise flow controllers in addition to implementing control of the flow of precursor material into the growth chamber. This method is generally implemented in more sophisticated grow methodologies of metal-

organic CVD (MOCVD) and molecular beam epitaxy (MBE) [337–339]. Additionally, differences in growth behavior between different precursor sources were observed. These involved the powders for the molybdenum precursor where powders stemming from different lots in production or different production sources displayed a difference in growth behavior. Even though the purity of the precursors was specified to > 99%, either the remaining impurities or the grain sizes within the powder plausibly influence growth outcomes. This behavior should be taken into account for further studies.

Finally, the family of two-dimensional TMDs extends far beyond the materials studied in this thesis, with many others experimentally realized or currently only predicted theoretically [8, 274]. The insight gained from growing the MX_2 compounds of this thesis via CVD, may be applicable to other members of the TMD family, broadening the scope of possibilities for two-dimensional materials and their potential applications.

Bibliography

1. Queisser, H. J. *Forword to: Semiconductor Physics by Böer, Karl W. and Pohl, Udo W.* (Springer International Publishing, 2018).
2. Kang, K. *et al.* High-mobility three-atom-thick semiconducting films with wafer-scale homogeneity. *Nature* **520,** 656–660 (2015).
3. Novoselov, K. S. *et al.* Electric field effect in atomically thin carbon films. *Science* **306,** 666–669 (2004).
4. Geim, A. K. & Novoselov, K. S. The rise of graphene. *Nat. Mater.* **6,** 183–191 (2007).
5. Novoselov, K. S. *et al.* Two-dimensional atomic crystals. *PNAS* **102,** 10451–10453 (2005).
6. Meyer, J. C. *et al.* The structure of suspended graphene sheets. *Nature* **446,** 60–63 (2007).
7. Novoselov, K. S. Nobel lecture: Graphene: Materials in the flatland. *Rev. Mod. Phys.* **83,** 837 (2011).
8. Mounet, N. *et al.* Two-dimensional materials from high-throughput computational exfoliation of experimentally known compounds. *Nat. Nanotechnol.* **13,** 246–252 (2018).
9. Watanabe, K., Taniguchi, T. & Kanda, H. Direct-bandgap properties and evidence for ultraviolet lasing of hexagonal boron nitride single crystal. *Nat. Mater.* **3,** 404–409 (2004).
10. Cooper, D. R. *et al.* Experimental review of graphene. *ISRN* **2012,** 1–56 (2012).
11. Wang, Q. H. *et al.* Electronics and optoelectronics of two-dimensional transition metal dichalcogenides. *Nat. Nanotechnol.* **7,** 699–712 (2012).
12. Wang, H. *et al.* High-quality monolayer superconductor NbSe2 grown by chemical vapour deposition. *Nat. Commun.* **8** (2017).

13. Frindt, R. F. & Yoffe, A. D. Physical properties of layer structures: optical properties and photoconductivity of thin crystals of molybdenum disulphide. *Proc. R. Soc. Lond. A. Proc. R. Soc. A: Math.* **273,** 69–83 (1963).

14. Frindt, R. F. Single crystals of MoS_2 several molecular layers thick. *J. Appl. Phys.* **37,** 1928–1929 (1966).

15. Wilson, J. A. & Yoffe, A. The transition metal dichalcogenides discussion and interpretation of the observed optical, electrical and structural properties. *Adv. Phys.* **18,** 193–335 (1969).

16. Splendiani, A. *et al.* Emerging photoluminescence in monolayer MoS_2. *Nano Lett.* **10,** 1271–1275 (2010).

17. Mak, K. F. *et al.* Atomically thin MoS_2: a new direct-gap semiconductor. *Phys. Rev. Lett.* **105,** 136805 (13 2010).

18. Momma, K. & Izumi, F. VESTA 3 for three-dimensional visualization of crystal, volumetric and morphology data. *J. Appl. Crystallogr.* **44,** 1272–1276 (2011).

19. Heising, J. & Kanatzidis, M. G. Exfoliated and restacked MoS_2 and WS_2: ionic or neutral species encapsulation and ordering of hard electropositive cations. *J. Am. Chem. Soc.* **121,** 11720–11732 (1999).

20. Eda, G. *et al.* Coherent atomic and electronic heterostructures of single-layer MoS_2. *ACS Nano* **6,** 7311–7317 (2012).

21. Radisavljevic, B. *et al.* Single-layer MoS_2 transistors. *Nat. Nanotechnol.* **6,** 147–150 (2011).

22. Wang, G. *et al.* Colloquium: Excitons in atomically thin transition metal dichalcogenides. *Rev. Mod. Phys.* **90,** 021001 (2 2018).

23. Chernikov, A. *et al.* Exciton binding energy and nonhydrogenic Rydberg series in monolayer WS_2. *Phys. Rev. Lett.* **113,** 076802 (2014).

24. He, K. *et al.* Tightly bound excitons in monolayer WSe_2. *Phys. Rev. Lett.* **113,** 026803 (2014).

25. Qiu, D. Y., da Jornada, F. H. & Louie, S. G. Optical spectrum of MoS_2: many-body effects and diversity of exciton states. *Phys. Rev. Lett.* **111,** 216805 (2013).

26. Ramasubramaniam, A. Large excitonic effects in monolayers of molybdenum and tungsten dichalcogenides. *Phys. Rev. B* **86,** 115409 (2012).

27. Wang, G. *et al.* Giant enhancement of the optical second-harmonic emission of WSe_2 monolayers by laser excitation at exciton resonances. *Phys. Rev. Lett.* **114,** 097403 (2015).

28. Ye, Z. *et al.* Probing excitonic dark states in single-layer tungsten disulphide. *Nature* **513,** 214–218 (2014).

29. Yao, W., Xiao, D. & Niu, Q. Valley-dependent optoelectronics from inversion symmetry breaking. *Phys. Rev. B* **77,** 235406 (2008).

30. Xiao, D. *et al.* Coupled spin and valley physics in monolayers of MoS_2 and other group-VI dichalcogenides. *Phys. Rev. Lett.* **108,** 1 (2012).

31. Cheiwchanchamnangij, T. & Lambrecht, W. R. L. Quasiparticle band structure calculation of monolayer, bilayer, and bulk MoS_2. *Phys. Rev. B* **85,** 205302 (2012).

32. Zhu, Z. Y., Cheng, Y. C. & Schwingenschlögl, U. Giant spin-orbit-induced spin splitting in two-dimensional transition-metal dichalcogenide semiconductors. *Phys. Rev. B* **84,** 153402 (2011).

33. Miwa, J. A. *et al.* Electronic structure of epitaxial single-layer MoS_2. *Phys. Rev. Lett.* **114,** 046802 (2015).

34. Zhang, Y. *et al.* Direct observation of the transition from indirect to direct bandgap in atomically thin epitaxial $MoSe_2$. *Nat. Nanotechnol.* **9,** 111–115 (2013).

35. Arora, A. *et al.* Excitonic resonances in thin films of WSe_2: from monolayer to bulk material. *Nanoscale* **7,** 10421–10429 (2015).

36. Zhang, X.-X. *et al.* Experimental evidence for dark excitons in monolayer WSe_2. *Phys. Rev. Lett.* **115,** 257403 (2015).

37. International Roadmap for Devices and Systems Executive Summary 2022. *IEEE* (2022).

38. Li, N. *et al.* Large-scale flexible and transparent electronics based on monolayer molybdenum disulfide field-effect transistors. *Nat. Electron.* **3,** 711–717 (2020).

39. Moore, G. E. Cramming more components onto integrated circuits, Reprinted from Electronics, volume 38, number 8, April 19, 1965, pp.114 ff. *IEEE Solid-State Circuits Society Newsletter* **11,** 33–35 (2006).

40. Tuomi, I. The lives and death of Moore's law. *First Monday* (2002).

41. Fu, N. *et al.* EUV lithography: state-of-the-art review. *J. microelectron. manuf.* **2,** 1–6 (2019).

42. International Roadmap for Devices and Systems 2023. *IEEE* (2023).

43. Desai, S. B. *et al.* MoS_2 transistors with 1-nanometer gate lengths. *Science* **354,** 99–102 (2016).

44. Xu, K. *et al.* Sub-10 nm nanopattern architecture for 2D material field-effect transistors. *Nano Lett.* **17,** 1065–1070 (2017).

45. Xie, L. *et al.* Graphene-contacted ultrashort channel monolayer MoS_2 transistors. *Adv. Mater.* **29** (2017).

46. Zhu, Y. *et al.* Monolayer molybdenum disulfide transistors with single-atom-thick gates. *Nano Lett.* **18,** 3807–3813 (2018).

47. Li, W. *et al.* Uniform and ultrathin high-κ gate dielectrics for two-dimensional electronic devices. *Nat. Electron.* **2,** 563–571 (2019).

48. Chen, J.-H. *et al.* Intrinsic and extrinsic performance limits of graphene devices on SiO_2. *Nat. Nanotechnol.* **3,** 206–209 (2008).

49. Schwierz, F. Graphene transistors. *Nat. Nanotechnol.* **5,** 487–496 (2010).

50. Fivaz, R. & Mooser, E. Mobility of charge carriers in semiconducting layer structures. *Phys. Rev.* **163,** 743–755 (1967).

51. Zhang, Y. *et al.* Ambipolar MoS_2 thin flake transistors. *Nano Lett.* **12,** 1136–1140 (2012).

52. Bao, W. *et al.* High mobility ambipolar MoS_2 field-effect transistors: Substrate and dielectric effects. *Appl. Phys. Lett.* **102** (2013).

53. Kim, S. *et al.* High-mobility and low-power thin-film transistors based on multilayer MoS_2 crystals. *Nat. Commun.* **3** (2012).

54. Radisavljevic, B. & Kis, A. Mobility engineering and a metal–insulator transition in monolayer MoS_2. *Nat. Mater.* **12,** 815–820 (2013).

55. Cui, X. *et al.* Multi-terminal transport measurements of MoS_2 using a van der Waals heterostructure device platform. *Nat. Nanotechnol.* **10,** 534–540 (2015).

56. Chung, Y.-Y. *et al.* Demonstration of 40-nm channel length top-gate p-MOSFET of WS_2 channel directly grown on SiO_x/Si substrates using area-selective CVD technology. *IEEE Transactions on Electron Devices* **66,** 5381–5386 (2019).

57. Sachid, A. B. *et al.* Monolithic 3D CMOS using layered semiconductors. *Adv. Mater.* **28,** 2547–2554 (2016).

58. Chen, M.-L. *et al.* A FinFET with one atomic layer channel. *Nat. Commun.* **11** (2020).

59. Xu, X. *et al.* Spin and pseudospins in layered transition metal dichalcogenides. *Nat. Phys.* **10,** 343 (2014).

60. Cao, T. *et al.* Valley-selective circular dichroism of monolayer molybdenum disulphide. *Nat. Commun.* **3** (2012).

61. Zeng, H. *et al.* Valley polarization in MoS_2 monolayers by optical pumping. *Nat. Nanotechnol.* **7,** 490–493 (2012).

62. Mak, K. F. *et al.* Control of valley polarization in monolayer MoS_2 by optical helicity. *Nat. Nanotechnol.* **7,** 494–498 (2012).

63. Jones, A. M. *et al.* Optical generation of excitonic valley coherence in monolayer WSe_2. *Nat. Nanotechnol.* **8,** 634–638 (2013).

64. Mak, K. F. *et al.* The valley Hall effect in MoS_2 transistors. *Science* **344,** 1489–1492 (2014).

65. Zhang, Y. J. *et al.* Electrically switchable chiral light-emitting transistor. *Science* **344,** 725–728 (2014).

66. Yang, W. *et al.* Electrically tunable valley-light emitting diode (vLED) based on CVD-grown monolayer WS_2. *Nano Lett.* **16,** 1560–1567 (2016).

67. Wu, Z. *et al.* Intrinsic valley Hall transport in atomically thin MoS_2. *Nat. Commun.* **10** (2019).

68. Hung, T. Y. T. *et al.* Direct observation of valley-coupled topological current in MoS_2. *Science Advances* **5** (2019).

69. Mueller, T. & Malic, E. Exciton physics and device application of two-dimensional transition metal dichalcogenide semiconductors. *npj 2D mater. appl.* **2** (2018).

70. Lopez-Sanchez, O. *et al.* Ultrasensitive photodetectors based on monolayer MoS_2. *Nat. Nanotechnol.* **8,** 497–501 (2013).

71. Fu, Q. *et al.* Excitonic emission in atomically thin electroluminescent devices. *Laser Photonics Rev.* **15** (2021).

72. Reed, G. T. *et al.* Silicon optical modulators. *Nat. Photonics* **4,** 518–526 (2010).

73. Sun, Z., Martinez, A. & Wang, F. Optical modulators with 2D layered materials. *Nat. Photonics* **10,** 227–238 (2016).

74. Datta, I. *et al.* Low-loss composite photonic platform based on 2D semiconductor monolayers. *Nat. Photonics* **14,** 256–262 (2020).

75. Geim, A. K. & Grigorieva, I. V. Van der Waals heterostructures. *Nature* **499,** 419–425 (2013).

76. Novoselov, K. S. *et al.* 2D materials and van der Waals heterostructures. *Science* **353** (2016).

77. Castellanos-Gomez, A. *et al.* Van der Waals heterostructures. *Nat. Rev. Methods Primers* **2** (2022).

78. Chernikov, A. *et al.* Exciton binding energy and nonhydrogenic Rydberg series in monolayer WS_2. *Phys. Rev. Lett.* **113,** 076802 (2014).

79. Molas, M. R. *et al.* Energy spectrum of two-dimensional excitons in a nonuniform dielectric medium. *Phys. Rev. Lett.* **123,** 136801 (2019).

80. Stier, A. V. *et al.* Magnetooptics of exciton Rydberg states in a monolayer semiconductor. *Phys. Rev. Lett.* **120,** 057405 (2018).

81. Goryca, M. *et al.* Revealing exciton masses and dielectric properties of monolayer semiconductors with high magnetic fields. *Nat. Commun.* **10** (2019).

82. Arora, A. *et al.* Excited-state trions in monolayer WS_2. *Phys. Rev. Lett.* **123,** 167401 (2019).

83. Stier, A. V. *et al.* Probing the influence of dielectric environment on excitons in monolayer WSe_2: insight from high magnetic fields. *Nano Lett.* **16,** 7054–7060 (2016).

84. Raja, A. *et al.* Coulomb engineering of the bandgap and excitons in two-dimensional materials. *Nat. Commun.* **8** (2017).

85. Hsu, W.-T. *et al.* Dielectric impact on exciton binding energy and quasiparticle bandgap in monolayer WS_2 and WSe_2. *2D Mater.* **6,** 025028 (2019).

86. Riis-Jensen, A. C. *et al.* Anomalous exciton Rydberg series in two-dimensional semiconductors on high-κ dielectric substrates. *Phys. Rev. B* **102,** 201402 (2020).

87. Lee, G.-H. *et al.* Highly stable, dual-gated MoS_2 transistors encapsulated by hexagonal boron nitride with gate-controllable contact, resistance, and threshold voltage. *ACS Nano* **9,** 7019–7026 (2015).

88. Ajayi, O. A. *et al.* Approaching the intrinsic photoluminescence linewidth in transition metal dichalcogenide monolayers. *2D Mater.* **4,** 031011 (2017).

89. Cadiz, F. *et al.* Excitonic linewidth approaching the homogeneous limit in MoS_2-based van der Waals heterostructures. *Phys. Rev. X* **7,** 021026 (2017).

90. Wierzbowski, J. *et al.* Direct exciton emission from atomically thin transition metal dichalcogenide heterostructures near the lifetime limit. *Sci. Rep.* **7** (2017).

91. Fang, H. *et al.* Strong interlayer coupling in van der Waals heterostructures built from single-layer chalcogenides. *PNAS* **111,** 6198–6202 (2014).

92. Kim, M. S. *et al.* Simultaneous hosting of positive and negative trions and the enhanced direct band emission in $MoSe_2/MoS_2$ heterostacked multilayers. *ACS Nano* **10,** 6211–6219 (May 2016).

93. Calman, E. V. *et al.* Indirect excitons in van der Waals heterostructures at room temperature. *Nat. Commun.* **9** (2018).

94. Shimazaki, Y. *et al.* Strongly correlated electrons and hybrid excitons in a moiré heterostructure. *Nature* **580,** 472–477 (2020).

95. Zerba, C. *et al.* Realizing topological superconductivity in tunable Bose-Fermi mixtures with transition metal dichalcogenide heterostructures. *Phys. Rev. Lett.* **133,** 056902 (2024).

96. Yu, Y. *et al.* Equally efficient interlayer exciton relaxation and improved absorption in epitaxial and nonepitaxial MoS_2/WS_2 heterostructures. *Nano Lett.* **15,** 486–491 (2014).

97. Zhang, J. *et al.* Observation of strong interlayer coupling in MoS_2/WS_2 heterostructures. *Adv. Mater.* **28,** 1950–1956 (2015).

98. Lin, Y.-C. *et al.* Atomically thin resonant tunnel diodes built from synthetic van der Waals heterostructures. *Nat. Commun.* **6** (2015).

99. Gong, Y. *et al.* Two-step growth of two-dimensional $WSe_2/MoSe_2$ heterostructures. *Nano Lett.* **15,** 6135–6141 (2015).

100. He, Y. *et al.* Strain-induced electronic structure changes in stacked van der Waals heterostructures. *Nano Lett.* **16,** 3314–3320 (2016).

101. Nikam, R. D. *et al.* Epitaxial growth of vertically stacked p-MoS_2/n-MoS_2 heterostructures by chemical vapor deposition for light emitting devices. *Nano Energy* **32,** 454–462 (2017).

102. Zhang, C. *et al.* Interlayer couplings, Moiré patterns, and 2D electronic superlattices in MoS_2/WSe_2 hetero-bilayers. *Science Advances* **3** (2017).

103. Carozo, V. *et al.* Excitonic processes in atomically-thin $MoSe_2/MoS_2$ vertical heterostructures. *2D Mater.* **5,** 031016 (2018).

104. Ding, Y. *et al.* Stacking-mode confined growth of 2H-$MoTe_2/MoS_2$ bilayer heterostructures for UV–vis–IR photodetectors. *Nano Energy* **49,** 200–208 (2018).

105. Zhang, X. *et al.* Controllable one-step growth of bilayer MoS_2-WS_2/WS_2 heterostructures by chemical vapor deposition. *Nanotechnology* **29,** 455707 (2018).

106. Li, F. *et al.* Rational kinetics control toward universal growth of 2D vertically stacked heterostructures. *Adv. Mater.* **31** (2019).

107. Wu, X. *et al.* Vapor growth of WSe_2/WS_2 heterostructures with stacking dependent optical properties. *Nano Research* **12,** 3123–3128 (2019).

108. Yuan, L. *et al.* Twist-angle-dependent interlayer exciton diffusion in WS_2-WSe_2 heterobilayers. *Nat. Mater.* **19,** 617–623 (2020).

109. Xia, J. *et al.* Strong coupling and pressure engineering in WSe_2-$MoSe_2$ heterobilayers. *Nat. Phys.* **17,** 92–98 (2020).

110. Irisawa, T. *et al.* CVD grown bilayer $WSe_2/MoSe_2$ heterostructures for high performance tunnel transistors. *JJAP* **59,** SGGH05 (2020).

111. Kim, B. *et al.* Large surface photovoltage of WS_2/MoS_2 and MoS_2/WS_2 vertical hetero-bilayers. *ACS Appl. Electron. Mater.* **3,** 2601–2606 (2021).

112. Wan, Y. *et al.* Strain-directed layer-by-layer epitaxy toward van der Waals homo- and heterostructures. *ACS Materials Letters* **3,** 442–453 (2021).

113. Li, Z. *et al.* Lattice reconstruction in $MoSe_2$-WSe_2 heterobilayers synthesized by chemical vapor deposition. *Nano Lett.* **23,** 4160–4166 (2023).

114. Davies, F. H. *et al.* Band alignment of transition metal dichalcogenide heterostructures. *Phys. Rev. B* **103,** 045417 (2021).

115. Anderson, R. L. Germanium-gallium arsenide heterojunctions [Letter to the Editor]. *IBM J. Res. Dev.* **4,** 283–287 (1960).

116. Zhang, C. *et al.* Systematic study of electronic structure and band alignment of monolayer transition metal dichalcogenides in Van der Waals heterostructures. *2D Mater.* **4,** 015026 (2016).

117. Nguyen, P. V. *et al.* Visualizing electrostatic gating effects in two-dimensional heterostructures. *Nature* **572,** 220–223 (2019).

118. Schmitt, D. *et al.* Formation of moiré interlayer excitons in space and time. *Nature* **608,** 499–503 (2022).

119. Meneghini, G., Brem, S. & Malic, E. Ultrafast phonon-driven charge transfer in van der Waals heterostructures. *Natural Sciences* **2** (2022).

120. Meneghini, G. *et al.* Hybrid exciton signatures in ARPES spectra of van der Waals materials. *ACS Photonics* **10,** 3570–3575 (2023).

121. Alexeev, E. M. *et al.* Resonantly hybridized excitons in moiré superlattices in van der Waals heterostructures. *Nature* **567,** 81–86 (2019).

122. Kiemle, J. *et al.* Control of the orbital character of indirect excitons in MoS_2/WS_2 heterobilayers. *Phys. Rev. B* **101,** 121404 (2020).

123. Tang, Y. *et al.* Tuning layer-hybridized moiré excitons by the quantum-confined Stark effect. *Nat. Nanotechnol.* **16,** 52–57 (2020).

124. Tagarelli, F. *et al.* Electrical control of hybrid exciton transport in a van der Waals heterostructure. *Nat. Photonics* **17,** 615–621 (2023).

125. Nagler, P. *et al.* Interlayer exciton dynamics in a dichalcogenide monolayer heterostructure. *2D Mater.* **4,** 025112 (2017).

126. Rivera, P. *et al.* Observation of long-lived interlayer excitons in monolayer $MoSe_2$-WSe_2 heterostructures. *Nat. Commun.* **6** (2015).

127. Rivera, P. *et al.* Interlayer valley excitons in heterobilayers of transition metal dichalcogenides. *Nat. Nanotechnol.* **13,** 1004–1015 (2018).

128. Ovesen, S. *et al.* Interlayer exciton dynamics in van der Waals heterostructures. *Communications Physics* **2** (2019).

129. Barré, E. *et al.* Optical absorption of interlayer excitons in transition-metal dichalcogenide heterostructures. *Science* **376,** 406–410 (2022).

130. Unuchek, D. *et al.* Room-temperature electrical control of exciton flux in a van der Waals heterostructure. *Nature* **560,** 340–344 (2018).

131. Jiang, Y. *et al.* Interlayer exciton formation, relaxation, and transport in TMD van der Waals heterostructures. *Light: Science and Applications* **10** (2021).

132. Rosati, R. *et al.* Two dimensional semiconductors: optical and electronic properties. *arXiv* (2024).

133. Andrei, E. Y. *et al.* The marvels of moiré materials. *Nat. Rev. Mater.* **6,** 201–206 (2021).

134. Wilson, N. P. *et al.* Excitons and emergent quantum phenomena in stacked 2D semiconductors. *Nature* **599,** 383–392 (2021).

135. Regan, E. C. *et al.* Emerging exciton physics in transition metal dichalcogenide heterobilayers. *Nat. Rev. Mater.* **7,** 778–795 (2022).

136. Mak, K. F. & Shan, J. Semiconductor moiré materials. *Nat. Nanotechnol.* **17,** 686–695 (2022).

137. Huang, D. *et al.* Excitons in semiconductor moiré superlattices. *Nat. Nanotechnol.* **17,** 227–238 (2022).

138. Du, L. *et al.* Moiré photonics and optoelectronics. *Science* **379** (2023).

139. Hermann, K. Periodic overlayers and moiré patterns: theoretical studies of geometric properties. *J. Phys. Condens. Matter* **24,** 314210 (2012).

140. Zhang, N. *et al.* Moiré intralayer excitons in a $MoSe_2/MoS_2$ heterostructure. *Nano Lett.* **18,** 7651–7657 (2018).

141. Seyler, K. L. *et al.* Signatures of moiré-trapped valley excitons in $MoSe_2$ /WSe_2 heterobilayers. *Nature* **567,** 66 (Mar. 2019).

142. Jin, C. *et al.* Observation of moiré excitons in WSe_2/WS_2 heterostructure superlattices. *Nature* **567,** 76 (Mar. 2019).

143. Tran, K. *et al.* Evidence for moiré excitons in van der Waals heterostructures. *Nature* **567,** 71–75 (2019).

144. Baek, H. *et al.* Highly energy-tunable quantum light from moiré-trapped excitons. *Science Advances* **6** (2020).

145. Liu, E. *et al.* Signatures of moiré trions in $WSe_2/MoSe_2$ heterobilayers. *Nature* **594,** 46–50 (2021).

146. Wang, X. *et al.* Moiré trions in $MoSe_2/WSe_2$ heterobilayers. *Nat. Nanotechnol.* **16,** 1208–1213 (2021).

147. Kim, H. *et al.* Dynamics of Moiré trion and its valley polarization in a microfabricated $WSe_2/MoSe_2$ heterobilayer. *ACS Nano* **17,** 13715–13723 (July 2023).

148. Liu, Z. *et al.* Distinct moiré trions in a twisted semiconductor homobilayer. *arXiv* (2024).

149. Li, T. *et al.* Quantum anomalous Hall effect from intertwined moiré bands. *Nature* **600,** 641–646 (2021).

150. Cai, J. *et al.* Signatures of fractional quantum anomalous Hall states in twisted $MoTe_2$. *Nature* **622,** 63–68 (2023).

151. Zeng, Y. *et al.* Thermodynamic evidence of fractional Chern insulator in moiré $MoTe_2$. *Nature* **622,** 69–73 (2023).

152. Park, H. *et al.* Observation of fractionally quantized anomalous Hall effect. *Nature* **622,** 74–79 (2023).

153. Xu, F. *et al.* Observation of Integer and Fractional Quantum Anomalous Hall Effects in Twisted Bilayer $MoTe_2$. *Phys. Rev. X* **13,** 031037 (2023).

154. Uri, A. *et al.* Superconductivity and strong interactions in a tunable moiré quasicrystal. *Nature* **620,** 762–767 (2023).

155. Kang, K. *et al.* Observation of the double quantum spin Hall phase in moiré WSe_2. *arXiv* (2024).

156. Yu, H. *et al.* Moiré excitons: From programmable quantum emitter arrays to spin-orbit–coupled artificial lattices. *Sci. Adv.* **3,** e1701696 (2017).

157. Wu, F., Lovorn, T. & MacDonald, A. H. Topological exciton bands in moiré heterojunctions. *Phys. Rev. Lett.* **118,** 147401 (2017).

158. Tong, Q. *et al.* Topological mosaics in moiré superlattices of van der Waals heterobilayers. *Nat. Phys.* **13,** 356–362 (2017).

159. Wu, F. *et al.* Hubbard model physics in transition metal dichalcogenide moiré bands. *Phys. Rev. Lett.* **121,** 026402 (2018).

160. Wang, Z. *et al.* Evidence of high-temperature exciton condensation in two-dimensional atomic double layers. *Nature* **574,** 76–80 (2019).

161. Regan, E. C. *et al.* Mott and generalized Wigner crystal states in WSe_2/WS_2 moiré superlattices. *Nature* **579,** 359–363 (2020).

162. Tang, Y. *et al.* Simulation of Hubbard model physics in WSe_2/WS_2 moiré superlattices. *Nature* **579,** 353–358 (2020).

163. Xu, Y. *et al.* Correlated insulating states at fractional fillings of moiré superlattices. *Nature* **587,** 214–218 (2020).

164. Zhang, Y., Yuan, N. F. Q. & Fu, L. Moiré quantum chemistry: Charge transfer in transition metal dichalcogenide superlattices. *Phys. Rev. B* **102,** 201115 (2020).

165. Kennes, D. M. *et al.* Moiré heterostructures as a condensed-matter quantum simulator. *Nat. Phys.,* 1–9 (2021).

166. Huang, X. *et al.* Correlated insulating states at fractional fillings of the WS_2/WSe_2 moiré lattice. *Nat. Phys.* **17,** 715–719 (2021).

167. Ciorciaro, L. *et al.* Kinetic magnetism in triangular moiré materials. *Nature* **623,** 509–513 (2023).

168. Foutty, B. A. *et al.* Mapping twist-tuned multiband topology in bilayer WSe_2. *Science* **384,** 343–347 (2024).

169. Zhao, W. *et al.* Realization of the Haldane Chern insulator in a moiré lattice. *Nat. Phys.* **20,** 275–280 (2024).

170. Gao, B. *et al.* Excitonic Mott insulator in a Bose-Fermi-Hubbard system of moiré WS_2/WSe_2 heterobilayer. *Nat. Commun.* **15** (2024).

171. Ahn, S. J. *et al.* Dirac electrons in a dodecagonal graphene quasicrystal. *Science* **361,** 782–786 (2018).

172. Sun, L. *et al.* Hetero-site nucleation for growing twisted bilayer graphene with a wide range of twist angles. *Nat. Commun.* **12** (2021).

173. Fortin-Deschênes, M. *et al.* Van der Waals epitaxy of tunable moirés enabled by alloying. *Nat. Mater.* **23,** 339–346 (2023).

174. Gong, Y. *et al.* Vertical and in-plane heterostructures from WS_2/MoS_2 monolayers. *Nat. Mater.* **13,** 1135–1142 (2014).

175. Duan, X. *et al.* Lateral epitaxial growth of two-dimensional layered semiconductor heterojunctions. *Nat. Nanotechnol.* **9,** 1024–1030 (2014).

176. Huang, C. *et al.* Lateral heterojunctions within monolayer $MoSe_2$-WSe_2 semiconductors. *Nat. Mater.* **13,** 1096–1101 (2014).

177. Li, M.-Y. *et al.* Epitaxial growth of a monolayer WSe_2 -MoS_2 lateral p-n junction with an atomically sharp interface. *Science* **349,** 524–528 (2015).

178. Heo, H. *et al.* Rotation-misfit-free heteroepitaxial stacking and stitching growth of hexagonal transition-metal dichalcogenide monolayers by nucleation kinetics controls. *Adv. Mater.* **27,** 3803–3810 (2015).

179. Zhang, C. *et al.* Strain distributions and their influence on electronic structures of WSe_2-MoS_2 laterally strained heterojunctions. *Nat. Nanotechnol.* **13,** 152–158 (2018).

180. Xie, S. *et al.* Coherent, atomically thin transition-metal dichalcogenide superlattices with engineered strain. *Science* **359,** 1131–1136 (2018).

181. Sahoo, P. K. *et al.* One-pot growth of two-dimensional lateral heterostructures via sequential edge-epitaxy. *Nature* **553,** 63–67 (2018).

182. Najafidehaghani, E. *et al.* 1D p–n junction electronic and optoelectronic devices from transition metal dichalcogenide lateral heterostructures grown by one-pot chemical vapor deposition synthesis. *Adv. Funct. Mater.* **31** (2021).

183. Yuan, L. *et al.* Non-equilibrium first-order exciton Mott transition at monolayer lateral heterojunctions visualized by ultrafast microscopy. *arXiv* (2021).

184. Beret, D. *et al.* Exciton spectroscopy and unidirectional transport in $MoSe_2$-WSe_2 lateral heterostructures encapsulated in hexagonal boron nitride. *npj 2D mater. appl.* **6** (2022).

185. Ichinose, N. *et al.* Two-dimensional atomic-scale ultrathin lateral heterostructures. *arXiv* (2022).

186. Rosati, R. *et al.* Interface engineering of charge-transfer excitons in 2D lateral heterostructures. *Nat. Commun.* **14** (2023).

187. Sahoo, P. K. *et al.* Bilayer lateral heterostructures of transition-metal dichalcogenides and their optoelectronic response. *ACS Nano* **13,** 12372–12384 (2019).

188. Furchi, M. M. *et al.* Device physics of van der Waals heterojunction solar cells. *npj 2D mater. appl.* **2** (2018).

189. Prabhu, P., Jose, V. & Lee, J.-M. Design Strategies for Development of TMD-Based Heterostructures in Electrochemical Energy Systems. *Matter* **2,** 526–553 (2020).

190. Kennes, D. M. *et al.* Moiré heterostructures as a condensed-matter quantum simulator. *Nat. Phys.* **17,** 155–163 (2021).

191. Gherabli, R. *et al.* $MoSe_2/WS_2$ heterojunction photodiode integrated with a silicon nitride waveguide for near infrared light detection with high responsivity. *Light: Science and Applications* **12** (2023).

192. Li, J. *et al.* General synthesis of two-dimensional van der Waals heterostructure arrays. *Nature* **579,** 368–374 (2020).

193. Kim, K. S. *et al.* Non-epitaxial single-crystal 2D material growth by geometric confinement. *Nature* **614,** 88–94 (2023).

194. Taniguchi, T. & Watanabe, K. Synthesis of high-purity boron nitride single crystals under high pressure by using Ba–BN solvent. *J. Cryst. Growth* **303,** 525–529 (2007).

195. Funk, V. *Spectroscopy of momentum-dark excitons in layered semiconductors* Master Thesis (Ludwig-Maximilians-University, Munich, 2017).

196. Castellanos-Gomez, A. *et al.* Deterministic transfer of two-dimensional materials by all-dry viscoelastic stamping. *2D Mater.* **1,** 011002 (2014).

197. Pizzocchero, F. *et al.* The hot pick-up technique for batch assembly of van der Waals heterostructures. *Nat. Commun.* **7** (2016).

198. Purdie, D. G. *et al.* Cleaning interfaces in layered materials heterostructures. *Nat. Commun.* **9** (2018).

199. Göser, J. *Fabrication and optical spectroscopy of twisten van der Waals heterostructures* Master Thesis (Ludwig-Maximilians-University Munich, 2019).

200. Rupp, A. *et al.* Energy-dispersive X-ray spectroscopy of atomically thin semiconductors and heterostructures. *Phys. Rev. Appl.* **18,** 064061 (2022).

201. Son, S. *et al.* Strongly adhesive dry transfer technique for van der Waals heterostructure. *2D Mater.* **7,** 041005 (2020).

202. Krelle, L. *Plasmon-exciton-polaritons in two-dimensional semiconductors strongly coupled to gold nanoparticle arrays* MA thesis (Ludwig-Maximilian-Universität, 2022).

203. Uwanno, T. *et al.* Fully dry PMMA transfer of graphene on h-BN using a heating/cooling system. *2D Mater.* **2,** 041002 (2015).

204. Koós, A. A. *et al.* STM study of the MoS_2 flakes grown on graphite: A model system for atomically clean 2D heterostructure interfaces. *Carbon* **105,** 408–415 (2016).

205. Rao, Q. *et al.* Scratching lithography, manipulation, and soldering of 2D materials using microneedle probes. *AIP Advances* **14** (2024).

206. Tapasztó, L. *et al.* Tailoring the atomic structure of graphene nanoribbons by scanning tunnelling microscope lithography. *Nat. Nanotechnol.* **3,** 397–401 (2008).

207. Magda, G. Z. *et al.* Room-temperature magnetic order on zigzag edges of narrow graphene nanoribbons. *Nature* **514,** 608–611 (2014).

208. Diez-Merida, J. *et al.* High-yield fabrication of bubble-free magic-angle twisted bilayer graphene devices with high twist-angle homogeneity. *arXiv* (2024).

209. Tabataba-Vakili, F. *et al.* Metasurface of strongly coupled excitons and nanoplasmonic arrays. *Nano Lett.* **24,** 10090–10097 (2024).

210. Klingshirn, C. *Semiconductor optics* (Springer Berlin Heidelberg, 2007).

211. Moody, G. *et al.* Intrinsic homogeneous linewidth and broadening mechanisms of excitons in monolayer transition metal dichalcogenides. *Nat. Commun.* **6,** 1 (2015).

212. Fano, U. Effects of configuration interaction on intensities and phase shifts. *Phys. Rev.* **124,** 1866 (1961).

213. Miroshnichenko, A. E., Flach, S. & Kivshar, Y. S. Fano resonances in nanoscale structures. *Rev. Mod. Phys.* **82,** 2257–2298 (2010).

214. Reimer, L. *Scanning electron microscopy: physics of image formation and microanalysis* (Springer Berlin Heidelberg, 1998).

215. Goldstein, J. I. *et al. Scanning electron microscopy and X-ray microanalysis* (Springer New York, 2018).

216. Bell, D. C. & Garratt-Reed, A. J. *Energy dispersive X-ray analysis in the electron microscope* 2003.

217. Bearden, J. A. & Burr, A. F. Reevaluation of X-ray atomic energy levels. *Rev. Mod. Phys.* **39,** 125–142 (1967).

218. Twenty years of 2D materials. *Nat. Phys.* **20,** 1–1 (2024).

219. Huang, Y. *et al.* Reliable exfoliation of large-area high-quality flakes of graphene and other two-dimensional materials. *ACS Nano* **9,** 10612–10620 (2015).

220. Huang, Y. *et al.* Universal mechanical exfoliation of large-area 2D crystals. *Nat. Commun.* **11** (2020).

221. Asahi, H. & Horikoshi, Y. *Molecular beam epitaxy. Materials and applications for electronics and optoelectronics* First edition. 1512 pp. (John Wiley & Sons, Inc, Hoboken, NJ, 2019).

222. Späh, R. *et al.* n-$MoSe_2$/p-WSe_2 heterojunctions. *Appl. Phys. Lett.* **47,** 871–873 (1985).

223. Koma, A., Sunouchi, K. & Miyajima, T. Fabrication and characterization of heterostructures with subnanometer thickness. *Microelectronic Engineering* **2,** 129–136 (1984).

224. Koma, A., Sunouchi, K. & Miyajima, T. Summary Abstract: Fabrication of ultrathin heterostructures with van der Waals epitaxy. *J. Vac. Sci. Technol. B:Nanotechnol. Microelectron.* **3,** 724–724 (1985).

225. Koma, A. & Yoshimura, K. Ultrasharp interfaces grown with Van der Waals epitaxy. *Surface Science* **174,** 556–560 (1986).

226. Ohuchi, F. S. *et al.* van der Waals epitaxial growth and characterization of $MoSe_2$ thin films on SnS_2. *J. Appl. Phys.* **68,** 2168–2175 (1990).

227. Helveg, S. *et al.* Atomic-scale structure of single-layer MoS_2 nanoclusters. *Phys. Rev. Lett.* **84,** 951–954 (2000).

228. Zhan, Y. *et al.* Large-area vapor-phase growth and characterization of MoS_2 atomic layers on a SiO_2 substrate. *Small* **8,** 966–971 (2012).

229. Lee, Y.-H. *et al.* Synthesis of large-area MoS_2 atomic layers with chemical vapor deposition. *Adv. Mater.* **24,** 2320–2325 (2012).

230. Lee, Y.-H. *et al.* Synthesis and transfer of single-layer transition metal disulfides on diverse surfaces. *Nano Lett.* **13,** 1852–1857 (2013).

231. Bilgin, I. *et al.* Chemical vapor deposition synthesized atomically thin molybdenum disulfide with optoelectronic-grade crystalline quality. *ACS Nano* **9,** 8822–8832 (2015).

232. Van der Zande, A. M. *et al.* Grains and grain boundaries in highly crystalline monolayer molybdenum disulphide. *Nat. Mater.* **12,** 554–561 (2013).

233. Chen, W. *et al.* Oxygen-assisted chemical vapor deposition growth of large dingle-Crystal and High-Quality Monolayer MoS_2. *J. Am. Chem. Soc.* **137,** 15632–15635 (2015).

234. Shaw, J. C. *et al.* Chemical vapor deposition growth of monolayer MoSe2 nanosheets. *Nano Research* **7,** 511–517 (2014).

235. Wang, X. *et al.* Chemical vapor deposition growth of crystalline monolayer $MoSe_2$. *ACS Nano* **8,** 5125–5131 (2014).

236. Lin, Y.-C. *et al.* Direct synthesis of van der Waals solids. *ACS Nano* **8,** 3715–3723 (2014).

237. Liu, B. *et al.* Chemical vapor deposition growth of monolayer WSe_2 with tunable device characteristics and growth mechanism study. *ACS Nano* **9,** 6119–6127 (2015).

238. Wang, X. *et al.* Controllable growth of two-dimensional WSe_2 using salt as co-solvent. *CrystEngComm* **20,** 6267–6272 (2018).

239. Cong, C. *et al.* Synthesis and optical properties of large-area single-crystalline 2D semiconductor WS_2 monolayer from chemical vapor deposition. *Adv. Opt. Mater.* **2,** 131–136 (2013).

240. McCreary, K. M. *et al.* Synthesis of large-area WS_2 monolayers with exceptional photoluminescence. *Sci. Rep.* **6** (2016).

241. Li, X. *et al.* Insight into the role of H_2 in WS_2 growth by chemical vapor deposition. *ACS Appl. Electron. Mater.* **3,** 5138–5146 (2021).

242. An, G. H. *et al.* Growth mode control of CVD-grown WS_2 monolayer flakes via O_2 pre-annealing for organic surfactant oxidation. *Appl. Surf. Sci.* **585,** 152564 (2022).

243. Yu, Y. *et al.* Controlled scalable synthesis of uniform, high-quality monolayer and few-layer MoS_2 films. *Sci. Rep.* **3** (2013).

244. Yu, H. *et al.* Wafer-scale growth and transfer of highly-oriented monolayer MoS_2 continuous films. *ACS Nano* **11,** 12001–12007 (2017).

245. Xu, H. *et al.* High-performance wafer-scale MoS_2 transistors toward practical application. *Small* **14** (2018).

246. Cohen, A. *et al.* Growth-etch metal–organic chemical vapor deposition approach of WS_2 atomic layers. *ACS Nano* **15,** 526–538 (2020).

247. Yang, P. *et al.* Epitaxial growth of centimeter-scale single-crystal MoS_2 monolayer on Au(111). *ACS Nano* **14,** 5036–5045 (2020).

248. Kim, M. *et al.* High-crystalline monolayer transition metal dichalcogenides films for wafer-scale electronics. *ACS Nano* **15,** 3038–3046 (2021).

249. Chubarov, M. *et al.* Wafer-scale epitaxial growth of unidirectional WS_2 monolayers on sapphire. *ACS Nano* **15,** 2532–2541 (2021).

250. Li, T. *et al.* Epitaxial growth of wafer-scale molybdenum disulfide semiconductor single crystals on sapphire. *Nat. Nanotechnol.* **16,** 1201–1207 (2021).

251. Xia, Y. *et al.* 12-inch growth of uniform MoS_2 monolayer for integrated circuit manufacture. *Nat. Mater.* **22,** 1324–1331 (2023).

252. Xue, G. *et al.* Modularized batch production of 12-inch transition metal dichalcogenides by local element supply. *Science Bulletin* **68,** 1514–1521 (2023).

253. Bauer, E. Phänomenologische Theorie der Kristallabscheidung an Oberflächen. I. *Zeitschrift für Kristallographie* **110,** 372–394 (1958).

254. Bauer, E. Phänomenologische Theorie der Kristallabscheidung an Oberflächen. II. *Zeitschrift für Kristallographie - Crystalline Materials* **110** (1958).

255. Scheel, H. J. *Crystal growth technology* Reprint. (ed Scheel, H. J.) 668 pp. (Wiley, 2005).

256. Scheel, H. J. & Fukuda, T. *Crystal growth technology* (Wiley, 2003).

257. Saito, Y. *Statistical physics of crystal growth* (World Scientific, 1996).

258. Voronenkov, V. *et al.* Guiding principles for the design of a chemical vapor deposition process for highly crystalline transition metal dichalcogenides. *Phys. Status Solidi (a)* (2024).

259. Young, T. An essay on the cohesion of fluids. *Philosophical Transactions of the Royal Society of London* **95,** 65–87 (1805).

260. Frank, F. C. & van der Merwe, J. H. One-dimensional Dislocations. I. Static Theory. *Proc. R. Soc. Lond. A* **198,** 205–216 (Mathematical and Physical Sciences 1949).

261. Volmer, M. & Weber, A. Keimbildung in übersättigten Gebilden. *Zeitschrift für Physikalische Chemie* **119U,** 277–301 (1926).

262. Stranski, I. N. & Krastanow, L. Zur Theorie der orientierten Ausscheidung von Ionenkristallen aufeinander Abhandlungen der Mathematisch-Naturwissenschaftlichen Klasse IIb. *Akademie der Wissenschaften Wien. Abhandlungen der Mathematisch-Naturwissenschaftlichen Klasse IIb,* 797–810 (1938).

263. Dumcenco, D. *et al.* Large-area epitaxial monolayer MoS_2. *ACS Nano* **9,** 4611–4620 (2015).

264. Burton, W. K., Cabrera, N. & Frank, F. C. The growth of crystals and the equilibrium structure of their surfaces. *Phil. Trans. R. Soc. Lond. A, Math. Phys. Sci.* **243,** 299–358 (1951).

265. Ko-ichi Yamaguchi, K.-i. Y. & Kotaro Okamoto, K. O. Lateral supply mechanisms in selective metalorganic chemical vapor deposition. *JJAP* **32,** 1523 (1993).

266. Olsson, F. *et al.* Large mask area effects in selective area growth. *J. Cryst. Growth* **289,** 24–30 (2006).

267. Zhang, J. *et al.* Scalable growth of high-quality polycrystalline MoS_2 monolayers on SiO_2 with tunable grain sizes. *ACS Nano* **8,** 6024–6030 (2014).

268. Zhang, X. *et al.* Diffusion-controlled epitaxy of large area coalesced WSe_2 monolayers on sapphire. *Nano Lett.* **18,** 1049–1056 (2018).

269. Hertz, H. Über den Druck des gesättigten Quecksilberdampfes. *Annalen der Physik* **253,** 193–200 (1882).

270. Knudsen, M. Die maximale Verdampfungsgeschwindigkeit des Quecksilbers. *Annalen der Physik* **352,** 697–708 (1915).

271. Knacke, O., Strankski, I. N. & Wolff, G. *Zur Struktur und Materie der Festkörper: Die Verdampfung von Krystallen* 34–55 (Springer Berlin Heidelberg, 1952).

272. Fick, A. Über Diffusion. *Annalen der Physik* **170,** 59–86 (1855).

273. Cao, D. *et al.* Role of Chemical Potential in Flake Shape and Edge Properties of Monolayer MoS_2. *J. Phys. Chem. C* **119,** 4294–4301 (2015).

274. Fu, W. *et al.* Toward edge engineering of two-dimensional layered transition-metal dichalcogenides by chemical vapor deposition. *ACS Nano* **17,** 16348–16368 (2023).

275. Mazitov, A. *et al.* Substrate-aware computational design of two-dimensional materials. *arXiv* (2024).

276. Zhang, J. *et al.* Towards controlled synthesis of 2D crystals by chemical vapor deposition (CVD). *Materials Today* **40,** 132–139 (2020).

277. Morita, M. *et al.* Growth of native oxide on a silicon surface. *J. Appl. Phys.* **68,** 1272–1281 (1990).

278. Naylor, C. H. *et al.* Monolayer single-crystal 1T'-$MoTe_2$ grown by chemical vapor deposition exhibits weak antilocalization effect. *Nano Lett.* **16,** 4297–4304 (2016).

279. Empante, T. A. *et al.* Chemical vapor deposition growth of few-layer $MoTe_2$ in the 2H, 1T', and 1T phases: tunable properties of $MoTe_2$ films. *ACS Nano* **11,** 900–905 (2017).

280. Deng, Y. *et al.* $MoTe_2$: semiconductor or semimetal? *ACS Nano* **15,** 12465–12474 (2021).

281. Hynek, D. J. *et al.* cm^2-scale synthesis of $MoTe_2$ thin films with large grains and layer Control. *ACS Nano* **15,** 410–418 (2020).

282. Xu, T. *et al.* Phase-controllable chemical vapor deposition synthesis of atomically thin $MoTe_2$. *Nanomater.* **12,** 4133 (2022).

283. Wang, Y. *et al.* Structural phase transition in monolayer $MoTe_2$ driven by electrostatic doping. *Nature* **550,** 487–491 (2017).

284. Duerloo, K.-A. N., Li, Y. & Reed, E. J. Structural phase transitions in two-dimensional Mo- and W-dichalcogenide monolayers. *Nat. Commun.* **5** (2014).

285. Huang, H. H. *et al.* Controlling phase transition for single-layer MTe_2 (M = Mo and W): modulation of the potential barrier under strain. *Physical Chemistry Chemical Physics* **18,** 4086–4094 (2016).

286. Selig, M. *et al.* Excitonic linewidth and coherence lifetime in monolayer transition metal dichalcogenides. *Nat. Commun.* **7** (2016).

287. Arora, A. *et al.* Exciton band structure in layered $MoSe_2$: from a monolayer to the bulk limit. *Nanoscale* **7,** 20769–20775 (2015).

288. Koirala, S. *et al.* Homogeneous linewidth broadening and exciton dephasing mechanism in MoT_2. *Phys. Rev. B* **93,** 075411 (2016).

289. Dey, P. *et al.* Optical coherence in atomic-monolayer transition-metal dichalcogenides limited by electron-phonon interactions. *Phys. Rev. Lett.* **116,** 127402 (2016).

290. Cadiz, F. *et al.* Excitonic linewidth approaching the homogeneous limit in MoS_2-based van der Waals heterostructures. *Phys. Rev. X* **7,** 021026 (2017).

291. Fang, H. H. *et al.* Control of the exciton radiative lifetime in van der Waals heterostructures. *Phys. Rev. Lett.* **123,** 067401 (2019).

292. Ross, J. S. *et al.* Electrical control of neutral and charged excitons in a monolayer semiconductor. *Nat. Commun.* **4** (2013).

293. Singh, A. *et al.* Trion formation dynamics in monolayer transition metal dichalcogenides. *Phys. Rev. B* **93,** 041401 (2016).

294. Sun, D. *et al.* Chemical vapor deposition growth of a periodic array of single-layer MoS_2 islands via lithographic patterning of an SiO_2 /Si substrate. *2D Mater.* **2,** 045014 (2015).

295. Han, G. H. *et al.* Seeded growth of highly crystalline molybdenum disulphide monolayers at controlled locations. *Nat. Commun.* **6** (2015).

296. Li, Y. *et al.* Site-specific positioning and patterning of MoS_2 monolayers: the role of Au seeding. *ACS Nano* **12,** 8970–8976 (2018).

297. Zobel, A. *et al.* Chemical vapour deposition and characterization of uniform bilayer and trilayer MoS_2 crystals. *J. Mater. Chem. C* **4,** 11081–11087 (2016).

298. Zheng, J. *et al.* High-mobility multilayered MoS_2 flakes with low contact resistance grown by chemical vapor deposition. *Adv. Mater.* **29** (2017).

299. Silva-Guillén, J., San-Jose, P. & Roldán, R. Electronic band structure of transition metal dichalcogenides from ab initio and Slater–Koster tight-binding model. *Appl. Sci.* **6,** 284 (2016).

300. Zhang, X. *et al.* Transition metal dichalcogenides bilayer single crystals by reverse-flow chemical vapor epitaxy. *Nat. Commun.* **10** (2019).

301. Mak, K. F. *et al.* Tightly bound trions in monolayer MoS_2. *Nat. Mater.* **12,** 207–211 (2012).

302. Mouri, S. *et al.* Thermal dissociation of inter-layer excitons in $MoS_2/MoSe_2$ hetero-bilayers. *Nanoscale* **9,** 6674–6679 (2017).

303. Pandey, J. & Soni, A. Unraveling biexciton and excitonic excited states from defect bound states in monolayer MoS_2. *Appl. Surf. Sci.* **463,** 52–57 (2019).

304. Courtade, E. *et al.* Charged excitons in monolayer WSe_2 : Experiment and theory. *Phys. Rev. B* **96,** 085302 (2017).

305. Gerber, I. C. *et al.* Interlayer excitons in bilayer MoS_2 with strong oscillator strength up to room temperature. *Phys. Rev. B* **99,** 035443 (2019).

306. Schneemeyer, L. F. & Sienko, M. J. Crystal data for mixed-anion molybdenum dichalcogenides. *Inorganic Chemistry* **19,** 789–791 (1980).

307. Agarwal, M. K. *et al.* Optical band gaps of molybdenum sulphoselenide (MoS_2 Se_{2-x}, $0 \leqq x \leqq 2$) single crystals from spectral response. *Phys. Status Solidi (a)* **90,** K107–K111 (1985).

308. Ajalkar, B. D. *et al.* Optical and electrical studies on molybdenum sulphoselenide [$Mo(S_{(1-x)}Se_x)_2$] thin films prepared by arrested precipitation technique (APT). *Solar Energy Materials and Solar Cells* **81,** 101–112 (2004).

309. Li, H. *et al.* Growth of alloy $MoS_{2x}Se_{2(1-x)}$ nanosheets with fully tunable chemical compositions and optical properties. *J. Am. Chem. Soc.* **136,** 3756–3759 (2014).

310. Jadczak, J. *et al.* Composition dependent lattice dynamics in $MoS_xSe_{(2-x)}$ alloys. *J. Appl. Phys.* **116** (2014).

311. Mann, J. *et al.* 2-dimensional transition metal dichalcogenides with tunable direct band gaps: $MoS_{2(1-x)}Se_{2x}$ monolayers. *Adv. Mater.* **26,** 1399–1404 (2013).

312. Feng, Q. *et al.* Growth of large-area 2D $MoS_{2(1-x)}Se_{2x}$ semiconductor alloys. *Adv. Mater.* **26,** 2648–2653 (2014).

313. Feng, Q. *et al.* Growth of $MoS_{2(1-x)}Se_{2x}$ (x = 0.41-1.00) monolayer alloys with controlled morphology by physical vapor deposition. *ACS Nano* **9,** 7450–7455 (2015).

314. Kang, T. *et al.* Band alignment engineering by twist angle and composition modulation for heterobilayer. *Small* **18** (2022).

315. Christopher, J. W., Goldberg, B. B. & Swan, A. K. Long tailed trions in monolayer MoS_2: temperature dependent asymmetry and resulting red-shift of trion photoluminescence spectra. *Sci. Rep.* **7** (2017).

316. Mouri, S., Miyauchi, Y. & Matsuda, K. Tunable photoluminescence of monolayer MoS_2 via chemical doping. *Nano Lett.* **13,** 5944–5948 (2013).

317. Wieting, T. J. & Verble, J. L. Infrared and Raman studies of long-wavelength optical phonons in hexagonal MoS_2. *Phys. Rev. B* **3,** 4286–4292 (1971).

318. Sekine, T. *et al.* Raman Scattering and Infrared Reflectance in 2H-$MoSe_2$. *JPSJ* **49,** 1069–1077 (1980).

319. Sugai, S. & Ueda, T. High-pressure Raman spectroscopy in the layered materials 2H-MoS_2, 2H-$MoSe_2$, and 2H-$MoTe_2$. *Phys. Rev. B* **26,** 6554–6558 (1982).

320. Stacy, A. M. & Hodul, D. T. Raman spectra of IVB and VIB transition metal disulfides using laser energies near the absorption edges. *J. Phys. Chem. Solids* **46,** 405–409 (1985).

321. Li, H. *et al.* From bulk to monolayer MoS_2: evolution of Raman scattering. *Adv. Funct. Mater.* **22,** 1385–1390 (2012).

322. Komsa, H.-P. & Krasheninnikov, A. V. Two-Dimensional Transition Metal Dichalcogenide Alloys: Stability and Electronic Properties. *J. Phys. Chem. C Lett.* **3,** 3652–3656 (2012).

323. Förste, J. *Spectroscopy of gate-tunable thin films of tungsten-diselenide* Master Thesis (Ludwig-Maximilians-University Munich, 2018).

324. Conley, H. J. *et al.* Bandgap engineering of strained monolayer and bilayer MoS_2. *Nano Lett.* **13,** 3626–3630 (2013).

325. He, K. *et al.* Experimental demonstration of continuous electronic structure tuning via strain in atomically thin MoS_2. *Nano Lett.* **13,** 2931–2936 (2013).

326. Li, H. *et al.* Optoelectronic crystal of artificial atoms in strain-textured molybdenum disulphide. *Nat. Commun.* **6** (2015).

327. Lloyd, D. *et al.* Band gap engineering with ultralarge biaxial strains in suspended monolayer MoS_2. *Nano Lett.* **16,** 5836–5841 (2016).

328. Liang, J. *et al.* Monitoring local strain vector in atomic-layered $MoSe_2$ by second-harmonic generation. *Nano Lett.* **17,** 7539–7543 (2017).

329. Cheng, X. *et al.* Using strain to alter the energy bands of the monolayer $MoSe_2$: A systematic study covering both tensile and compressive states. *Appl. Surf. Sci.* **521,** 146398 (2020).

330. Chen, Y., Fang, F. & Zhang, N. Advance in additive manufacturing of 2D materials at the atomic and close-to-atomic scale. *npj 2D mater. appl.* **8** (2024).

331. Zhu, J. *et al.* Low-thermal-budget synthesis of monolayer molybdenum disulfide for silicon back-end-of-line integration on a 200 mm platform. *Nat. Nanotechnol.* **18,** 456–463 (2023).

332. Kanade, C. K. *et al.* Low-temperature and large-scale production of a transition metal sulfide vertical heterostructure and its application for photodetectors. *ACS Appl. Mater. Interfaces.* **13,** 8710–8717 (2021).

333. Seok, H. *et al.* Low-temperature synthesis of wafer-scale MoS_2-WS_2 vertical heterostructures by single-step penetrative plasma sulfurization. *ACS Nano* **15,** 707–718 (2021).

334. Kim, H.-U. *et al.* Wafer-scale and low-temperature growth of 1T-WS_2 film for efficient and stable hydrogen evolution reaction. *Small* **16** (2020).

335. Wang, J. *et al.* Dual-coupling-guided epitaxial growth of wafer-scale single-crystal WS_2 monolayer on vicinal α-plane sapphire. *Nat. Nanotechnol.* **17,** 33–38 (2021).

336. Yang, P. *et al.* Epitaxial growth of inch-scale single-crystal transition metal dichalcogenides through the patching of unidirectionally orientated ribbons. *Nat. Commun.* **13** (2022).

337. Rajan, A. *et al.* Morphology control of epitaxial monolayer transition metal dichalcogenides. *Phys. Rev. Mater.* **4,** 014003 (2020).

338. Park, J.-H. *et al.* Synthesis of high-performance monolayer molybdenum disulfide at low temperature. *Small Methods* **5** (2021).

339. Hoang, A. T. *et al.* Low-temperature growth of MoS_2 on polymer and thin glass substrates for flexible electronics. *Nat. Nanotechnol.* **18,** 1439–1447 (2023).

Acknowledgments

Persuing a PhD has been an incredible part of my life. Now it is time to say thank you to all the people that have accompanied me along this journey and have helped to make this work possible.
First and foremost, I would like to thank my supervisor Alexander Högele. Thank you, Alex, for enabling me to do the PhD in your research group, for fostering low hierarchies in your group, and for always being approachable when supervision was needed.
A big thank you goes to the CVD team, Ismail Bilgin and Zhijie Li, for keeping the CVD system up and running with me and for always being open to discussions and sharing your results. Thank you, Ismail, for establishing the CVD system in our group and passing down your knowledge to us.
My deepest gratitude goes to the entire Nanophotonics group with all the past and present team members who fostered a scientifically productive, creative, and fun environment. Thank you Victor Funk and Jonathan Förste, for your supervision during my Master project and taking me up as a fellow PhD student. Thank you, Samarth Vadia, for many discussions and encouragement. Thank you, Johannes Scherzer and Lukas Husel, for accompanying me from the first Bachelor semester all the way to the last months of my PhD. Borislav Polovnikov, Subhradeep Misra, Farsane Tabataba-Vakili, Shen Zhao, Anna Rupp, Julian Trapp, and Tim Wedl: thank you for the amazing group atmosphere and the great time together inside and outside of the lab. And of course Anvar Baimuratov, thank you for the hard work in trying to explain theory to experimentalists. Thank you to Manuel Nutz, Michael Förg, Jonathan Noé, André Neumann and Jessica Lindlau for sharing your knowledge and staying in contact after you left.
It is almost needless to say that the work in the laboratories and the cleanroom would not be possible without an incredible staff of technicians. Thanks to all the technicians from the Rädler and former Kotthaus chair who made this work possible: Heribert Lorenz, for keeping everything up and running, Anton Heindl, for all those refills of liquid helium and nitrogen and without whom I probably would have never used the old and scary-looking diamond saw in the basement, Charlott Leu, for always helping and sharing your knowledge on lithography, Stefan Manus, for always having the right

electrical part at hand, and Philipp Altpeter and Christian Obermayer, thank you for always helping out and your incredible efforts to keep the entire cleanroom and every machinery therein in top shape. And thank you Dayse Ferreira e Silva, for taking care of the administrative side and making our lives easier.
I also want to thank my collaborators at Caltech who have welcomed me to their labs in California. Thank you Nai-Chang Yeh, for hosting me in your group and fostering a vivid scientific environment. Thank you Akioshi Park and Rohit Kantipudi for your efforts on our projects and the good times together. And thank you Daniel Anderson, Duxing Hao, and Steve Lu, for the discussions and open work environment in your labs.
I am deeply grateful to many more people that I have the pleasure of calling friends and family. Thank you to my parents and my sister, for supporting me my entire life. Thank you Erika, for all the support by my side during the entirety of my PhD and reminding me that there are other things in life than PhD work. Thank you Fabian Schmidt, for teaching me that sometimes things just need to look good. Thank you Florian Schoner and Nicolas Macé for being amazing flatmates and sharing the pain of pursuing a PhD.
And lastly, thank you to all the other people that have supported me along my journey. To include all those names here would add too many pages to this work. So I will end it here, knowing that you guys know who you are, and say: thank you deeply for all the support, companionship, and good times.